The Dissertation Committee for Patrick Kelly Crumley
certifies that this is the approved version of the following dissertation:

On the Nature of Emission from Relativistic Jets

Committee:

Duane Dicus, Supervisor

Pawan Kumar, Co-Supervisor

Milos Milosavljevic

Richard Matzner

Sera Markoff

On the Nature of Emission from Relativistic Jets

by

Patrick Kelly Crumley, B.A.

DISSERTATION
Presented to the Faculty of the Graduate School of
The University of Texas at Austin
in Partial Fulfillment
of the Requirements
for the Degree of

DOCTOR OF PHILOSOPHY

THE UNIVERSITY OF TEXAS AT AUSTIN
May 2015

Dedicated to my wife, Diana, and son, Arlo.

Acknowledgments

First and foremost, I would like to thank Pawan Kumar, whose guidance on matters scientific and personal has been invaluable throughout the course of my PhD. I am grateful for the time he has generously given me, and for his insights into astrophysics. I am particularly grateful for the open environment that never stifled dissent, encouraged us to form our own opinions, and forced us to get to the heart of the science behind any issue. Pawan always has time for our questions. All he asks is that we be willing to try to answer them on the blackboard with a piece of chalk. I feel privileged to have been a member of his group.

I'd like to thank the graduate students who participated in our weekly journal clubs over the years. Former graduate students Rodolfo Barniol-Duran and Rongfeng Shen, for providing a welcoming environment when I first entered the group. They were always patient with my beginner questions as I transitioned into astrophysics. Current graduate students Rodolfo Santana, Roberto Hernández, and Wenbin Lu, who have provided a wealth of scientific insight over the years.

Thanks are due to my parents, David and Rene, who have always encouraged me in my academic pursuits from an early age.

Finally, I'm deeply indebted to my wife, Diana Crumley. She has been unbelievably supportive and helpful throughout my PhD. She's been constant source of encouragement and a welcome respite from the stressors of graduate schoool.

On the Nature of Emission from Relativistic Jets

Publication No. ____________________

Patrick Kelly Crumley, Ph.D.
The University of Texas at Austin, 2015

Supervisors: Duane Dicus
Pawan Kumar

Several longstanding questions in astrophysics center on the make up of relativistic astrophysical jets seen in microquasars, blazars, gamma-ray bursts, and super-Eddington tidal disruption events. What carries the energy in these jets? Is the majority of the energy carried by Poynting flux or by the baryonic matter? How is this energy converted into the non-thermal gamma-rays and X-rays seen in these systems? While there are many different theoretical models for launching a relativistic jet and producing the non-thermal emission observed in these astrophysical systems, often times the observational data are not good enough to convincingly discriminate between models. This thesis is comprised of several different projects that address these questions for several different astrophysical systems. First I discuss some general considerations of the synchrotron radiation from electrons accelerated by magnetic reconnection in a Poynting dominated jet. I show that the super-Eddington tidal disruption events (TDE) represent an unique opportunity to test different emission mechanisms in relativistic jets. I find that a magnetic dominated jet model can most easily explain the broadband observations in the observed super-Eddington TDE Sw J1644+57. In gamma-ray bursts, that hadronic emission models cannot explain the high energy ($\gtrsim$100 MeV) gamma-rays observed by the Fermi Large Area Telescope. I also include a chapter that suggests using the radio monitoring of the diffuse cloud in the galactic center object G2's to distinguish between different models of G2. Early observations of G2 after periapse passage suggests this prediction was correct.

Table of Contents

Acknowledgments **v**

Abstract **vi**

List of Figures **xi**

Chapter 1. Introduction and Overview **1**
- 1.1 Tidal Disruption Events 7
- 1.2 The Galactic Center "Cloud" G2 9
- 1.3 Gamma-ray Bursts 10

Chapter 2. Radiation from a Relativistic Poynting Jet: some general considerations **13**
- 2.1 Introduction 13
- 2.2 Poynting jet: a few general considerations 15
  - 2.2.1 Particle acceleration in current sheets 20
  - 2.2.2 Electron distribution function 29
  - 2.2.3 Synchrotron and IC spectra 32
  - 2.2.4 Constraint on the number of current sheets in the jet . . 36
- 2.3 Discussion 39

Chapter 3. Swift J1644+57: an Ideal Test Bed of Radiation Mechanisms in a Relativistic Super-Eddington Jet **41**
- 3.1 Introduction 42
- 3.2 Overview of Sw J1644+57 properties 46
- 3.3 Synchrotron Model of TDE Sw J1644+57 48
  - 3.3.1 Detailed Synchrotron Model of TDE Sw J1644+57 . . . 55
    - 3.3.1.1 Radiation Physics 57
    - 3.3.1.2 Synchrotron Radiation 57

        3.3.1.3 Synchrotron Self Compton 60
        3.3.1.4 The electron distribution 65
        3.3.1.5 Energetics 66
3.4 Proton Synchrotron 69
3.5 Internal Inverse-Compton Radiation 73
3.6 External Inverse-Compton Radiation 80
    3.6.1 Jet Characteristics 80
    3.6.2 Radiation from the Wind 81
    3.6.3 External Inverse-Compton Luminosity 85
        3.6.3.1 EIC above the photosphere 85
        3.6.3.2 EIC below the photosphere 86
    3.6.4 External Inverse-Compton Spectrum 88
3.7 Photospheric model of TDE SW J1644+57 90
    3.7.1 Spectrum for Photospheric Process 91
    3.7.2 Photospheric Radius and Photon to Electron Ratio for SW J1644+57 92
    3.7.3 Input Parameters for MC Photospheric Simulations . . . 94
    3.7.4 MC Photospheric Simulation Results With One Electron Heating Event 97
        3.7.4.1 Estimating N_{pl} 98
        3.7.4.2 Estimating N_{cool} 99
    3.7.5 Estimating Number of Electron Re-heating Events Needed To Produce A Power-Law Spectrum 100
3.8 Poynting-Dominated jet 101
3.9 Conclusions 109

Chapter 4. Radio-synchrotron Emission from the Extended Object at the Galactic Center, G2 112
4.1 Introduction 112
4.2 Methodology 117
    4.2.1 Environment at the Galactic Center 117
    4.2.2 Geometry of the Bow Shock 118
4.3 Results 120
    4.3.1 Radio Flux of Forward Shock 120

        4.3.2 Radio Flux of Inner Shock 124
        4.3.3 Spectra 128
    4.4 Application to the Star S2 128
    4.5 Conclusions 129

Chapter 5. Hadronic Models of Gamma-ray Bursts **131**
    5.1 Introduction 132
    5.2 Photo-pion Production 136
        5.2.1 Analytical Estimate 138
            5.2.1.1 Neutrino Flux 142
        5.2.2 Numerical Calculation 144
    5.3 Bethe-Heitler Pair Production 151
    5.4 Proton Synchrotron 157
    5.5 Summary and Discussion 164

Bibliography **167**

Vita **182**

List of Figures

2.1 A schematic sketch of a Poynting jet and multiple reconnection zones . . . 17
2.2 The inertial frame where electric fields and magnetic field are parallel . . . 23
2.3 Acceleration of an electron in a current sheet is shown as a function of time . . . 26
2.4 Synchrotron flux and spectrum from electrons accelerated via magnetic reconnection . . . 35

3.1 Example Synchrotron Self-Compton Spectra . . . 61
3.2 Parameter Space available to the Synchrotron-in-Shock model of Sw J1644+57 . . . 67
3.3 The available parameter space to the inverse Compton model of Sw J1644+57 . . . 77
3.4 Photospheric spectrum for Sw J1644+57 . . . 97
3.5 The available parameter space for Magnetic Reconnection model of Sw J1644+57 . . . 105
3.6 A sample spectra in the magnetic reconnection process . . . 108

4.1 The Cross-sectional Area of G2 as it approaches Sgr A* . . . 120
4.2 The Synchrotron flux from the Bow-Shock of G2 . . . 125
4.3 Sychrotron Spectra from the Bow-Shock of G2 . . . 127

5.1 Maximum efficiency for the Photo-pion process in GRBs, 1-D plot . . . 152
5.2 Maximum efficiency for the Photo-pion process in GRBs, 2-D plot . . . 153
5.3 Efficiency of the proton synchrotron process for LAT GRBs . . . 160

Chapter 1

Introduction and Overview

Bipolar, highly-collimated jets are present in many astrophysical systems where gas is accreting onto a spinning compact object, such as a black hole or a neutron star. These jets are capable of traveling great distances from where they were launched, and can carry a tremendous amount of energy. Jets are associated with the most energetic and luminous objects in the universe, active galactic nuclei (*e.g.*, Jennison & Das Gupta, 1953; Hargrave & Ryle, 1974; Rawlings & Saunders, 1991; Begelman et al., 1984, for review) and gamma-ray bursts (*e.g.*, Mészáros & Rees, 1993; Kumar & Zhang, 2015, for review). Jets are associated with a wide range of astrophysical systems that differ in many orders of magnitude in accretion rates and compact object mass: super-massive black holes at the center of galaxies, gamma-ray bursts, black hole binaries (*e.g.*, Margon, 1984; Remillard & McClintock, 2006), and neutron star binaries (*e.g.* Sell et al., 2010). It appears that jets are a common feature of astrophysical accretion onto compact objects.

A general schematic for accretion onto a compact object is as follows: if the gas has no net angular momentum with respect to the compact object, the accretion rate is determined by spherically symmetric Bondi-Hoyle accretion (Bondi & Hoyle, 1944; Bondi, 1952). In many astrophysical systems, the reservoir of gas feeding the compact object has some net angular momentum with respect to the central object. When the gas carries some net angular momentum, gas trying to fall onto the central mass will collide with itself and circularize into a disk. If angular momentum were to be conserved, a parcel of gas that starts with a specific angular momentum l will end up at a radial distance from the black hole given by $R = l^2/(GM_\bullet)$. For the gas to fall further onto the black hole, it must lose some of its angular momentum. In most astrophysical disks we expect that the orbital time is less than the accretion time, and therefore the orbits can be taken to be more or less circular, *i.e.*, Keplerian orbits with an orbital frequency $\Omega \propto R^{-3/2}$. We can see that there is differential rotation within the disk. This differential rotation can play a critical role in angular momentum transport throughout the disk, either by providing supersonic turbulence that causes the so-called α-viscosity (Shakura & Sunyaev, 1973) or through a magneto-rotational instabilities (Balbus & Hawley, 1991). If there is a large scale magnetic field threading the disk with a significant poloidal component, angular momentum can be carried off by a mildly collimated jet/wind as well (Blandford & Payne, 1982).

If a jet is to be powered by the black hole's spin through the Blandford-Znajek process, the poloidal component of the magnetic flux must be large nearby the black hole. A large magnetic flux is required because the Blandford-Znajek power scales with the black hole spin a and magnetic flux threading the black hole Φ_B as $P_{\rm BZ} \propto a^2\Phi_B^2$ (Blandford & Znajek, 1977; Tchekhovskoy et al., 2010). How a large scale poloidal component to the magnetic field could be formed is currently a matter of debate. Either it is formed inside of the disc through an MHD dynamo (Tout & Pringle, 1996), or the magnetic flux is transported in from large radii along with the plasma (Narayan et al., 2003). With a large scale polodial magnetic field close to the black hole, a powerful, relativistic jet can be launched.

From the general picture outlined above, it is clear that magnetic fields probably play an important part in the formation and powering of black hole jets. While a plausible scenario can be sketched out, exactly how a relativistic jet is launched and collimated is still an unsolved question in astrophysics. There has been a great deal of progress on this front recently, led both by advances in the computational simulations of accretion disks and jets, (*e.g.*, Komissarov, 2001; Semenov et al., 2004; McKinney, 2006; Komissarov et al., 2007, 2009; Tchekhovskoy et al., 2011; McKinney et al., 2012, 2013) and through new observations (*e.g.*, Celotti et al., 1997; Eatough et al., 2013; Ghisellini et al., 2014; Zamaninasab et al., 2014). Regardless of how the jet is formed and powered, one question remains: how does the jet dissipate the tremendous amount of energy it is carrying to produce the observed broadband non-thermal emission observed in blazars, gamma-ray bursts, and tidal disruption events? How this radiation is produced is an open question in astrophysics. We hope that in addressing these questions we will learn something about the makeup of the jets.

There are good reasons to try to constrain the properties of super-Eddington jets by modeling their radiation. For one, for super-Eddington accretion to work, the jet and the disk must be optically thick to photons. It is simply not possible to peer into the region where super-Eddington jets are launched. Contrast this to where the non-thermal X-rays and gamma-rays are produced. This is where super-Eddington TDEs and GRBs shine the brightest. It must be optically thin there, or in the case of photospheric models, modestly optically thick. In GRBs, most of the time only the prompt emission from an unresolved jet and its afterglow are observed. If we're particularly lucky we might see an accompanying supernova. In TDEs, if the host galaxy does not have too much extinction, it is possible to detect the accretion disk, but you still will not be able see the innermost regions where jet is launched.

That's not to say that aren't significant challenges to constraining jet properties by modeling their radiation. It's practically a tautology to state that any conclusions made may be model dependent. The onus is on the modeler to prove that their findings are ultimately independent of their choices and the models they considered. But even the most careful and thorough modeler will face an insurmountable problem when trying to disentangle the data; often times the data will allow multiple models to work. This is particularly frustrating when one model "feels best" but other, less plausible models are fiendishly difficult to conclusively rule out. With this in mind I outline a general prescription of things needed for the modeling approach to work well on a system with a relativistic jet.

1. A tight energy budget. While one can always appeal to a more efficient way of producing a spectrum or light curve as being more likely, any conclusion based solely on such an argument will rest on shaky ground. It is much better if the total energy available is known, and the energy in the observed radiation is a large fraction of the available energy. In TDEs and GRBs, we know that one star's worth of gas gets accreted onto the compact object. This sets an upper limit to the total energy budget of $\lesssim Mc^2$.[1] The total energy released in X-rays and gamma-rays by TDEs and GRBs can be a large fraction of this total energy, forcing the emission mechanism to be efficient.

---

[1] The energy in the jet may be slightly larger by a factor of a few because in the Blandford-Znajek mechanism, the jet is be powered by the black hole's spin (Tchekhovskoy et al., 2011).

2. Simultaneous broadband measurements. By having multiple simultaneous measurements in a wide range of photon energies we can constrain the models even if we don't require that they reproduce those measurements. Often times in trying to fit the a certain part of the observed spectrum, radiation will come out at a different wavelengths. With a wide range of measurements, we can rule out these models. With any transient that only lasts a brief time like GRBs, it will always be a difficult endeavor to take simultaneous measurements in other wavelengths.

3. Constraints on the radius of emission and/or the bulk Lorentz factor. Often times these two items are the most unknown free parameters in the model. GRBs in particular have poorly constrained radii and bulk Lorentz factors. For Sw J1644+57, afterglow modeling tells you that the Lorentz factor must be modest ~ 20, but VLBI measurements tell you is clearly relativistic so $\Gamma \gtrsim 2$. In addition, the TDE must be launched from a relatively large radius because it originates from a super-massive black hole as opposed to a stellar mass one. Both of these things work in concert to reduce the available parameter space of the model.

4. The data must be difficult to fit. If a model can easily fit the observations, chances are good that a different model will work as well. For the conclusions to be solid, the data should challenge nearly all attempts at explaining it. This is a double-edged sword. Over 20 years ago, Band et al. (1993) found nearly all spectra in GRBs were well fit by a smoothly-joined double power-law. Why this spectral shape is produced in GRBs is still a completely open question; no model has been able to reproduce it without ad hoc additions. Tremendous insight would be gained by

figuring out the prompt emission of GRBs, but it is unclear what is be needed to make significant progress.

There is a caveat to this approach, modeling the emission will only tell you the composition of the jet at the radius of emission. Since the emission region can be orders of magnitude further away from the central object than the jet launching point, the composition of the jet can change along the way. The jet can entrain more material as it travels, and the magnetic field may dissipate in order to accelerate the jet. For instance, the pulsar jets inside of the Crab Nebula are thought to be launched with a very large magnetization, but at the radius where the emission is produced, they are a matter dominated jet; *e.g.*, Michel (1982); Coroniti (1990); although see Lyubarsky & Kirk (2001) for a dissenting view.

This thesis is comprised of several projects that try to answer the question of how the observed non-thermal emission is produced in different astrophysical transients—all with the goal of constraining the make-up of the jet in the emission region. First I consider general implications of a Poynting dominated jet on the observed radiation in Chapter 2. Next I argue that super-Eddington tidal disruption events such as Sw J1644+57 are a particularly good system for which to discern an answer about the emission mechanism in the jet. I apply the Poynting dominated model as well as many others to the tidal disruption event Sw J1644+57 in Chapter 3. In Chapter 4, I model the interaction of G2, an extended object in the galactic center, with the accretion flow surrounding Sgr A*, the super-massive black hole in the center of the Milky Way. Finally, I model the highest energy photons observed in gamma-ray bursts with hadronic emission in Chapter 5. The rest of this introduction is dedicated to an brief overview of the transients mentioned above: tidal disruption events, G2, and gamma-ray bursts.

1.1 Tidal Disruption Events

A star is tidally disrupted by a black hole when the star's self-gravity can no longer resist the pull of the black hole's tidal force. When this happens, the star is completely ripped apart in a tidal disruption event (TDE). Roughly half the mass is unbound, and the rest falls back onto the black hole. The accretion rate is initially super-Eddington. Tidal disruptions are a way to turn a dormant super-massive black hole in a distant galaxy into an active galactic nuclei. TDEs are expected to occur at a rate $\sim 10^{-4} - 10^{-5}$ yr^{-1} in a Milky Way like galaxy. One of the signature signs of a tidal disruption event is a characteristically declining light curve as $L \propto t^{-5/3}$ (Rees, 1988; Phinney, 1989). During a TDE, a relativistic jet may be launched (Giannios & Metzger, 2011).

While originally a theoretical curiosity, in the last 10 years or so there have been many claims of an observed tidal disruption event[2]. Only a small fraction ($\lesssim 10\%$) of claimed TDEs have evidence that they launched a relativistic jet (Bower et al., 2013; van Velzen et al., 2013). Of the small fraction of TDEs that launch relativistic jets, only 2 have been observed along the jet axis. These two TDEs were discovered by Swift XRT, J1644+57 and J2058.4+0516. (Bloom et al., 2011; Burrows et al., 2011; Cenko et al., 2012). These objects are the gold standard for TDEs—the only known super-Eddington, relativistic TDEs where we were able to see the early time X-ray emission from the jet.

---

[2] See J. Guillochon's http://astrocrash.net/resources/tde-catalogue/ for a catalog of astrophysical transients claimed to be a TDE.

We focus on Sw J1644+57 because it occurred at a smaller redshift ($z = 0.354$) than J2058 ($z = 1.185$). The two events released a similar amount of energy; however the observed flux is much brighter for J1644 because it is ~ 4 times closer than J2058. Because Sw J1644+57 is much closer, the quality of its data is much better, with simultaneous broadband data. We will use these broadband observations to constrain models of the X-ray emission.

Sw J1644+57 had variable X-ray emission that lasted hundreds of days. After a brief 10 day period characterized by very strong flares peaking at a luminosity $L_X \approx 3 \times 10^{48}$ erg/s, the X-ray light curve declined in a manner consistent with $t^{-5/3}$. Sw J1644+5 X-rays had a hard spectrum, $f_\nu \propto \nu^{-0.8}$. How this X-ray emission is produced is an open question. In Chapter 3 we model the X-ray emission of Sw J1644+57.

TDEs with relativistic jets viewed on axis offer a unique opportunity to test emission models in relativistic jets because we know the energy budget for the radiation. During a TDE, roughly 1 solar mass of material is accreted by the black hole. This sets a strict upper limit on the total energy coming out in the jet as $\lesssim M_\odot c^2 \approx 2 \times 10^{54}$ erg. In Sw J1644+57, the average X-ray luminosity for the first 10 days was roughly 3×10^{47} erg/s, corresponding to a isotropic equivalent energy release of $E_{X,iso} \sim 3 \times 10^{53}$ erg, or a beam corrected energy if bulk Lorentz factor $\Gamma \sim 10$, $E_X \sim 3 \times 10^{51}$ erg. Therefore if the mechanism producing the observed X-ray radiation has an efficiency much less then 1%, it can be ruled since it requires too much energy. Additionally, because the emission from Sw J1644 had a bright period lasting more than a week, there was ample opportunity for simultaneous observations in multiple wavelengths. Sw J1644 has excellent observations in the radio, optical and near IR, and X-rays, as well as strong upper limits in the γ-rays. We take advantage of these constraints to test emission models of relativistic jets in Chapter 3. We find that many emission modes are unable to explain the observed emission of Sw J1644+57, and we favor an explanation where the X-ray radiation is produced through magnetic reconnection in a Poynting dominated jet.

1.2 The Galactic Center "Cloud" G2

In 2011, Gillessen et al. (2012) discovered an extended object with a radius of 2×10^{15} cm and a mass of 3 Earth masses in the process of being tidally disrupted by Sgr A*, the $4.3 \times 10^6\ M_\odot$ mass super-massive black hole that resides in the Milky Way center. Once the cloud reached pericenter of only 2400 Schwarzschild radii away from Sgr A* ($R_s \sim 10^{12}$ cm) in Spring 2014, it was expected that hydrodynamical forces would take over and the cloud would be completely shredded. If gas was capable of remaining cold as it was accreted by Sgr A*, it could have significantly boosted the accretion rate onto Sgr A* and therefore its X-ray luminosity. In addition, G2 was expected to drive a bow shock into the hot material surrounding Sgr A* that would be observable in the radio (Gillessen et al., 2012; Narayan et al., 2012a).

There was considerable excitement because it was almost like a designed experiment; we would be able to watch as a black hole feed on the gas surrounding it, with good knowledge of how much mass it was eating. Thus began one of the largest simultaneous observational campaigns in astronomy, with many different instruments monitoring the galactic center in the X-ray and radio, and many more set to observe if G2 triggered in the X-rays or radio. As G2 passed through periapsis, nothing happened. There was no increased activity at any wavelength attributable to G2 (Haggard et al., 2014; Hora et al., 2014; Tsuboi et al., 2015; Bower et al., 2015; Park et al., 2015;

Degenaar et al., 2015). G2 has appears to have emerged from pericenter intact and continued along its ballistic trajectory (Witzel et al., 2014; Pfuhl et al., 2015). This null result is disappointing because it means that we cannot use G2 to learn about how Sgr A* converts its accreted mass into X-rays. As we argue in Chapter 4, the result does hint at something about the nature of G2. Since the radio flux of the bow shock depends on the cross-sectional area of G2, the fact that radio emission from the bow shock was not observed is a hint that G2 is more compact at pericenter than previously believed. This would be the case if G2 was a momentum-supported bow shock from the wind of a star, as suggested by Scoville & Burkert (2013).

A stellar model of G2 is supported by the fact that G2 has not deviated from a Keplerian orbit as it passed through pericenter and G2's near infrared luminosity has been constant for as long as G2 has been observed. However, there are people who still dispute this interpretation (Pfuhl et al., 2015; McCourt & Madigan, 2015). If G2 is a momentum-supported bow shock from a stellar wind, and the stellar wind remains constant, the bow shock should reform roughly a year after periapsis (De Colle et al., 2014). The velocity dispersion in the Br-γ line should be smaller than before periapsis and roughly equal to the velocity of the stellar wind 50–200 km/s. If such a bow shock reappears, it will be incontrovertible proof that G2 is caused by a stellar wind.

1.3 Gamma-ray Bursts

Gamma-ray bursts (GRB) are the most luminous explosions in the universe. As their name implies, they appear as bright pulses that have a peak energy in the gamma-rays. For a general review see Piran (2004); Kumar & Zhang (2015). GRBs last anywhere from less than a second to hundreds of seconds. Since GRBs come from cosmological distances, the isotropic equivalent energy released by them is incredibly large. In a few tens of seconds a GRB will release as much energy as the sun will radiate in its lifetime. With the current generation of satellites, Swift and Fermi, GRBs are detected at a rate of a few per day. The brightness and variability of GRB requires them to be produced in very narrowly-collimated, highly-relativistic jets with bulk Lorentz factors $\Gamma \gtrsim 100$.

The launch of Fermi satellite opened a new window on GRBs. With the combination of two instruments, the Gamma-ray Burst Monitor (GBM) and the Large Area Telescope (LAT), Fermi has an unparalleled energy range from $\sim$ 10 keV to 300 GeV with which to observe GRBs. The high energy instrument, the Fermi-LAT, can detect photons with energies $\sim$ 100 MeV – 300 GeV and was a large improvement over its predecessor EGRET on the Compton Gamma-ray Observatory.

It was in the LAT energy range where Fermi made its largest discovery about GRBs: they emit very high-energy gamma-rays up to $\gtrsim 90$ GeV (Maselli et al., 2014). Often times the flux of these high-energy gamma-rays is consistent with being a simple extension of the spectrum of the lower energy gamma-rays $\gtrsim 1$ MeV *i.e.*, the highest energy photons observed by Fermi-LAT do not seem to add additional spectral features to GRBs. The $\gtrsim 100$ MeV photons are delayed with respect to the lower energy gamma-rays and they last longer. This lead to an interpretation that these photons were produced in the early afterglow (Kumar & Barniol Duran, 2009; Gao et al., 2009; Corsi et al., 2010; Kumar & Barniol Duran, 2010). However, the highest energy gamma-rays pose a challenge to GRB models because this energy exceeds the theoretical maximum possible synchrotron energy expected from electrons accelerated in shocks. The maximum energy is obtained by balancing a characteristic acceleration time with synchrotron cooling time for electrons, *e.g.*, de Jager et al. (1996); Maxham et al. (2011), although see Kumar et al. (2012) for a dissenting view. Since protons suffer less synchrotron cooling, people have suggested that the highest energy photons observed in GRBs might be created through hadronic radiation. In Chapter 5, we model the LAT emission observed in GRBs with hadronic processes. We find them to be inefficient and to have severe difficulties in reproducing the observed LAT radiation.

Chapter 2

Radiation from a Relativistic Poynting Jet: some general considerations

Chapter Preécis

We provide estimates for the flux and maximum frequency of radiation produced when the magnetic field in a relativistic, highly magnetized, jet is dissipated and particles are accelerated using general considerations. We also provide limits on the jet Lorentz factor and magnetization parameter from the observed flux. Furthermore, using the Lorentz invariance of scalar quantities produced with electromagnetic tensor, we provide constraints on particle acceleration, and general features of the emergent radiation. We find that the spectrum below the peak softens with decreasing frequency which is opposite to the case of a kinetic energy dominated jet where shocks are responsible for converting jet energy to radiation. A spectral softening with decreasing frequency may be one way of telling apart a magnetic jet from a kinetic jet.

2.1 Introduction

Relativistic jets where the energy is transported outward by Poynting flux ($\vec{E} \times \vec{B}$) have been invoked for many energetic outflows in astrophysical systems such as pulsars, quasars, micro-quasars and gamma-ray bursts

---

[†] This chapter has been submitted to MNRAS as Kumar P, Crumley P, 2015

(GRB). There is a vast peer reviewed literature on this topic *e.g.*, Michel (1969); Blandford & Znajek (1977); Blandford & Payne (1982); Kennel & Coroniti (1984); Begelman et al. (1984); Coroniti (1990); Mészáros & Rees (1997); Lyubarsky & Kirk (2001); de Gouveia dal Pino & Lazarian (2005); Drenkhahn & Spruit (2002); Lovelace et al. (2002); Kulsrud (2005); Giannios & Spruit (2006); Komissarov et al. (2007); Tchekhovskoy et al. (2008); Metzger et al. (2011); Cerutti et al. (2012).

The radiation is produced in these systems as a result of magnetic field dissipation (referred to as *reconnection*, a generic phrase, which we will be using throughout this article), where particles are accelerated either via parallel electric field or first order Fermi process in converging flows, and they then emit photons via the synchrotron process. Radiation could also be produced in shocks internal to the jet or when the jet interacts with the surrounding medium via a shock and transfers a fraction of its energy to particles in the external medium[1] We do not consider the latter process in this paper.

Magnetic reconnection is a complex and poorly understood process despite the work of numerous people on this problem for the last more than 50 years, *e.g.*, Dungey (1953); Sweet (1958); Parker (1957); Petschek (1964); Syrovatskii (1981); Biskamp (1986); Yamada et al. (1997); Kulsrud (1998); Uzdensky & Kulsrud (2000); Birn et al. (2001); Drake et al. (2006); Samtaney

---

[1] We are considering relativistic jets in this work which are Poynting flux dominated such as those that one encounters in Gamma-ray bursts, disruption of a star by the tidal gravity of a massive blackhole, or AGNs. If the jet energy were to be transported outward by particles as kinetic energy, then in that case the kinetic energy could be converted to radiation via internal and external shocks as discussed for GRB jets in the works of *e.g.*, Mészáros & Rees (1993); Rees & Meszaros (1994); Dermer et al. (1999); Ghisellini & Celotti (1999b); Stern & Poutanen (2004); Beloborodov (2010); Thompson & Gill (2014). However, the efficiency of converting jet kinetic energy to radiation in internal shocks is of order only a few percent *e.g.*, Kumar (1999).

et al. (2009); Zweibel & Yamada (2009). Does the difficulty in understanding the microphysics of magnetic reconnection mean that we are doomed in our effort to understand those astrophysical systems where Poynting jets play an important role until a predictive theory for reconnections is developed? The answer depends on what it is that we want to understand about these systems. If we are interested in the general, global, properties then the fine details of the reconnection process might not matter. A basic understanding can be obtained from certain Lorentz invariant functions of electromagnetic tensor and conservation laws. The goal of this paper is thus modest, and highly restricted in this sense, i.e., to try to provide some constraints on Poynting jet parameters (without having to rely on a particular reconnection model) so that magnetic dissipation can explain some broad aspects of the data such as the efficiency for converting magnetic energy to radiation and the general shape of the emergent spectrum. In a recent paper Beniamini & Piran (2014) have provided constraints on a Poynting jet model for GRBs. Their general approach and results are very different from the one we pursue here.

In section 2 we provide a few general properties of Poynting jet. We estimate the maximum energy electrons could achieve in reconnection, and the shape of emergent spectrum also in §2.

2.2 Poynting jet: a few general considerations

Figure 2.1 provides a schematic sketch of the system we are considering. The magnetic fields of a relativistic Poynting jet undergo dissipation at some radius[2] R and a number of current sheets form within the causally connected

---

[2] The dissipation of Poynting jet could be spread over a wide range in radius — R_1 to R_2 with $R_2 \gg R_1$. We are considering the maximum size of the region that is in causal contact

region of the jet of comoving size R/Γ (R/Γ^2 in lab frame) and efficiently convert the magnetic energy to particle energy and radiation. Within any current sheet there are likely to be a number of different regions where particles are accelerated, and within a space of size R/Γ there are obviously many more. These acceleration regions are usually associated with X-points — located in between plasmoids or magnetic islands that form due to tearing instability – where the magnetic field vanishes in absence of a guide field and where the electric field can accelerate particles, or with converging flows where particle acceleration takes place via first order Fermi process. Regions where particles are accelerated will be referred to as PASs (particle acceleration sites). Some general considerations regarding particle acceleration in an individual PAS is discussed in §2.2.1. The maximum Lorentz factor (LF) of particles in PASs is determined by a combination of electric field strength[3] and radiative losses in addition to energy conservation (§2.2.1). While outside PASs, particles lose energy to radiation and any acceleration they experience is negligible. The particle distribution function inside PASs is not determined in this paper and is taken to be a hard powerlaw function as per numerical simulations (Zenitani & Hoshino, 2001; Jaroschek et al., 2004; Sironi & Spitkovsky, 2011a, 2014; Guo et al., 2014). However, the distribution function outside PASs is determined by solving an appropriate set of equations (§2.2.2). Synchrotron radiation emanating from PASs and outside PASs is considered in §2.2.3. In §2.2.4 we

---

at R_2, i.e., between R_2/Γ^2 and R_2. If the causally connected region does not capture a good fraction of the energy dissipation process then we can add up results from other radii in a trivial way as processes going on in one region have no effect on another region that is not in causal contact.

[3] Particles are also accelerated in converging velocity flows (first order Fermi process) and stochastic velocity fields (second order Fermi process), but these are not considered in this work.

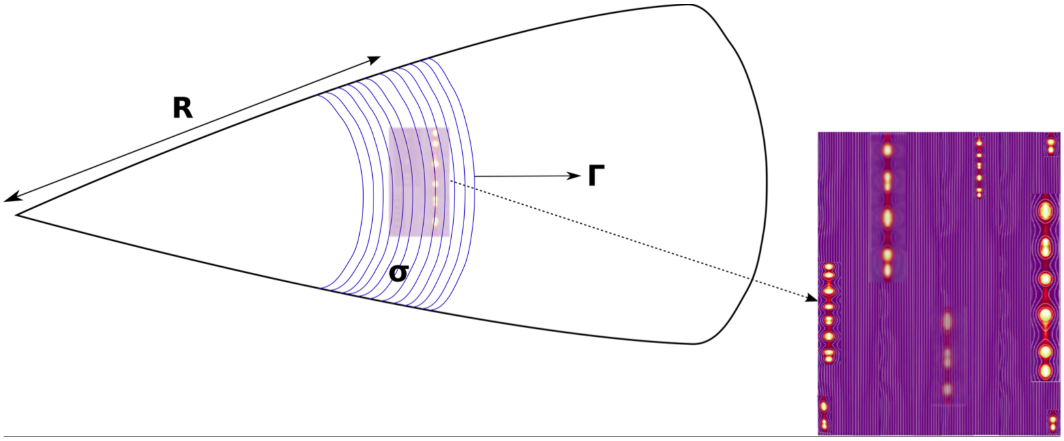

Figure 2.1: A schematic sketch of a Poynting jet and multiple reconnection zones within the causally connected region of comoving size R/Γ. Each reconnection zone has a number of PASs (the PASs are regions between bright spots or plasmoids where magnetic field is small and particles are accelerated by the electric field).

provide an estimate for distance from the center where Poynting jet is likely dissipated and the number of current sheets in the causally connected region for an efficient conversion of magnetic energy to radiation.

Let us consider a Poynting jet with magnetization parameter σ, Lorentz factor (LF) Γ, and isotropic equivalent luminosity L. The plasma is sufficiently cold so that the pressure of the particles can be ignored. The dissipation of magnetic field takes place when the jet is at radius R, and that is also roughly the radius where radiation is produced.

The magnetic field in the jet comoving frame is B'_0 — all physical quantities in the jet comoving frame are denoted by a prime and observer frame variables are un-primed — which is related to jet luminosity as

$$L = B_0'^2 \Gamma^2 R^2 c \quad \Longrightarrow \quad B'_0 = \frac{(L/c)^{1/2}}{\Gamma R} = (58 \text{ G}) \frac{L_{48}^{1/2}}{\Gamma_2 R_{15}} \tag{2.1}$$

provided that $\sigma > 1$; we are using the convenient notation $X_n \equiv X/10^n$.

We adopt the standard model that charged particles are accelerated in reconnection layers where magnetic field dissipation takes place. The accelerated electrons with "thermal" LF γ'_e emit synchrotron photons of frequency less than or equal to ν (in the observer frame) which is given by

$$\nu \approx \frac{qB'_0\gamma'^2_e\Gamma}{2\pi m_e c(1+z)}, \tag{2.2}$$

where q and m_e are electron charge and mass, and z is the redshift of the object. An upper limit to γ'_e can be obtained from energy conservation, i.e. the energy in accelerated particles cannot exceed the energy in magnetic field. This condition gives

$$n'_e\gamma'_{max}m_e c^2 \lesssim \frac{B'^2_0}{8\pi} \Longrightarrow \gamma'_{max} \lesssim (m_p/m_e)\sigma, \tag{2.3}$$

where n'_e is electron number density in the jet comoving frame, and

$$\sigma \equiv B'^2_0/(8\pi n'_e m_p c^2) \tag{2.4}$$

is jet magnetization parameter. The reason that equation (2.3) gives the maximum electron LF and not the average LF is because electrons accelerated in current sheets have a power-law distribution function ($dn_e/d\gamma_e \propto \gamma_e^{-p}$) with $p < 2$ when the region where the reconnection takes place is strongly magnetized $\sigma \gtrsim 10$ and if the reconnection layer is sufficiently large (*e.g.*, Romanova & Lovelace, 1992; Zenitani & Hoshino, 2001; Sironi & Spitkovsky, 2011a; Bessho & Bhattacharjee, 2012; Werner et al., 2014; Guo et al., 2014), and so most of the electron "thermal" energy is carried by the highest energy electrons. Making use of equations 2.1 & 2.3 for magnetic field strength and electron LF, we obtain an expression for the maximum synchrotron frequency

$$\nu^{syn}_{max} \sim \frac{qL^{1/2}\sigma^2(m_p/m_e)^2}{2\pi m_e c^{3/2}R(1+z)} = (2.2\times10^2\ \mathrm{eV})\frac{\sigma^2 L^{1/2}_{48}}{R_{15}(1+z)}. \tag{2.5}$$

A more accurate estimate for ν^{syn}_{max} that takes into account radiative losses are presented in §2.2.1. The synchrotron photons will be inverse-Compton (IC) scattered to higher energies by electrons producing these photons, and the maximum IC photon energy in observer frame is the smaller of $m_e c^2 \gamma'_e \Gamma/(1+z)$ and $\sim \nu \gamma'^2_{max}$.

The specific flux at frequency ν, i.e. flux per unit frequency, in the observer frame is

$$f_\nu \approx \left[\frac{q^3 B'_0 \Gamma N_e}{m_e c^2}\right] \frac{1+z}{4\pi d_L^2}, \tag{2.6}$$

where N_e is the total number of electrons (isotropic equivalent) in the causally connected part of the jet with thermal LF $\geq \gamma_e$, and d_L is the luminosity distance to the source. We can calculate the number of electrons needed to produce a given observed flux by combining equations (2.1)–(2.6):

$$N_e \approx 1.2 \times 10^{49} f_{\nu,mJy} L_{48}^{-1/2} R_{15} d_{L,28}^2 (1+z)^{-1}, \tag{2.7}$$

The optical depth of these electrons to Thomson scattering is,

$$\tau_T \approx \frac{\sigma_T N_e}{4\pi R^2} = 8 \times 10^{-7}\, f_{\nu,mJy} L_{48}^{-1/2} R_{15}^{-1} d_{L,28}^2 (1+z)^{-1}, \tag{2.8}$$

and their "thermal" LF and kinetic energy luminosity they carry are

$$\gamma'_e \approx \left[\frac{2\pi m_e \nu R c^{3/2}}{q L^{1/2} (1+z)^{-1}}\right]^{1/2} = 4 \times 10^3 \frac{[R_{15} \nu_{kev} (1+z)]^{1/2}}{L_{48}^{1/4}}, \tag{2.9}$$

$$\begin{aligned} L_e &\approx \frac{N_e m_e c^3 \gamma_e \Gamma}{(R/\Gamma^2)} \\ &= (1.2 \times 10^{42}\ \mathrm{erg\,s^{-1}}) \frac{\Gamma^3 f_{\nu,mJy} R_{15}^{1/2} d_{L,28}^2 \nu_{keV}^{1/2}}{L_{48}^{3/4} (1+z)^{1/2}}, \end{aligned} \tag{2.10}$$

where ν_{keV} is photon frequency (in units of 1 keV) for which the observed specific flux is $f_{\nu,mJy}$. Considering that the energy carried by electrons cannot exceed the energy in magnetic fields for a Poynting jet, we find

$$L_e/L \lesssim 1 \quad \Longrightarrow \quad \Gamma \lesssim 90\, \frac{L_{48}^{7/12}(1+z)^{1/6}}{f_{\nu,mJy}^{1/3} R_{15}^{1/6} d_{L,28}^{2/3} \nu_{keV}^{1/6}}. \tag{2.11}$$

The reason for the approximate inequality sign in the above equation is because magnetic fields of a Poynting jet could be compressed by a factor a few and thus L_e could in principle exceed L by order unity.

If we consider that there are η_p protons for every electron[4] that radiates at frequency ν, then the kinetic energy luminosity carried by cold protons is

$$L_p \approx \frac{N_e \eta_p m_p c^3 \Gamma}{(R/\Gamma^2)} \approx (5\times 10^{41}\ \mathrm{erg\,s^{-1}}) \frac{\Gamma^3 \eta_p f_{\nu,mJy} d_{L,28}^2}{L_{48}^{1/2}(1+z)}. \tag{2.12}$$

Therefore, the magnetization parameter for the jet at location where jet magnetic energy is dissipated and radiation is produced is given by

$$\sigma(R) \approx \frac{L}{L_p} \approx \frac{2\times 10^6}{\eta_p \Gamma^3} f_{\nu,mJy}^{-1} L_{48}^{3/2} d_{L,28}^{-2}(1+z). \tag{2.13}$$

If 10% of electrons in the jet are accelerated. i.e. $\eta_p = 10$, and $\Gamma = 20$, then $\sigma(R) \approx 25$. And that means that the magnetization parameter at the let launching site where $\Gamma \sim 1$ is $\sigma_0 \approx \Gamma(R)\sigma(R) \sim 500$.

2.2.1 Particle acceleration in current sheets

Consider an electron undergoing acceleration in a reconnection region where the electric field is $\vec{E}'$, and the magnetic field is $\vec{B}'$. In the absence

---

[4] $\eta_p > 1$ when only a fraction of electrons in the jet are accelerated.

of a guide field, the magnetic field vanishes at the X-point, and far away from it its magnitude is B'_0, but otherwise at this stage we place no further constraint on the electric and magnetic fields. The electron starting from some place in the vicinity of the X-point is accelerated, and as it moves away it finds the strength of the magnetic field increasing. At some point when the magnetic field becomes sufficiently strong, which will be quantified shortly, the acceleration ceases if $\vec{E}' \cdot \vec{B}' = 0$. However, even well before this happens, the electron could stop accelerating due to radiative losses which will determine its terminal Lorentz factor. We consider this interplay between acceleration and radiative losses to determine maximum electron LF.

It is best to view the motion of a particle acted upon by $\vec{E}'$ and $\vec{B}'$ from a frame where the fields point in the same direction (which is always possible except when $|\vec{E}'| = |\vec{B}'|$ and the two fields are exactly perpendicular to each other). This special frame where $\vec{E}'' \parallel \vec{B}''$ will be referred to as the AF frame (Aligned Fields frame). There are two quadratic Lorentz invariant functions of $\vec{E}'$ and $\vec{B}'$:

$$\begin{aligned} I_1 &= -\epsilon_{\alpha\beta\gamma\delta} F^{\alpha\beta} F^{\gamma\delta}/8 = \vec{E}' \cdot \vec{B}' \quad \textit{and} \\ I_2 &= -F^{\alpha\beta} F_{\alpha\beta}/2 = E'^2 - B'^2, \end{aligned} \tag{2.14}$$

where $F_{\alpha\beta}$ is the electromagnetic tensor (anti-symmetric 2-form). Since $\vec{E}' \cdot \vec{B}'$ is Lorentz invariant, if there is a non-zero component of magnetic field in the direction of the electric field in one inertial frame, there will be a non-zero component in all inertial frames. However, the component of magnetic field perpendicular to the electric field can be made to vanish by frame transformation if $E'^2 - B'^2 > 0$, or the electric field perpendicular to magnetic field can be transformed away in an appropriate frame when $E'^2 - B'^2 < 0$. The point is that there exists an inertial frame (AF) where the transformed electric and magnetic fields are parallel, and the motion of the electron is the AF frame is as simple as can be — the electron momentum parallel to the fields increases linearly with time (if the electric field is non-zero in this frame), and the perpendicular component of momentum has a constant magnitude (time independent) and it rotates about the magnetic field at a constant rate.

The simplest way to get to the AF frame is by a Lorentz boost in the direction $\vec{E}' \times \vec{B}'$; if $\vec{E}' \times \vec{B}' = 0$, then obviously no Lorentz transformation is needed as we are already in a frame where the two fields are either parallel or one of them is zero. A straightforward Lorentz transformation algebra shows that the speed of the Lorentz boost required so that the fields are parallel in the new frame is

$$\beta_{LT} = \frac{(1+\epsilon^2) - \left[(1-\epsilon^2)^2 + 4\epsilon^2\cos^2\theta'\right]^{1/2}}{2\epsilon\sin\theta'} \tag{2.15}$$

where

$$\epsilon \equiv \frac{E'}{B'}, \quad \cos\theta' = \frac{\vec{E}'\cdot\vec{B}'}{|\vec{E}'||\vec{B}'|}. \tag{2.16}$$

Figure 2.2 shows the LF of needed boost as a function of ϵ for a few different values of θ'; a simple analytical expression for $\epsilon \gg 1$ and $\epsilon \ll 1$ is

$$\beta_{LT} \approx \min\left\{\epsilon, \epsilon^{-1}\right\}\sin\theta', \tag{2.17}$$

which turns out to be exact (as opposed to approximate) for all values of ϵ for the special case of $\theta' = \pi/2$.

The electric field in the new frame follows from the two Lorentz invariant quantities mentioned above and is given by

$$E''^2 = \frac{I_2 + \sqrt{4I_1^2 + I_2^2}}{2}, \tag{2.18}$$

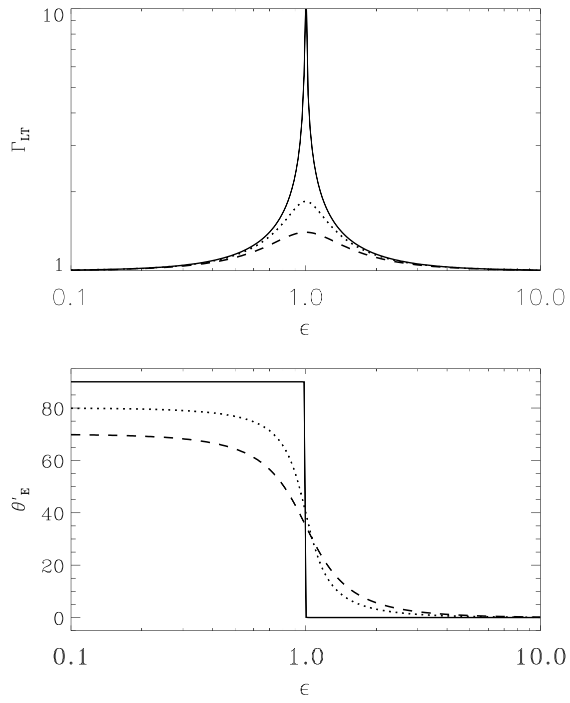

Figure 2.2: The Lorentz factor of the inertial frame (wrt jet rest-frame) in which the electric and magnetic fields in some region of current sheet are parallel to each other is shown in the upper panel as a function of $\epsilon \equiv E'/B'$; $\Gamma_{LT} \equiv (1-\beta_{LT}^2)^{-1/2}$, where β_{LT} is given by equation (2.15). The three different curves correspond to three different angles (θ') between electric and magnetic fields; $\theta' = 70^o$ (dashed curve), 80^o (dotted line), and 90^o (solid line). Note that $\Gamma_{LT} \sim 1$ except when electric field is almost exactly perpendicular to the magnetic field and the strengths of these fields are about the same. A small Γ_{LT} makes it rather easy to carry out calculations in the AF frame where $\vec{E}'' \parallel \vec{B}''$ and transform variables back to the jet comoving frame. The lower panel shows the angle (measured in the jet comoving frame in degrees) by which the electric field direction is rotated in the AF frame for three different values of θ' which are same as in the upper panel; when the electric field vanishes is the AF frame then the angle is the rotation for magnetic field plus $\pi/2$.

and the magnetic field is

$$B'' = \frac{I_1}{E''}, \tag{2.19}$$

where I_1 and I_2 are defined in equation (2.14). The angle between the aligned electro-magnetic field in the AF frame and the electric field in the jet frame can be easily calculated and is

$$\cos\theta'_E = \frac{(\epsilon - \beta_{LT}\sin\theta')}{\sqrt{\epsilon^2 + \beta_{LT}^2 - 2\epsilon\beta_{LT}\sin\theta'}}, \tag{2.20}$$

The lower panel of Figure 2.2 shows θ'_E as a function of ϵ for a few different values of θ'.

With these results in hand, we are ready to describe particle acceleration in a current sheet. Consider a charged particle in the vicinity of the X-point where $E' \gg B'$. We can transform away the perpendicular component of the magnetic field by going to the AF frame, and in this frame the particle Lorentz factor γ''_e (the double prime emphasizes that we are in a different inertial frame, and not the jet comoving frame) increases as $qE''t''/(m_e c^2)$, which can be rewritten from the point of view of the jet frame as

$$\gamma'_e \approx \frac{q\epsilon_0 B'_0 \ell'}{m_e c^2}, \tag{2.21}$$

where ℓ' is the distance the electron has traveled along the direction of the electric field from its starting position in the jet comoving frame, and

$$\epsilon_0 \equiv E'/B'_0. \tag{2.22}$$

As the electron travels further and further away from the X-point, it feels the strength of the magnetic field increase and at some point when B' becomes stronger than E' the electron is no longer accelerated (unless $\vec{E}' \cdot \vec{B}' \neq 0$) and its momentum vector gyrates about the magnetic field and the LF oscillations and drifts slowly with time. This generic behavior can been in figure (2.3) where numerical result for particle motion in a current sheet is presented.

If the length of the region where $E' > B'$ is ℓ'_E, then the maximum LF of electron $\gamma'_{max} \sim q\epsilon_0 B'_0 \ell'_E/(m_e c^2)$; it should be noted that $\ell'_E \overset{\propto}{\sim} \epsilon_0$ for a magnetic field configuration where B' increases linearly with distance from the X-point, and thus $\gamma'_{max} \overset{\propto}{\sim} \epsilon_0^2$ (Larrabee et al., 2003, see *e.g.*). However, two effects can substantially limit electron LF below this value. One of which is *"global"* energy conservation, which provides a limit for γ'_{max} as described by equation (2.3). And the other is radiative losses — synchrotron and inverse-Compton (IC) for systems of interest to us — that could restrict particle LF further. We discuss how radiative losses effect γ'_{max} below.

Viewed from the AF frame where $\vec{E}'' \parallel \vec{B}''$, the electron suffers radiative losses due to acceleration along the electric field direction, gyration about the magnetic field, and inverse-Compton scatterings. We evaluate each of these to determine the dominant loss mechanism, and its effect on γ'_{max}. The energy loss rate is calculated by first assuming that the magnetic field lines are parallel, i.e. $\vec{B}' \cdot \vec{\nabla}\vec{B}' = 0$, and the electric field is nearly uniform. This estimate is then improved by relaxing these assumptions and by considering the more realistic possibility that magnetic field lines have non-zero curvature, and that the electric field has spacial fluctuations in the acceleration region.

The power radiated due to particle acceleration along the electric field can be calculated using the Larmor's formula. The momentum vector of the electron in the AF frame is nearly parallel to $\vec{E}''$ since it is being accelerated along the electric field and the magnetic field is parallel to $\vec{E}''$ in this frame. Therefore, the electric field in the instantaneous rest-frame of electron is also

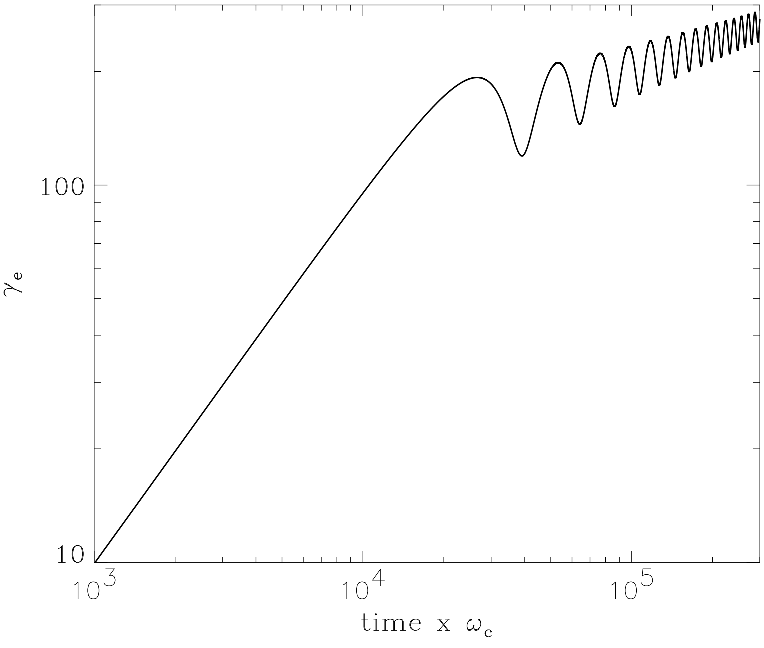

Figure 2.3: Acceleration of an electron in a current sheet is shown as a function of time in unit of $1/\omega_c$, where $\omega_c = qB'_0/(m_e c)$ is Larmor frequency. The electric and magnetic field configurations in the current sheet are taken from Larrabee et al. (2003), i.e. sheet lies in the x-y plane with the electric field pointing in the x-direction and has a constant magnitude $E' = \epsilon_0 B'_0$, and the vector potential is $\vec{A} = [B'_0(y^2 - z^2)/2\ell'_s]\hat{z}$; we took $\epsilon_0 = 0.01$ and the length of the "sheet" $\ell'_s \omega_c/c = 5 \times 10^5$ for this calculation. The particle started out in the $z = 0$ plane with initial velocity of zero. The LF of the electron (γ'_e) increases linearly with time as long as it is in the region where $E' > B'$ (which is for about 2x$10^4\omega_c^{-1}$ for the parameters we have chosen for this calculation), and afterward when $B' > E'$ the acceleration ceases and the electron gyrates about the magnetic field. These results are entirely consistent with analytical calculations presented in this section.

$\vec{E}''$, and the magnitude of its acceleration in this frame is qE''/m_e. It then follows from Larmor's formula that the power radiated (which is a Lorentz invariant quantity) is $\sigma_T E''^2 c/4\pi \sim \sigma_T \epsilon_0^2 B_0'^2 c/4\pi$; from equation (2.15) and Fig. 2.2 we know that $\Gamma_{LT} \sim 1$ for $\epsilon > 2$, and hence $E'' \sim E' = \epsilon_0 B_0'$. This rate of loss of energy is independent of electron LF, and so the maximum electron LF in this case is bounded only by the size of the acceleration region.

The synchrotron loss rate due to electron gyration about the magnetic field is $\sigma_T B''^2 \gamma_\perp''^2 \beta_\perp''^2 c/(6\pi)$; where $m_e c \gamma_\perp'' \beta_\perp''$ is the 4-momentum of the electron perpendicular to the magnetic field. In the region where particles are undergoing acceleration, the magnetic field in the AF frame (B'') either vanishes (if $\vec{E}' \cdot \vec{B}' = 0$) or is parallel to $\vec{E}'$, and in either case the value of $\gamma_\perp'' \beta_\perp''$ does not change with time even as the electron continues to accelerate. Thus, the synchrotron loss rate (like the loss rate due to acceleration along the electric field) is nearly independent of electron momentum, which continues to increase linearly with time along $\vec{E}'$ while the electron is in the acceleration region.

For realistic astrophysical systems we don't expect the magnetic and electric field lines to be perfectly straight in the acceleration region. The curvature of field lines and the variation of E'/B' with distance from the X-point causes the direction of $\vec{E}''$ to change (see Fig. 2.2 for the dependence of θ_E' on E'/B'), and therefore particle momentum vector is also rotated. Due to these effects $\gamma_\perp''$ is no longer independent of time, and in fact even a modest curvature in $\vec{E}'$ would lead to $\gamma_\perp'' \sim \gamma_\parallel''$. In this case the synchrotron loss estimated above increases by a factor γ'^2 (the loss due to acceleration along $\vec{E}'$ increases by a similar factor) and is given by

$$\frac{d m_e c^2 \gamma'^2}{dt'} \sim \sigma_T (\epsilon_0^2 + \sin^2 \theta_g') B_0'^2 \gamma'^2 c/6\pi \sim \sigma_T B_0'^2 \gamma'^2 c/6\pi \qquad (2.23)$$

where $B_0' \sin\theta_g'$ is the strength of the guide field. From here on we assume that the guide field is not much smaller than B_0' and therefore particle acceleration is dominated by electric field parallel to the magnetic field.

The inverse-Compton loss rate is proportional to the energy density of photons, which is closely related to magnetic field dissipation. Photons are produced via the synchrotron process in acceleration regions and also outside it. Assuming that a fraction ψ_B of magnetic field energy in a causally connected region of size R/Γ is dissipated in a dynamical time and converted to radiation, the photon energy density in the comoving jet frame is[5] $\psi_B B_0'^2/8\pi$, and therefore the IC loss rate is

$$\frac{d m_e c^2 \gamma'^2}{dt'} = \sigma_T \psi_B B_0'^2 \gamma'^2 c/6\pi. \tag{2.24}$$

Equating the rate of energy gain for an electron as it is accelerated along the electric field with the rate of radiative loses we arrive at the following equation for the maximum value for LF

$$q\epsilon_0 B_0' c \approx \frac{\sigma_T B_0'^2 \gamma_{max}'^2 c(1+\psi_B)}{6\pi}. \tag{2.25}$$

Or

$$\gamma_{max}' \approx 1.5\times 10^7 \epsilon_0^{1/2}(1+\psi_B)^{-1/2}\Gamma_2^{1/2} L_{48}^{-1/4} R_{15}^{1/2}, \tag{2.26}$$

where we made use of equation (2.1) to substitute for B_0', and we are considering the case where $\vec{E}'\cdot\vec{B}' \neq 0$. The maximum electron LF is the smaller of values given in equations (2.3) and (2.26).

---

[5] Photons produced by the dissipation of magnetic field in a region of size R/Γ in the comoving frame travel a distance in a dynamical time which is also R/Γ, and hence all the radiative energy is confined to a volume $\sim R^3/\Gamma^3$.

The distance an electron travels to get accelerated to γ_{max} is

$$\begin{aligned}
\ell'_a &\approx \frac{\gamma'_{max} m_e c^2}{q\epsilon_0 B'_0} \\
&\approx \min\left\{\begin{array}{l} (4.7\times 10^8\ \mathrm{cm})\, \frac{\Gamma_2^{3/2} L_{48}^{-3/4} R_{15}^{3/2}}{\epsilon_0^{1/2}(1+\psi_B)^{1/2}}, \\ \\ (5.2\times 10^4\ \mathrm{cm})\, \epsilon_0^{-1}\sigma L_{48}^{-1/2}\Gamma_2 R_{15} \end{array}\right\} \qquad (2.27)
\end{aligned}$$

The synchrotron photon energy corresponding to γ'_{max} is

$$\nu_{max} \sim \min\left\{\begin{array}{l} (150\ \mathrm{MeV})\Gamma\epsilon_0(1+\psi_B)^{-1}, \\ \\ (200\ \mathrm{eV})\ \sigma^2 L_{48}^{1/2} R_{15}^{-1} \end{array}\right\} \qquad (2.28)$$

The minimum electron LF can be obtained by taking the length of the acceleration region to be no less than proton Larmor radius. The minimum electron LF is then $\gamma'_{min} \sim \epsilon_0^2(m_p/m_e)$.

2.2.2 Electron distribution function

Simulations of particle acceleration in a reconnection layer show that the energy distribution is a hard powerlaw function below γ'_{max} and exponentially cut-off above it, i.e. $dn'_e/d\gamma'_e \propto \gamma_e'^{-p_0}$, for $\gamma'_e < \gamma'_{max}$ with $p_0 < 2$.

When we add up particle distribution functions in all PASs within the causally connected region of the jet at the radius where a good fraction of magnetic energy in the jet is dissipated, the resulting distribution is

$$\frac{dn'_e}{d\gamma'_e} \propto \gamma_e'^{-p} \qquad \text{for} \quad \gamma'_{min} \lesssim \gamma'_e \lesssim \gamma'_p. \qquad (2.29)$$

The value of p depends on how many electrons pass through PASs which can accelerate them to LF γ'_e; if the number of PASs increases rapidly with decreasing γ'_{max} then $p > p_0$. The electron distribution below γ'_{min} is either cutoff or drops off such that the total number of electrons with $\gamma'_e < \gamma'_{min}$ is small and can be ignored. The distribution above γ'_p also falls off more rapidly than $\gamma_e'^{-2}$.

Let us assume that electrons spend an average of t'_{cs} time in an acceleration region which is larger than ℓ'_a/c; the average is taken over all particle acceleration sites or PASs in causally connected part of the jet. Furthermore, the total number of electrons injected into these acceleration regions, in the causally connected part of the jet, per unit time is $\dot{N}'_{e,cs}$. The average rate at which particles exit PASs should also be $\dot{N}'_{e,cs}$. Particles outside PASs cool down radiatively and therefore the particle distribution outside is much steeper. We calculate this distribution, and estimate the synchrotron flux from electrons inside and outside PASs.

If the average time spent by electrons outside PASs is t'_{dz}, then in that time electrons cool down to LF

$$\gamma'_c \approx \frac{6\pi m_e c}{\sigma_T B_0'^2 t'_{dz}} \approx \frac{6\pi m_e c^3 \Gamma^3 R \xi}{\sigma_T L} \approx 7\xi \Gamma_1^3 R_{16} L_{48}^{-1}, \tag{2.30}$$

where

$$\xi \equiv \frac{R}{c\Gamma t'_{dz}}, \tag{2.31}$$

is the ratio of dynamical time in jet comoving frame and t'_{dz}.

The electron distribution outside PASs is obtained by solving

$$\frac{\partial (dN'_{e,dz}/d\gamma'_e)}{\partial t'} + \frac{\partial \dot{\gamma}'_e (dN'_{e,dz}/d\gamma'_e)}{\partial \gamma'_e} = S'(\gamma'_e), \tag{2.32}$$

where the source function is

$$S'(\gamma'_e) \approx \frac{(p-1)\dot{N}'_{e,cs}}{\gamma'_{min}} \left(\frac{\gamma'_e}{\gamma'_{min}}\right)^{-p} \quad \text{for } \gamma'_{min} \le \gamma'_e \le \gamma'_p \tag{2.33}$$

$p > 1$, $\dot{N}'_{e,cs}$ is the rate at which electrons with Lorentz factors $\geq \gamma'_{min}$ leave acceleration regions and enter the surrounding medium, and

$$\dot{\gamma}'_e = -\frac{\sigma_T B'^2_0 \gamma'^2_e}{6\pi m_e c}. \tag{2.34}$$

A quasi-steady state solution is reasonable to consider when the time it takes for a typical PAS in the jet to form and disappears is much shorter than the dynamical time, and there are many PASs in the causally connected region of the jet that contribute to particle acceleration and radiation; the average of all these PASs can be taken to be roughly constant for about a dynamical time. The solution of equation (2.32) for $p \geq 1$, in quasi-steady state, is easy to obtain and for $\gamma'_c < \gamma'_{min}$ is given by

$$\frac{dN'_{e,dz}}{d\gamma'_e} \approx \frac{t'_{dz}\dot{N}'_{e,cs}}{\gamma'_c} \begin{cases} \frac{\gamma'^2_c \gamma'^{-p-1}_e}{\gamma'^{-p+1}_{min}} & \gamma'_{min} \leq \gamma'_e \leq \gamma'_p \\ \left(\frac{\gamma'_e}{\gamma'_c}\right)^{-2} & \gamma'_c \leq \gamma'_e \leq \gamma'_{min} \end{cases} \tag{2.35}$$

The above derivation assumes $\gamma'_p \gg \gamma'_c$, which should be a good approximation considering that $\gamma'_p \sim \gamma'_{max} \sim 10^7$ (eq. 2.26) and $\gamma'_c \sim 10$ (eq. 2.30). The distribution is effectively cutoff above γ'_p outside the PASs since electrons of this high energy cool efficiently and their LF drops below γ'_p quickly. The distribution function for the case where $\gamma'_p > \gamma'_c > \gamma'_{min}$ is

$$\frac{dN'_{e,dz}}{d\gamma'_e} \approx t'_{dz}\dot{N}'_{e,cs} \begin{cases} \frac{\gamma'_c \gamma'^{-p-1}_e}{\gamma'^{-p+1}_{min}} & \gamma'_c \leq \gamma'_e \leq \gamma'_p \\ \frac{\gamma'^{-p}_e}{\gamma'^{-p+1}_{min}} & \gamma'_{min} \leq \gamma'_e \leq \gamma'_c \end{cases} \tag{2.36}$$

For $p < 1$, the source function is

$$S'(\gamma'_e) \sim \frac{(1-p)\dot{N}'_{e,cs}}{\gamma'_p} \left(\frac{\gamma'_e}{\gamma'_p}\right)^{-p} \quad \text{for } \gamma'_{min} \leq \gamma'_e \leq \gamma'_p \tag{2.37}$$

and therefore most of the electrons are at $\gamma'_e \sim \gamma'_p$. The solution of equation (2.32) using the above source function for $\gamma'_c < \gamma'_{min}$ is

$$\frac{dN'_{e,dz}}{d\gamma'_e} \approx \frac{t'_{dz}\dot{N}'_{e,cs}}{\gamma'_c}\left(\frac{\gamma'_e}{\gamma'_c}\right)^{-2} \qquad \text{for} \quad \gamma'_c < \gamma'_e \lesssim \gamma'_p. \tag{2.38}$$

And the distribution function when $\gamma'_p > \gamma'_c > \gamma'_{min}$ is given by

$$\frac{dN'_{e,dz}}{d\gamma'_e} \approx t'_{dz}\dot{N}'_{e,cs} \begin{cases} \frac{\gamma'_c}{\gamma'^2_e} & \gamma'_c \ll \gamma'_e \leq \gamma'_p \\ \frac{1}{\gamma'_p}\left(\frac{\gamma'_e}{\gamma'_p}\right)^{-p} & \gamma'_{min} \leq \gamma'_e \ll \gamma'_c \end{cases} \tag{2.39}$$

The apparent discontinuity of the distribution function in equation (2.39) at $\gamma'_e = \gamma'_c$ is because the two branches of solutions are inaccurate as γ'_e approaches γ'_c. However, a steep drop off of the distribution function just below γ'_c is physical. The drop off is due to the fact that electrons with LF $\sim \gamma'_p$ (which are a majority of the electrons entering the medium in between PASs when $p < 1$) radiatively cool down to LF $\sim \gamma'_c$ in the available time t'_{dz}, and hence there is an accumulation of electrons in the neighborhood of γ'_c and that is responsible for a drop in the distribution function just below this LF.

2.2.3 Synchrotron and IC spectra

The synchrotron spectrum due to radiation from electrons inside PASs, within the causally connected region of the jet, is $f_\nu \propto \nu^{-(p-1)/2}$ for $\nu \lesssim \nu_p$; where

$$\nu_p \approx \frac{qB'_0\gamma'^2_p\Gamma}{2\pi m_e c(1+z)} \approx \frac{qL^{1/2}\gamma'^2_p}{2\pi m_e c^{3/2}R(1+z)} \tag{2.40}$$

is synchrotron frequency in the observer frame corresponding to electron LF γ'_p; the electron distribution function starts to fall off faster than γ'^{-p}_e for $\gamma'_e > \gamma'_p$. The specific flux (flux per unit frequency) at ν_p due to PAS electrons is (*e.g.*, Rybicki & Lightman, 1986)

$$
\begin{aligned}
f_{cs}(\nu_p) &\sim \frac{q^3 B_0' \Gamma N_e(\gtrsim \gamma_p')}{m_e c^2} \frac{1+z}{4\pi d_L^2} \\
&\sim \frac{q^3 L^{1/2} \dot{N}_{e,cs}' t_{cs}'}{m_e c^{5/2} R} \frac{1+z}{4\pi d_L^2} \begin{cases} 1 & p < 1 \\ \left[\frac{\gamma_p'}{\gamma_{min}'}\right]^{1-p} & p > 1 \end{cases}
\end{aligned} \tag{2.41}
$$

where $N_e(\gtrsim \gamma_p')$ is the total number of electrons inside PASs with LF $\gtrsim \gamma_p'$ (which is t_{cs}' times the integral of the source function given in equations 2.33 & 2.37), t_{cs}' is the average time electrons spend in acceleration regions, and d_L is the luminosity distance of the source at redshift z.

The synchrotron spectrum due to electrons outside PASs is either $f_\nu \propto \nu^{-p/2}$, $\nu^{-1/2}$ or $\nu^{-(p-1)/2}$ depending on whether p is larger or smaller than 1, and the ordering of ν and synchrotron characteristic frequencies.

The synchrotron flux at ν_p due to electrons outside PASs can be estimated using the distribution function calculated in the previous subsection (eqs. 2.35, 2.36, 2.38, 2.39). For the case we are considering where the guide field strength is of order B_0', the magnetic fields outside and inside PAS are of similar strength, and in that case the flux at ν_p due to electrons outside PASs is

$$
f_{dz}(\nu_p) \sim f_{cs}(\nu_p) \left[\frac{t_{cool}'(\gamma_p')}{t_{cs}'}\right], \sim f_{cs}(\nu_p) \left[\frac{t_{dz}' \gamma_c'}{t_{cs}' \gamma_p'}\right] \tag{2.42}
$$

where $f_{cs}(\nu_p)$ is synchrotron flux at ν_p due to electrons inside PASs (see eq. 2.41), and

$$
t_{cool}'(\gamma_p') = \frac{6\pi m_e c}{\sigma_T B_0'^2 \gamma_p'} = (2.3\,\mathrm{s}) L_{48}^{-1} \gamma_{p,5}'^{-1} \Gamma_2^2 R_{15}^2 \tag{2.43}
$$

is synchrotron cooling time for an electron of LF γ_p' outside PASs. Therefore, the ratio of synchrotron flux at ν_p due to electrons inside and outside PASs is

$$
\mathcal{R}_p \equiv \frac{f_{cs}(\nu_p)}{f_{dz}(\nu_p)} \sim \frac{t_{cs}'}{t_{cool}'(\gamma_p')}. \tag{2.44}
$$

At a frequency ν between ν_{min} and ν_p (assuming that $\nu_{min} > \nu_c$), the ratio of the flux from the two regions is[6]

$$\frac{f_{cs}(\nu)}{f_{dz}(\nu)} \approx \mathcal{R}_p \begin{cases} (\nu/\nu_p)^{(2-p)/2} & 1/3 < p < 1 \\ \\ (\nu/\nu_p)^{1/2} & p > 1 \end{cases} \tag{2.45}$$

And the flux ratio at a frequency such that $\nu_c < \nu < \nu_{min}$ is

$$\frac{f_{cs}(\nu)}{f_{dz}(\nu)} \approx \mathcal{R}_p \begin{cases} \left(\frac{\nu}{\nu_{min}}\right)^{5/6} \left[\frac{\nu_{min}}{\nu_p}\right]^{(2-p)/2} & 1/3 < p < 1 \\ \\ \left(\frac{\nu}{\nu_{min}}\right)^{5/6} \left[\frac{\nu_{min}}{\nu_p}\right]^{1/2} & p > 1 \end{cases} \tag{2.46}$$

The observed spectrum is a superposition of synchrotron radiation from electrons in PASs and electrons outside acceleration regions. We have provided all the relevant equations to determine specific flux at an arbitrary frequency from these two sources. We note that if the observed flux between ν_{min} and ν_p is dominated by synchrotron radiation within PASs then the spectrum would be $f_\nu \propto \nu^{-(p-1)/2}$, which is harder by $\nu^{1/2}$ than the case where the flux comes mostly from electrons in the medium between PASs. Figure 2.4 shows the relative contributions of the two sources (upper panel), and the spectral index of the observed flux (lower panel), as a function of frequency. The figure clearly shows that the flux at ν_p is dominated by electrons in PASs and thus the spectral index is harder. Electrons outside PASs make the dominant contribution to the observed flux at sufficiently low frequencies (below $\nu_p/10^2$ for the parameters considered in Fig. 2.4), and therefore the spectrum is softer. This

---

[6] ν_{min} and ν_c are synchrotron frequencies in the observer frame for electrons of Lorentz factors γ'_{min} and γ'_c respectively in a magnetic field of strength B'_0; γ'_c is given by eq. 2.30, and γ'_{min} is the electron LF below which the average distribution function inside PASs either drops off or rises less rapidly than $\gamma_e'^{-p}$.

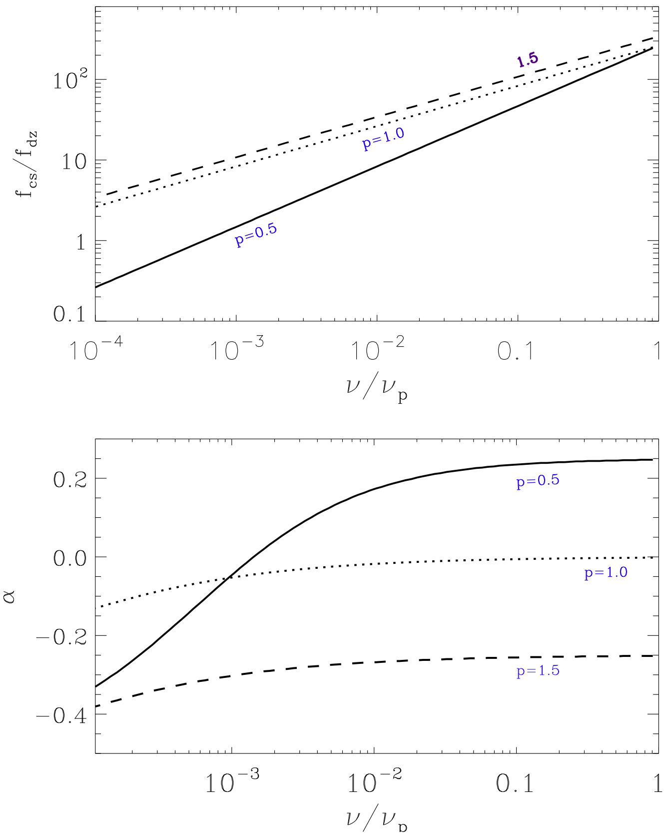

Figure 2.4: The upper panel shows the ratio of synchrotron flux from electrons in acceleration regions (PASs) and electrons in regions outside; three different lines correspond to three different values of p: 0.5 (solid line), 1.0 (dotted line) and 1.5 (dashed line). The parameters for these calculations are: $L = 10^{48}$erg/s, $\Gamma = 10$, $\sigma = 10^2$, $R = 10^{15}$cm, $\epsilon_0 = 0.1$, $\psi_B = 0.1$, $\gamma'_p = \gamma'_{max}$, $\gamma'_{min} = \gamma'_{max}/10^2$, and $t'_{cs} = 10^{-3} \times R/(c\Gamma)$. The lower panel shows the spectral index for the observed flux, i.e. $\alpha = d\ln(f_{cs} + f_{dz})/d\ln\nu$ for the same three values of p. Note that for the parameters chosen for these calculations the observed flux is dominated by electrons radiating in PASs for $\nu \gtrsim 10^{-3}\nu_p$ and therefore the spectral index in this frequency range is $\alpha \approx -(p-1)/2$, i.e. the spectrum is hard.

behavior — softening of spectrum with decreasing frequency — is opposite to what we find when particles are accelerated in shocks, and a spectral softening with decreasing energy might be a way to determine whether magnetic or shock dissipation of jet energy is responsible for the observed radiation.

The ratio of the luminosity in synchrotron and IC radiations is equal to the ratio of energy densities in magnetic field and photons. Since only a small fraction of energy in magnetic fields in dissipated in current sheets[7], it is expected that the IC luminosity of a Poynting jet would be smaller than the synchrotron luminosity. The IC spectrum, or to be precise synchrotron-self-Compton spectrum, is straightforward to calculate using the results for particle distribution and synchrotron spectrum described above.

2.2.4 Constraint on the number of current sheets in the jet

The radius interval where conversion of magnetic energy to thermal energy for a Poynting jet takes place depends on the magnetic field configuration and instabilities that develop in the jet. These are very difficult to calculate with any confidence. However, some general considerations described in this subsection provide broad guidance which can be used to constrain the dissipation radius and the number of current sheets in the jet.

Consider a short segment of the jet that was launched at radius R_0. The dissipation of magnetic energy in this segment could take place anywhere between R_0 and $\sim R_d$ (the deceleration radius of the jet), either gradually over a long distance interval or suddenly within a short distance. Once the recon-

---

[7] In general, it is highly unlikely for magnetic fields on the opposite sides of currents sheets to be exactly anti-parallel, and that limits the efficiency for converting magnetic energy to particle energy and radiation.

nection gets started at one location in the jet, it could trigger magnetic field dissipation at other sites — possibly as a result of plasma outflow from this region or magnetic field reconfiguration propagating at Alfv́en speed and triggering reconnection at other sites — and these *secondary* reconnection sites lie in a region of the jet that is in causal contact with the current sheet triggering these events. It is unlikely that most of the energy of this segment of the jet under consideration will be dissipated at a radius smaller than $(\delta t)c\Gamma^2$ because of causality considerations (provided of course that different parts of this segment of the jet don't independently develop instability and/or reconnection centers). We can describe the dissipation with radius as a monotonically increasing function of radius, $\zeta_B(R)$; ζ_B is the fraction of the magnetic energy in the segment that is dissipated or converted to bulk kinetic energy of the jet.

For example, in magnetic reconnection in a jet consisting of striped magnetic wind geometry (magnetic fields reversing direction over distance of r_0 in the lab frame), $\zeta_B \propto R^{1/3}$ (*e.g.*, Drenkhahn, 2002; Kumar & Zhang, 2015), and the process is completed at a radius $R_c \sim r_0\Gamma^2/\epsilon_0$; where ϵ_0 as defined in §2.2.1 is the ratio of electric and magnetic fields and $v'_p \sim \epsilon_0 c$ is the speed for plasma flow into current sheets. So, although, the magnetic field dissipation process in this case is slow and extends over a large distance interval of R_0 — $r_0\Gamma^2/\epsilon_0 \gg R_0$, roughly half of the magnetic energy is in fact dissipated within a factor of a few of $r_0\Gamma^2/\epsilon_0$. This result follows from causality, i.e., the size of the region where magnetic field is dissipated cannot increase at a speed faster than light, and hence the radial width of region where field has been dissipated grows proportional to R/Γ (in jet comoving frame) and that is the reason that a good fraction of magnetic energy dissipation occurs within a factor a few of the terminal radius where the dissipation process is completed. This property is likely to be generic, and independent of magnetic field geometry and reconnection model.

Current sheets are likely to form and disappear on a time short compared with the dynamical time ($R/(c\Gamma)$ in jet comoving frame). We envision that there are an average $\aleph_s$ PASs present in the region at any given time, for a time duration $\sim R/(c\Gamma)$, and the average length of these current sheets in jet comoving frame is ℓ'_s.

The total volume of plasma in the jet in the causally connected region at R is

$$\mathcal{V}'_c \sim (R/\Gamma)^3, \tag{2.47}$$

provided that the jet opening angle is $> \theta_j$. Since plasma flows into current sheets at speed $v'_p \sim \epsilon_0 c$, the total volume of plasma passing through current sheets in a dynamical time is

$$\mathcal{V}'_{plasma,cs} \sim \aleph_s {\ell'_s}^2 \epsilon_0 (R/\Gamma). \tag{2.48}$$

If the fraction of the magnetic energy in the jet dissipated in this region is $\zeta_B(R)$, then that means that the total volume of plasma passing through current sheets in volume $\mathcal{V}'_c$ should be $\zeta_B \mathcal{V}'_c$. Thus, we obtain the number of PASs in the region to be

$$\aleph_s \sim [\zeta_B(R)/\epsilon_0] \left\{R/(\Gamma \ell'_s)\right\}^2. \tag{2.49}$$

A lower limit for $\aleph_s$ can be obtained by substituting $\ell'_s \sim R/\Gamma$ in equation (2.49), which gives

$$\aleph_s \gtrsim \zeta_B(R)/\epsilon_0. \tag{2.50}$$

And a generous upper limit on the number of current sheets can be obtained by taking $\ell'_s \sim \ell'_a$ (the distance an electron travels in order to get accelerated to LF γ'_{max}). Using (2.27) we find $\aleph_s \lesssim 5 \times 10^8 \zeta_B(R)\Gamma_2^{-5} R_{15}^{-1} L_{48}^{3/2}$. This upper limit is much too large to be of practical use. The length of an acceleration region can be much larger than ℓ'_a when electron acceleration is balanced by radiative losses, and in that case far fewer number of PASs are needed to process magnetic energy to radiation. Let us take $\ell'_s = \eta \ell'_a$, with $\eta \sim 10^3$ that is needed to ensure that the observed radiation is dominated by electrons in PASs (as opposed to electrons in inter-PAS regions) and therefore the emergent spectrum is hard (see §2.2.3). Requiring the observed radiation be dominated by electrons in PASs yields

$$\aleph_s \sim 5 \times 10^2 \zeta_B(R) \eta_3^{-2} \Gamma_2^{-5} R_{15}^{-1} L_{48}^{3/2}. \tag{2.51}$$

2.3 Discussion

This work was motivated in part by a puzzle regarding gamma-ray bursts. A broad class of models for γ-ray emission from GRBs is based on the jet being baryonic, which moves with a Lorentz factor $\gtrsim 10^2$. The kinetic energy of baryons in the jet is converted to particle thermal energy via a series of shocks, and radiated away via the synchrotron process. According to this model, the spectrum below the peak should be $f_\nu \propto \nu^{-1/2}$ or softer whereas the observed spectra for most bursts are close to ν^0, i.e. much harder than the baryonic jet model predicts (*e.g.*, Ghisellini et al., 2000; Kumar & McMahon, 2008). The origin of this problem can be traced to the fact that particles are accelerated while crossing the shock front but otherwise they cool rapidly as they travel down-stream. Therefore, the number of electrons increases rapidly with decreasing LF ($dn'_e/d\gamma'_e \propto \gamma_e'^{-2}$ or faster) and that is the reason for the soft spectrum for a generic model that is based on dissipation of baryonic jet energy in shocks.

What we find is that if the GRB jet were not baryonic but Poynting, then the dissipation of magnetic fields and particle acceleration provides a way out this problem. The solution is due to the fact that particles can be kept in acceleration regions for a time much longer than the their radiative cooling time, thereby preventing the development of a large population of lower energy electrons that give rise to a soft spectrum. The spectrum of radiation from electrons in the region in between PASs (where electrons are undergoing cooling without acceleration) is soft like that it is for the shock model, but the spectrum emanating from PASs is hard because the powerlaw index for the particle distribution function in current sheets has $p \approx 1$. We have shown in §2.2.3 that the observed spectrum, which is a superposition of contributions from the two regions (PASs and inter-PASs), is hard when the average time electrons spend in acceleration region is much larger than their synchrotron cooling time.

One of the general results reported here could be used to determine whether a jet is baryonic or Poynting — for a Poynting jet, the spectrum below the peak softens with decreasing frequency which is opposite to the case of a baryonic jet where shocks convert jet energy to radiation.

Chapter 3

Swift J1644+57: an Ideal Test Bed of Radiation Mechanisms in a Relativistic Super-Eddington Jet

Chapter Preécis

The simultaneous radio, near-infrared, optical, X-ray, and γ-ray upper limits of the jetted tidal disruption event Sw J1644+57 provide a unique opportunity to test the emission mechanism and make-up of a relativistic super-Eddington jet. In this paper, we consider many different radiative mechanisms to model X-ray radiation observed in Sw J1644+57: synchrotron and internal inverse Compton from electrons and protons accelerated in shocks, external inverse Compton, photospheric, and a magnetic reconnection model. We are able to rule out the internal inverse Compton process as a potential producer of the X-rays in Sw J1644+57. A small parameter space exists for the electron synchrotron-in-shocks model, but the electrons are rapidly cooled which requires a very hard electron index. Protons accelerated through magnetic reconnection can explain the observed spectrum if the magnetization of the jet is very large but the radiative efficiency is less than 1% in this case. The external inverse Compton process has a similar problem as sychrotron-in-shocks with a hard electron index, but it easily matches the luminosity and peak energy

---

[†] This chapter will be submitted as Crumley P, Lu W, Hernández R, Santana R, Kumar P, 2015

of Sw J1644+57. Photospheric models need a significant ($\gtrsim$100) number of reheating events to occur just below the photosphere. Electrons accelerated by magnetic reconnection in a Poynting-dominated jet provides a natural explanation for the hard spectrum observed in Sw J1644+57 and can explain the X-ray emission of Sw J164+57.

3.1 Introduction

When a star wanders too close to the super-massive black hole (SMBH) at its galactic center, the star's self-gravity can no longer resist the tidal forces of the black hole. The star is torn apart in a tidal disruption event (TDE). Roughly half of its mass remains gravitationally bound to the black hole. This gas will return to pericenter and form an accretion disk (Lacy et al., 1982). The mass "falls back" onto this accretion disk at a super-Eddington accretion rate. The accretion rate decays in a characteristic manner, as $t^{-5/3}$ (Rees, 1988; Phinney, 1989). In some TDEs, a relativistic jet is launched, re-igniting a dormant quasar.

On March 28, 2011 the Swift Burst Alert Telescope (BAT) triggered on a relativistic TDE, Swift J164449.3+573451, hereafter Sw J1644+57. Sw J1644+57 was a new type of transient X-ray/soft γ-ray source. It was a luminous ($L_X \sim 10^{48}$ erg/s), highly variable ($\delta t \sim 100$ s), and long-lasting (around 500 days) transient source of X-rays and γ-rays (Burrows et al., 2011; Bloom et al., 2011). Detection of a coincident source in the optical, infrared, and radio wavelengths confirmed the X-rays were extra-galactic, and that Sw J1644+57 is located within the central 150 pc of its host galaxy (Levan et al., 2011; Zauderer et al., 2011). Archival images showed that this source was quiescent before the Swift trigger. Variable X-ray emission continued to be observed for ~ 500 days after the trigger, and the X-ray flux decreased in a manner consistent with $t^{-5/3}$. These X-rays are likely produced in a relativistic, $\Gamma \sim 10$, jet. After ~ 500 days, there was a steep drop in the X-ray flux. This drop off has been widely interpreted as the jet producing the prompt X-rays turning off. The very late time ($\gtrsim 500$ days) X-ray emission is produced by the same mildly relativistic, $\Gamma \gtrsim 2$, external forward shock that produces the early and late time radio emission (Zauderer et al., 2013). All of these lines of evidence point to Sw J1644+57 being the first relativistic jet from the tidal disruption of a stellar mass star by a super-massive black hole observed on the jet's axis.

The quality and breadth of Sw J1644+57's broadband data makes it an ideal astrophysical system to test different emission mechanisms. The long-lasting prompt emission allowed for a wealth of simultaneous data, with multiple instruments taking measurements in the radio, infrared, optical, X-rays, and soft γ-rays, as well as tight upper limits in the high-energy γ-rays. The radio and X-ray data of J1644+57 come from different sources; the radio data is well-modeled as the afterglow of the relativistic jet producing the X-rays (Metzger et al., 2012; Berger et al., 2012; Zauderer et al., 2013; Barniol Duran & Piran, 2013). The simplest model of the afterglow invokes energy injection to explain the radio light curve that is flat for ~ 100 days. However, the X-ray flux continues to decline as $t^{-5/3}$ while the radio flux is flat, belying the idea that energy is being continually injected into the system. To solve this issue, alternate models have been suggested. Kumar et al. (2013) suggested that the radio-producing electrons are inverse Compton cooled by the observed X-ray photons. The rate of cooling decreases as the X-ray luminosity decreases, producing a flat radio light curve. Mimica et al. (2015) suggested that the flat light curve is produced by a hypothetical two-jet structure in Sw J1644+57. When adding the contribution from afterglow of a faster ($\Gamma \sim 10$), narrower core jet and the afterglow of a slower ($\Gamma \sim 2$), wider, sheath jet, the observed radio light curve can be reproduced. Regardless of the details, the general picture is clear: the observed radio data is produced in the forward shock between the relativistic jet responsible for the X-ray emission and the external medium. The radio data of Sw J1644+57 is analogous to γ-ray burst afterglows, and as with γ-ray bursts, modeling the prompt emission of Sw J1644+57 is fraught with difficulty.

The production of the observed X-rays in Sw J1644+57 is not at all well understood. As mentioned previously, the temporal behavior of the X-rays is well explained by the rate at which the stellar gas falls back onto the accretion disk during a TDE. Any model of the prompt X-rays will face several challenges. For one, as we show in §3.3 and 3.5 the electrons are strongly cooled by both synchrotron and inverse Compton radiation. This cooling can easily cause excess flux at lower-energy bands. Additionally, the upper limits provided by the Fermi Large Area Telescope (100 MeV-10 GeV) and VERITAS at ∼500 GeV practically require that the high energy γ-rays be suppressed through $\gamma + \gamma$ pair production. This places strict upper limits on the radius of emission. A lower limit to the emission region is the Schwarzschild radius of the SMBH, $3 \times 10^{11} M_{\bullet,6}$cm. Since we know the total mass accreting onto the black hole is $\sim 1 M_{\odot}$, the production of the X-rays must be energy efficient; otherwise the total energy required exceeds the energy budget of the TDE. These challenges are really opportunities; they allow us to robustly rule out emission models in ways not possible in other astrophysical systems.

Previous works have modeled the emission of Sw J1644+57. Attempts were made to model X-ray emission with models commonly used in active galactic nuclei and γ-ray bursts: external inverse Compton and synchrotron from internal shocks (Liu et al., 2015; Wang & Cheng, 2012). These models are focused on the X-ray and soft γ-ray emission, and they ignore simultaneous measurements made in other wavelengths. Broadband fitting of the entire spectral energy distribution was done by Bloom et al. (2011), who used an external Compton model and fitted the spectrum at early times but not during the flaring period. Burrows et al. (2011) modeled the entire SED during periods of flaring, average and quiescent activity at early times. They concluded that the most probable explanation for the X-rays is a Poynting-dominated jet where the electrons are accelerated continuously in magnetic reconnection regions.

The goals of this paper are to critically assess the viability of as many model for non-thermal emission in relativistic jets as possible for Sw J1644+57. To this end we consider the following: first we limit ourselves to situations where the electrons are accelerated impulsively. By this, we mean any scenario where the electrons are quickly accelerated in a small region of the source. After being accelerated, the electrons then leave this region and cool either radiatively via synchrotron and inverse Compton radiation or adiabatically in a dynamical time. While shocks are typically invoked as a way to accelerate electrons impulsively, our arguments apply to any source where the electrons radiate most of their energy after they are finished being accelerated, and they are not re-accelerated after the initial acceleration, like electrons accelerated in relativistic shocks. In the context of impulsive acceleration we consider the electron synchrotron process (§3.3), the proton synchrotron process (§3.4),and internal inverse Compton radiation (§3.5). Internal inverse Compton radiation is where the electrons which up-scatter the seed photons are not necessarily the same population of electrons that produce the seed field, but the seed field is produced inside of the jet.[1] Besides these models, we also consider external inverse Compton scattering of optical and UV photons produced in an optically thick wind coming off the disk (§3.6), and photospheric radiation (§3.7), where a thermal spectrum is reprocessed by hot electrons in the jet. Finally, we apply the the magnetic-reconnection model developed in Kumar & Crumley (*in prep*) to Sw J1644+57 (§3.8).

3.2 Overview of Sw J1644+57 properties

Sw J1644+57 has several observations that must be matched by any successful model for the observed multi-wavelength radiation. In this section we briefly describe the broadband observations of Sw J1644+57.

The X-ray emission in XRT-BAT band can be fit as an absorbed, single power-law. During the first ten days the TDE experienced a period of intense X-ray flaring, with each individual flare lasting 10^3 seconds. After this time, the X-ray light curve shows a decline consistent with $t^{-5/3}$ lasting ∼500 days. After 500 days, the X-ray flux shows a precipitous drop. This steep drop off is interpreted to be the jet turning off and the X-rays being produced by the external forward shock (Zauderer et al., 2013).

During the early intense flaring, the Swift data shows an absorbed single power law in both the XRT and BAT band, with an average spectral index β of 0.8, $f_\nu \propto \nu^{-0.8}$, and an unabsorbed integrated flux from 1-10 keV

---

[1] Synchrotron self-Compton (SSC) is a particular example of the more general "interal" inverse-Compton process considered here.

of 6.5×10^{-10} erg s^{-1} (Burrows et al., 2011). This flux corresponds to a specific flux f_ν of 0.1 mJy at 1 keV and an isotropic luminosity of $L_X = 2.6 \times 10^{47}$erg s^{-1}. There is some uncertainty in the normalization and spectral index in the X-ray flux, but our findings are not particularly sensitive to the exact values given above. Wherever possible, we try to give analytic estimates of quantities. Therefore, so it is possible to see how our findings depend on our fiducial values for Sw J1644+57. The peak luminosity of Sw J1644+57 was about 3×10^{48} erg s^{-1} and the minimum in the first 10 days was $\sim 10^{46}$ erg s^{-1}. The total isotropic energy release in X-rays was 2×10^{53} erg. Considering a solar mass progenitor, the radiation mechanism must be $\gtrsim 1\%$ efficient; otherwise the energy requirements will exceed the energy budget.

Since Sw J1644+57 is likely located in the nucleus of its host galaxy, the optical extinction is large, $A_v \approx 4.5$ (Burrows et al., 2011). We therefore restrict ourselves to the K-band measurements where the extinction problem should be minimized. For an $A_v \approx 4.5$, we expect that the dereddened K-band values to be $\sim 60\%$ larger than the observed ones (Schlafly & Finkbeiner, 2011). The K-band data starts at about $f_\nu \sim 0.1$ mJy 2 days after trigger, decreases steadily by a factor of about 3 over the next ten days, and then is flat for 100 days (Burrows et al., 2011). The optical measurements also allow for the redshift to be measured, $z = 0.354$. This redshift corresponds to a luminosity distance, $d_L = 5.8 \times 10^{27}$ cm in a flat ΛCDM cosmology with $\Omega_\Lambda = 0.714$, $\Omega_M = 0.286$, and $H_0 = 69.6$.

In the hard γ-rays, the upper limit from Veritas at 500 GeV is that the flux must be less than 1.4×10^{-12} erg cm^{-2} s^{-1} (Aliu et al., 2011). Fermi LAT finds a similar upper limit on the flux from 100 MeV-10 GeV of 2.7×10^{-11} erg cm^{-2} s^{-1}, a factor of 24 times lower than the X-ray flux (Burrows et al., 2011).

The observed radio photons from Sw J1644+57 come from a different process than the X-ray photons. We therefore do not try to model the radio data in this paper. However, the radio data can be used to constrain some properties of the jet such as the initial bulk Lorentz factor which is $\sim 10-20$ (Metzger et al., 2012).

When modeling the X-ray emission, we do not require that the K-band flux be produced by the same mechanism that produces the X-rays; for instance, the K-band flux could be produced by the accretion disk. Instead we model the X-ray emission and then simply check to see if the K-band flux or γ-ray upper limits is significantly over produced for a particular parameter space in a particular model. If that is the case, then the model doesn't work for those parameters. If we have exhausted the entire possible parameter space without finding a solution consistent with the multi-wavelength data of Sw J1644+57, then we have ruled out that model.

3.3 Synchrotron Model of TDE Sw J1644+57

We first show with analytical calculations the difficulty the synchrotron model has reproducing the X-ray emission from Sw J1644+57. We then describe the numerical model we use to search the available parameter space to see if we can reproduce the observations. Our numerical model self-consistently calculates the inverse Compton and synchrotron emission from the non power-law electron distribution that may occur below the synchrotron self-absorption Lorentz factor (cf Ghisellini et al., 1988; de Kool & Begelman, 1989).

The synchrotron flux at a frequency ν from a spherically symmetric relativistic source depends on 6 free parameters: Γ, the bulk Lorentz factor; B', the co-moving magnetic field strength; N_e, the number of electrons radiating at ν; R, the radius of emission; γ_i, the typical electron Lorentz factor; and p, the electron spectral index.

The synchrotron frequency and peak flux are:

$$\nu_i = \frac{qB'\gamma_i^2\Gamma}{2\pi m_e c(1+z)} \approx (1.2 \times 10^{-8}\ \mathrm{eV})B'\gamma_i^2\Gamma(1+z)^{-1} \tag{3.1}$$

$$\begin{aligned} f_i &= \frac{\sqrt{3}q^3B'N_e\Gamma(1+z)}{4\pi d_L^2 m_e c^2} && (3.2) \\ &\approx (1.8 \times 10^2\ \mathrm{mJy})N_{e,55}B'\Gamma(1+z)/d_{L,28}^2 && (3.3) \end{aligned}$$

where d_L is the luminosity distance to the source. Throughout the paper frequencies ν are measured in eV, fluxes are measured in mJy, and the convention ($x_n \equiv x/(10^n\ \mathrm{cgs})$) is used.

The variability time is used to calculate the bulk Lorentz factor Γ. The conservative upper limit on the variability time, δt, of Sw J1644+57 is ~ 100 seconds (Burrows et al., 2011). Assuming a uniform jet, the variability time allows us to put a lower limit on the bulk Lorentz factor Γ because the variability time must be equal to or larger than the dynamical time, $\delta t \gtrsim t_{\mathrm{dyn}} = (1+z)R/(2c\Gamma^2)$. Additionally, there is good evidence that the X-ray source is at least mildly relativistic (Bloom et al., 2011; Levan et al., 2011). We therefore require that $\Gamma > 2$.

$$\Gamma = \max\left(4.1(1+z)^{1/2}\delta t_2^{-1/2}R_{14}^{1/2}, 2\right) \tag{3.4}$$

However, in this section we restrict ourselves to the regime where R is sufficiently large to ensure $4.1(1+z)^{1/2}\delta t_2^{-1/2}R_{14}^{1/2}$ is greater than 2 to simplify the expressions.

The optical depth of the source is

$$\tau_e = \frac{\sigma_T N_e}{4\pi R^2} \approx 53 N_{e,55} R_{14}^{-2} \tag{3.5}$$

We combine eq (3.1) and (3.2) to eliminate B'

$$f_i \approx \frac{1.5 \times 10^{10}\ \mathrm{mJy}}{\gamma_i^2} \left(\frac{\nu_i}{1\mathrm{eV}}\right) N_{e,55}(1+z)^2 d_{L,28}^{-2} \tag{3.6}$$

To eliminate $N_{e,55}$ from the above equation, we define a new quantity $\widetilde{Y}$,

$$\widetilde{Y} \equiv \gamma_i^2 \tau_e, \tag{3.7}$$

$\widetilde{Y}$ is closely related to Compton Y. Compton Y is the ratio of power an electron with a Lorentz factor γ radiates via synchrotron self-Compton process to the synchrotron process. In the Thomson regime $Y \equiv \frac{U'_\gamma}{U'_B}$, *i.e.*, the ratio of the energy density in the photons to the energy density of the magnetic field. $\widetilde{Y}$ is smaller than Y by a factor of order unity that depends on the electron index p. This small difference is due to the fact that there are electrons with Lorentz factors greater than γ_i. However, $\widetilde{Y}$ can be much greater than Compton Y when γ_i is sufficiently large enough to cause the inverse Compton scattering to be Klein-Nishina suppressed.

Rewriting eq (3.6)

$$f_i \approx \frac{3 \times 10^{8}\ \mathrm{mJy}}{\gamma_i^4} \left(\frac{\nu_i}{1\mathrm{eV}}\right) \widetilde{Y} R_{14}^2 (1+z)^2 d_{L,28}^{-2} \tag{3.8}$$

Solving for γ_i

$$\gamma_i \approx 740\ f_{i,\mathrm{mJy}}^{-1/4} \nu_{i,3}^{1/4} \widetilde{Y}^{1/4} R_{14}^{1/2} (1+z)^{1/2} d_{L,28}^{-1/2} \tag{3.9}$$

where $\nu_{i,3}$ is the frequency in keV.

Substituting (3.4) and (3.9) back into (3.1) we find the magnetic field is

$$B' \approx (3 \times 10^4\ \mathrm{G})\delta t_2^{1/2}\nu_{i,3}^{1/2} f_{i,\mathrm{mJy}}^{1/2}\widetilde{Y}^{-1/2}R_{14}^{-3/2}\frac{d_{L,28}}{\sqrt{1+z}} \tag{3.10}$$

While (3.2) and (3.10) gives the number of electrons:

$$N_{e,55} \approx 4 \times 10^{-8}\ \nu_{i,3}^{-1/2} f_{i,\mathrm{mJy}}^{1/2}\widetilde{Y}^{1/2}R_{14}(1+z)^{-1}d_{L,28} \tag{3.11}$$

The optical depth of these electrons is found by substituting eq (3.11) into eq. (3.5)

$$\tau_e \approx 1.4 \times 10^{-6}\ \nu_{i,3}^{-1/2} f_{i,\mathrm{mJy}}^{1/2}\widetilde{Y}^{1/2}R_{14}^{-1}(1+z)^{-1}d_{L,28} \tag{3.12}$$

If we assume the jet is baryonic, the optical depth of the jet would be

$$\tau_{\mathrm{jet}} \approx \frac{\sigma_T L_j(R/\Gamma)}{4\pi R^2 m_p c^3\Gamma^2} \approx 1.2 \times 10^{-3}\ \frac{L_{j,47}}{R_{14}\Gamma_1^3} \tag{3.13}$$

For TDE Sw J1644+57 the average flux at 1 keV during the first 10 days fluctuated between 2×10^{-3} and 1 mJy. The isotropic X-ray luminosity varied between 10^{46} and 3×10^{48} erg/s. The TDE occurred at redshift $z = 0.35$ corresponding to a distance $d_L = 5.8 \times 10^{27}$ cm.

If we take $L_{j,47} \sim 30$ and $f_{i,-3} \sim 1$ mJy there is a discrepancy between eq (3.12) and (3.13) of a factor $\sim 10^5$ when $\widetilde{Y} \lesssim 10$. Equation (3.12) implies $\tau_e \sim 6 \times 10^{-7}\widetilde{Y}^{1/2}$ whereas eq (3.13) implies $\tau_{\mathrm{jet}} \sim 4 \times 10^{-2}\Gamma_i^{-3}$. This discrepancy suggests only 1 in 10^5 electrons are radiating X-rays if $\Gamma \approx 10$. Making the two optical depths equal requires $\Gamma \sim 300$, too large for the Sw J1644+57. Alternatively, $\widetilde{Y}$ could be large, $\sim 4 \times 10^4$ with a more modest $\Gamma \sim 50$. While $\widetilde{Y} \sim 4 \times 10^4$ seems non-physically large, such a large $\widetilde{Y}$ value is not immediately dismissible because $\widetilde{Y}$ could be much larger than the true Compton Y due to the fact $\widetilde{Y}$ does not account for Klein-Nishina suppression.

Another way to account for the large difference between eq (3.13) and (3.12) could be that $\gamma_i \gg \gamma_c$, where γ_c is the cooling Lorentz factor. We will now show that for the majority of the available parameter space of Sw J1644+57, $\gamma_i \gg \gamma_c$.

Assuming that $Y \lesssim 1$ so that synchrotron cooling dominates, we find a cooling Lorentz factor of of

$$\gamma_c \approx \frac{6\pi m_e c}{\sigma_T B'^2 t'_{\rm dyn}} \quad \text{where} \quad t'_{\rm dyn} \sim \frac{R}{2c\Gamma} \tag{3.14}$$

Therefore,

$$\gamma_c \approx \frac{12\pi m_e c^2 \Gamma}{\sigma_T B'^2 R} \approx \frac{4.6 \times 10^5 \Gamma}{B'^2 R_{14}} \tag{3.15}$$

Using eq (3.10) for B' and (3.4) for Γ we find

$$\gamma_c \approx 2 \times 10^{-3}\ \nu_{i,-3}^{-1} f_{i,-3}^{-1} \widetilde{Y} R_{14}^{5/2} (1+z)^{3/2} \delta t_2^{-3/2} d_{L,28}^{-2} \tag{3.16}$$

Of course $\gamma_c < 1$ is not physical; what it means is that electrons are deep in the fast cooling regime, *i.e.* $\nu_c \ll$1 keV. Being in the fast cooling regime is a problem for Sw J1644+57 for two reasons. One, the observed spectrum $f_\nu \propto \nu^{-0.8}$ at 1 keV can be more naturally explained if electrons producing the X-ray photons are uncooled. If ν_c is much greater than a keV, the electron index p would be 2.6. If ν_c is less than a keV then p must be 1.6. A $p < 2$ is unlikely to occur from traditional shock acceleration (*e.g.*, Blandford & Eichler, 1987; Achterberg et al., 2001; Spitkovsky, 2008; Sironi & Spitkovsky, 2011b). The second problem is that if ν_c is much less than 1 keV, the solution runs the risk of causing the predicted K-band flux to be much larger than observed K-Band flux.

The average flux at 1 keV during the first ten days of Sw J1644+57 was $\sim$ 0.1 mJy, while the maximum dereddened K-band flux during the same time was ~ 0.15 mJy (Levan et al., 2011). Preventing the X-ray electrons from overproducing in the K-band requires either $\gamma_c \sim \gamma_i$, or for the self-absorption frequency, ν_a, to be larger than 0.57 eV (the energy of the K-band photons). It is clear from eq (3.16) that $\gamma_c \sim \gamma_i$ is very unlikely, except for extreme parameters for Sw J1644+57. Therefore only way to save the electrons from overproducing in the K-band is to have $\nu_a > 0.57$ eV. We now show it may be possible to avoid overproduction in the K-band through self-absorption by estimating the maximum possible ν_a.

The maximum possible ν_a will occur when $\nu_i \leq \nu_a$. The electrons that dominate the self-absorption have Lorentz factors γ_a

$$\gamma_a \equiv 9100 \nu_a^{1/2} B'^{-1/2} \Gamma^{-1/2} (1+z)^{1/2} \quad \text{if} \quad \gamma_{\min} < \gamma_a \tag{3.17}$$

The self-absorption frequency in the co-moving frame can be estimated by equating the synchrotron flux at ν_a, f_{ν_a} to the black-body flux at ν_a in the Rayleigh-Jeans limit.

$$\frac{2\pi \nu_a'^2}{c^2} m_e c^2 \gamma_a = \frac{f_{\nu_a}}{\Gamma} \frac{d_L^2}{(1+z)R^2} \tag{3.18}$$

Note that in eq (3.18) all quantities are in CGS units, but as before primes refers to the quantities measured in the co-moving rest frame. Assuming $f_{\nu_a} = f_i(\nu_a/\nu_i)^{-\beta}$ and converting all frequencies to eV measured in the observer frame we find

$$\nu_{a,\text{eV}}^{(5+2\beta)/2} = 3.3 \times 10^{-5+3\beta} f_{i,\text{mJy}} \nu_{i,3}^{\beta} B'^{1/2} \Gamma^{3/2} \frac{d_{L,28}^2 R_{14}^{-2}}{(1+z)^{-7/2}} \tag{3.19}$$

Substituting eq (3.10) into (3.19) we find

$$\nu_{a,\text{eV}}^{(5+2\beta)/2} = 1.1 \times 10^{-2+3\beta} f_{i,\text{mJy}}^{5/4} \nu_{i,3}^{(4\beta+1)/4} \frac{\Gamma d_{L,28}^{5/2} R_{14}^{-3}}{\widetilde{Y}^{1/4} (1+z)^{-7/2}} \tag{3.20}$$

When $\beta = 0.8$, $f_{i,\mathrm{mJy}} = 0.1$, $\nu_i = 1$ keV, $\Gamma \approx 10$, $z = 0.35$, and $d_{L,28} = 0.58$, the self-absorption frequency is $\nu_{a,\mathrm{eV}} \sim R_{14}^{-0.9}$. At $R \sim 3{\times}10^{13}$ cm, $\nu_a \sim 3$ eV. the self-absorption frequency is large enough to prevent the K-band constraint from being too large. Given the above self-absorption frequency, the flux at 0.57 eV is roughly equal to the observed value of 0.15 mJy,

$$\begin{aligned} f_{\mathrm{K-band}} &= f_{i,\mathrm{mJy}}(\nu_a/\nu_i)^{-0.8}(0.57/\nu_a)^{5/2} && (3.21) \\ &\approx 0.15 \text{ mJy} \quad \text{when} \quad \nu_a \sim 3, \nu_i = 1 \text{ keV}, f_i = 0.1 \text{ mJy}. && (3.22) \end{aligned}$$

So while $p < 2$ may make it seem somewhat unnatural for the electrons producing the X-ray photons to be cooled, $\nu_c < 1$ keV may not cause an overproduction of the K-band flux. Therefore we cannot automatically rule out the synchrotron model of Sw J1644+57; however the analytical calculations provided above argue that any solution would lie in an extreme part of the parameter space. To approach the problem, the self-absorption frequency must be determined very accurately, due to the sensitivity of the K-Band flux to the self-absorption frequency, as well as issues with calculating the synchrotron cooling below the self-absorption frequency. To this end we developed a new numerical code that uses 1-D radiative transfer to calculate the synchrotron and the synchrotron self-Compton spectrum with the main goal of self-consistently and accurately determining the self-absorption frequency and synchrotron flux in the K-band. Additionally, we will calculate the Inverse Compton flux at LAT and VERITAS energies. The goal of the code is to see if matching the observed synchrotron flux and spectrum at 1 keV causes too much flux in a different frequency band, in violation of observations and upper limits at these frequencies.

We use a methodology that calculates the observed inverse Compton flux and inverse Compton cooling accurately in both the Thomson and Klein-Nishina regime. It numerically integrates over the electron distribution to calculate the synchrotron and inverse Compton flux. The code is capable of calculating the spectrum from a non-power-law electron distribution and will iterate until the predicted emission is self-consistent with the cooling rate predicted from the spectrum produced. Our code works for an arbitrary electron index p, which is required because we expect the solution to have $p < 2$. Such a detailed treatment of the SSC model is necessary because non-power-law distributions can arise when the electrons are inverse Compton cooled but deep in the Klein-Nishina regime or when $\nu_c < \nu_a$. These cases are precisely the place where we've shown that any solution to the synchrotron model would likely exist. The new methodology is described in detail in the following section.

3.3.1 Detailed Synchrotron Model of TDE Sw J1644+57

Here we describe the methodology we use to search the possible parameter space that could reproduce the XRT-BAT X-ray emission from Sw J1644+57. In this section we limit ourselves to the scenario where the X-ray emission comes from the synchrotron part of an SSC spectrum. We consider the possibility that the X-ray photons are produced by the inverse Compton process in the following section.

The main goal of the methodology is simple: we give the code a set of free parameters, and it determines the electron distribution required to match the X-ray spectrum of Sw J1644+57 during the first 10 days after its discovery, $f_\nu = 0.1 \text{ mJy}(\nu/1 \text{ keV})^{-0.8}$ for 1 keV$\leq \nu \leq$150 keV. We then calculate the synchrotron and inverse Compton emission expected at different frequencies from the same electron distribution that is producing the X-ray photons. The code will then determine if the following conditions are met: the required luminosity in electrons, protons, and the magnetic field are all less than 10^{50} erg/s, and the predicted flux at at non-XRT frequencies are not much larger than the observations at these frequencies. We do not use the optical measurements because the extinction from the host galaxy is uncertain. The uncertain extinction makes it hard to predict an observed optical flux, so instead we use the near-IR observations where the extinction is greatly reduced. We calculate the predicted flux in the K-band (0.57 eV), the BAT band (125 keV), several frequencies in the LAT band (100 MeV, 1 GeV and 10 GeV), and at 500 GeV to compare to VERITAS upper limits, accounting for $\gamma + \gamma$ pair opacity for the ≥ 100 MeV photons. For frequencies at which a measurement of the flux was obtained, we require the predicted flux from the X-ray producing electrons not to exceed the observed measurement by more than a factor of 2. For frequencies where there are only upper limits on the flux, we require that the predicted flux not exceed these upper limits. We therefore are only trying to account for the X-ray emission while not violating any other observation of Sw J1644+57 or requiring a luminosity greater than 10^{50} erg/s, as then the energy requirements would exceed the restmass energy of the tidally disrupted star. For instance, if the predicted K-band flux is much less than the observed flux, that is acceptable because it simply means that the infrared emission from Sw J1644+57 comes from a different source than the X-rays, such as the accretion disk.

If the X-ray producing electrons do not violate any observational constraints and require less than 10^{50} erg/s of energy, then synchrotron radiation is a plausible mechanism for XRT-BAT emission of Sw J1644+57. We find that a small part of the parameter space survives at $R \lesssim 2 \times 10^{13}$ cm. See figure 3.2. Therefore, synchrotron radiation from a shock is able to produce the early X-ray spectrum observed by Swift. The allowed parameter space for such a solution is very small, and requires $p \approx 1.6$, which may be difficult to achieve for electrons accelerated in shocks.

3.3.1.1 Radiation Physics

Here we describe the new numerical methods used to self-consistently calculate the the SSC flux from an electron distribution with a co-moving number density $dn' = n'_e d\gamma$. Because we are worried about calculating the SSC spectrum for self-absorbed spectra, we must develop a new methodology because previous methods such as Nakar et al. (2009) do not work when a spectrum is harder than $f_\nu \propto \nu$. In this section, as before, primed quantities are in the co-moving rest frame, and unprimed quantities are in the observer rest frame. Unlike the previous section, all quantities in the section are in CGS units (including ν and f_ν).

3.3.1.2 Synchrotron Radiation

The synchrotron power radiated by a single electron with a Lorentz factor γ peaks at frequency in the co-moving rest frame $\nu'_p = qB'\gamma^2/(2\pi m_e c)$. $P_{\nu'}$, the angle-averaged power radiated at a given frequency ν' , depends on ratio $x \equiv \nu'/\nu'_p$ and the magnetic field B'.

$$P_{\nu'} \approx \frac{\sqrt{3}q^3 B'}{m_e c^2} F\left(\frac{\nu'}{\nu'_p}\right) \tag{3.23}$$

The exact formula for $F(x) \equiv F(\nu'/\nu'_p)$ in terms of integrals over modified Bessel functions can be found in Ginzburg & Syrovatskii (1965). However, to calculate the power radiated, we patch together their third-order approximation to $F(x)$ when $x \ll 1$ and first-order approximation of $F(x)$ when $x \gg 1$. The approximation agrees well with the exact solution to the synchrotron power, underestimating the power slightly at $x \approx 1$ and overestimating it slightly when $x \gg 1$. This approximation has the added benefit that it is integrable. We will integrate over this function later to calculate the total synchrotron power radiated by a single electron.

$$F(x) = \begin{cases} c_0 x^{1/3} g(x) & \text{for } x \leq 1 \\ \\ c_0 g(1) \sqrt{x} \exp{(1-x)} & \text{for } x > 1 \end{cases} \tag{3.24}$$

where

$$g(x) = 1 - \frac{\Gamma(\frac{1}{3})}{2}\left(\frac{x}{2}\right)^{2/3} + \frac{3}{4}\left(\frac{x}{2}\right)^{2} - \frac{9}{40}\frac{\Gamma(\frac{1}{3})}{\Gamma(\frac{5}{3})}\left(\frac{x}{2}\right)^{10/3} \tag{3.25}$$

$$c_0 = \frac{4\pi}{\sqrt{3}\Gamma(\frac{1}{3})} 2^{-1/3} \approx 2.15 \tag{3.26}$$

and $\Gamma(x)$ is the Gamma function.

The co-moving synchrotron specific intensity, I'_{ν}, is calculated using the formal solution to the 1-D radiative transfer equation of a constant synchrotron source with no incident radiation through an optical depth $\tau_{\nu'}$ ignoring scattering from Rybicki & Lightman (1986)

$$I_{\nu'} = (1 - e^{-\tau_{\nu'}})\frac{j_{\nu'}}{\alpha_{\nu'}} \tag{3.27}$$

The absorption coefficient, $\alpha_{\nu'}$, for electron distribution emitting a synchrotron power $P_{\nu'}$ is

$$\alpha_{\nu'} = -\frac{c^2}{8\pi\nu'}\int d\gamma \; \gamma^2 P_{\nu'} \frac{\partial}{\partial\gamma}\left[\frac{n'_e}{\gamma^2}\right]. \tag{3.28}$$

The emission coefficient, $j_{\nu'}$ is

$$j_{\nu'} = \frac{1}{4\pi}\int d\gamma n'_e P_{\nu'}. \tag{3.29}$$

We calculate the optical depth to synchrotron absorption by assuming the source has a thickness $R/2\Gamma$:

$$\tau_{\nu'} \approx \alpha_{\nu'} \frac{R}{2\Gamma}. \tag{3.30}$$

We also use the synchrotron optical depth to calculate the self-absorption frequency, ν'_a. ν'_a is found by numerically solving the equation $\tau_{\nu'_a} = 1$.

Assuming that the source is spherically symmetric and isotropic and moving at a bulk Lorentz factor $\Gamma \gg 1$, the observed synchrotron flux at frequency ν, $f_{\nu,\mathrm{syn}}$, is related to $I_{\nu'}$ by

$$f_{\nu,\mathrm{syn}} \approx 4\pi\Gamma(1+z) I_{\nu'} \left(\frac{R}{d_L}\right)^2 \tag{3.31}$$

Note that ignoring scattering effects in eq (3.27) means that the previous equation for the flux is only valid when the optical depth to Thomson scattering is small, *i.e.* $\sigma_T R \int d\gamma n'_e/(2\Gamma) \ll 1$

The total synchrotron energy radiated by an electron with Lorentz factor γ in the co-moving frame can be calculated by integrating over $P_{\nu'}$. However, any photons radiated at frequencies less the self-absorption frequency will be quickly absorbed by other electrons. These absorbed photons act as a heating source (Ghisellini et al., 1988). We approximate this synchrotron reheating by only allowing photons with frequencies $\geq \nu'_a$ to carry away energy from the electrons

$$P_{\mathrm{syn}}(\gamma) = \int_{\nu'_a}^{\infty} d\nu' P_{\nu'} \tag{3.32}$$

Defining a new quantity $x_a \equiv \nu'_a/\nu'_p$ and integrating over eq (3.23) for $P_{\nu'}$, we find the following expression for the synchrotron power emitted by an electron with Lorentz factor γ

$$P_{\text{syn}}(\gamma) \approx \frac{\sqrt{3}q^3B'}{m_ec^2}G\left(x_a\right). \tag{3.33}$$

$$G(x_a) = \begin{cases} c_0\left[h(1) - x_a^{4/3}h(x_a)\right] + c_1 & \text{for } x_a \leq 1 \\ \\ c_0g(1)\left[\sqrt{x_a}\exp\left(1 - x_a\right)\right. & \\ \qquad \left. + \frac{e}{2}\sqrt{\pi}\text{erfc}(\sqrt{x_a})\right] & \text{for } x_a > 1 \end{cases} \tag{3.34}$$

where erfc is the complementary error function,

$$h(x) = \frac{3}{2} - \frac{\Gamma(\frac{1}{3})}{2}\left(\frac{x}{2}\right)^{2/3} + \frac{9}{20}\left(\frac{x}{2}\right)^2 - \frac{27}{280}\frac{\Gamma(\frac{1}{3})}{\Gamma(\frac{5}{3})}\left(\frac{x}{2}\right)^{10/3} \tag{3.35}$$

and

$$c_1 = c_0g(1)\frac{\sqrt{\pi}}{2}\text{erfc}(1) \approx 0.822. \tag{3.36}$$

When $x_a \ll 1$ eq (3.33) agrees with the standard synchrotron power formula $\frac{4}{3}\sigma_t c\gamma^2B^2/(8\pi)$ within 1%.

3.3.1.3 Synchrotron Self Compton

We use eq (3.31) for $f_{\nu,\text{syn}}$ as the seed photons in the inverse Compton scattering to calculate the SSC flux. Therefore, we implicitly assume that a photon is only inverse Compton scattered once, a good assumption when either $Y \ll 1$ or the second scattering is Klein-Nishina suppressed. Our code can be easily extended to handle multiple scatterings self-consistently, but it becomes too numerically intensive to calculate multiple scatterings quickly.

We calculate the SSC flux using the equation for the inverse Compton spectrum produced by a single electron traveling through an isotropic field of photons given in Jones (1968); Blumenthal & Gould (1970). This equation differs from the exact Klein-Nishina cross section only by terms $\mathcal{O}(\gamma^{-2})$. This

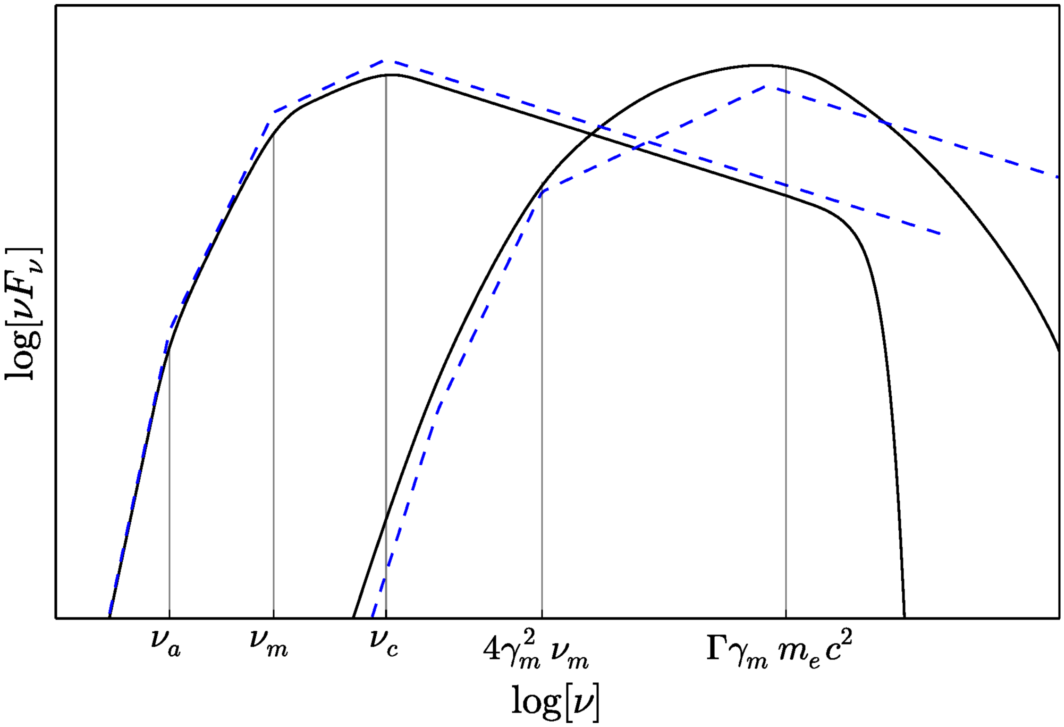

Figure 3.1: Example SSC spectra. The inverse Compton is exact to corrections of $\mathcal{O}(\gamma^{-2})$ to arbitrarily large ν. In Figure 3.2, the cooling is calculated self-consistently, but to make our spectrum easier to compare with previous results in this figure, the cooling is calculated assuming synchrotron cooling only. The curve that peaks at ν_i is the synchrotron component, and the curve that peaks at $\Gamma\gamma_i m_e c^2$ is the inverse Compton component. The dashed power-law synchrotron approximations are given in Sari et al. (1998), and inverse Compton dashed lines are calculated assuming the scattering takes place in the Thomson regime using power-law approximations from Sari & Esin (2001). The spectra agree well below the frequency $\Gamma\gamma_m m_e c^2$. Above this frequency, we should expect deviations due to Klein-Nishina effects. Above the Klein-Nishina frequency, the spectrum is similar to the spectrum found in Nakar et al. (2009); Wang et al. (2010).

equation is used to calculate the inverse Compton flux at arbitrarily large ν_{obs} as it accounts for the Klein-Nishina corrections to the Thomson cross-section. Using the observed synchrotron flux calculated with eq (3.31) to calculate the isotropic photon field and integrating over the co-moving electron density distribution yields the following equation for the SSC flux at ν_{obs}

$$f_{\nu_{\text{obs,IC}}} = \frac{3\nu_{\text{obs}}}{8\Gamma}\sigma_T R \int d\gamma \frac{n'_e}{\gamma^2} \int_{\nu_{\text{min}}}^{\nu_{\text{obs}}} d\nu \frac{f_{\nu,\text{syn}}}{\nu^2} g(\epsilon_\nu, q) \tag{3.37}$$

The function $g(\epsilon_\nu, q)$ is a function that accounts for the energy and angular dependence of the Klein-Nishina cross section. $g(\epsilon_\nu, q)$ depends on two dimensionless parameters: ϵ_ν, four times the photon's energy in the co-moving frame normalized by the electron energy, and q.

$$g(\epsilon_\nu, q) = 1 + q - 2q^2 + 2q\ln q + \frac{(\gamma^2\epsilon_\nu q)^2}{2 + 2\gamma^2\epsilon_\nu q}(1 - q) \tag{3.38}$$

$$\epsilon_\nu = \frac{4h\nu(1+z)}{\Gamma\gamma m_e c^2}; \qquad q = \frac{1}{\gamma^2\epsilon_\nu}\frac{\epsilon_{\nu_{\text{obs}}}}{(4 - \epsilon_{\nu_{\text{obs}}})} \tag{3.39}$$

The Thomson regime corresponds to $\epsilon_\nu \ll 1/\gamma^2$.

The lower limit of the $d\nu$ integral is found by numerically solving the following equation for ν_{min}:

$$\epsilon_{\nu_{\text{obs}}} = \frac{4\gamma^2\epsilon_{\nu_{\text{min}}}}{1 + \gamma^2\epsilon_{\nu_{\text{min}}}} \tag{3.40}$$

When ν_{obs} is well within the Thomson regime, *i.e.* $h\nu_{\text{obs}} \ll \Gamma\gamma m_e c^2/(1+z)$, the last term in eq (3.38) can be ignored, and the eq (3.40) can be linearized and solved for ν_{min}:

$$\nu_{\text{min}} \approx \frac{\nu_{\text{obs}}}{4\gamma^2} \quad \text{when} \quad \epsilon_{\nu_{\text{obs}}} \ll 1 \tag{3.41}$$

In the Thomson regime, ν_{min} is so small it is usually taken to be zero, but in the Klein-Nishina regime ν_{min} can actually become equal to or larger than

$\nu_{\rm obs}$. $\nu_{\rm min}$ will be larger than $\nu_{\rm obs}$ when $h\nu_{\rm obs} > \Gamma\gamma m_e c^2$, at which point the $d\nu$ integral is zero.

Our eq (3.37) simplifies to the expression often seen in in previous works concerned with SSC flux in the Thomson regime, such as Sari & Esin (2001) eq (A1), after taking $\nu_{\rm min} = 0$, making q first order in $\epsilon_{\nu_{\rm obs}}$, removing the last term from eq (3.38) for $g(\epsilon_\nu, q)$, and a simple variable substitution in the $d\nu$ integral. However, our eq (3.37) for $f_{\nu_{\rm obs,IC}}$ is accurate to arbitrarily large $\nu_{\rm obs}$ when using eq (3.40) to find $\nu_{\rm min}$ and the full form of $g(\epsilon_\nu, q)$. Since we made no assumptions on the function forms of n'_e, other than $\gamma \gg 1$, our formula may be used to calculate the SSC flux for any given electron distribution n'_e that is integrable and differentiable. A sample SSC spectrum is shown in Figure 3.1.

Since the inverse Compton flux will be calculated at large photon energies, $\gtrsim 100$ MeV, we must take into account the $\gamma + \gamma$ pair opacity. We use the methodology of Lithwick & Sari (2001a) to calculate an optical depth to pair production $\tau_{\gamma\gamma}$. If $\tau_{\gamma\gamma} \geq 1$ for a particular frequency, we assume those photons are absorbed by pair-production and set the observed flux at that frequency to zero.

$$\tau_{\gamma\gamma}(\nu_{\rm obs}) = \frac{11}{180}\frac{\sigma_T d_l^2}{\Gamma^2 Rhc(1+z)}\int_{\nu_{\gamma\gamma}}^{\infty} d\nu \frac{f_\nu}{\nu} \tag{3.42}$$

$$\nu_{\gamma\gamma} = \left(\frac{\Gamma m_e c^2}{h(1+z)}\right)^2 \frac{1}{\nu_{\rm obs}} \tag{3.43}$$

To calculate the total inverse Compton cooling, we integrate the inverse Compton spectrum of a single electron like we did for synchrotron radiation. This integral has been already calculated exactly for arbitrary seed photons and electron Lorentz factor γ by Jones (1965). We apply his solution to SSC cooling and $\gamma \gg 1$, (*i.e.* assuming $\beta \equiv \sqrt{1-\gamma^{-2}} \approx 1$)

$$P_{\rm IC}(\gamma) = \frac{12\sigma_T}{\left(\Gamma\gamma^2\right)^2}\left(\frac{d_L}{R}\right)^2 \int_0^\infty d\nu f_{\nu,\rm syn} F_{\rm IC}(\epsilon_\nu, \gamma) \tag{3.44}$$

$$\begin{aligned} F_{\rm IC}(\epsilon_\nu,\gamma) \;=\; & \left[f_1(\gamma^2\epsilon_\nu/2) - f_1(\epsilon_\nu/8)\right]/\epsilon_\nu^3 \\ & - \left[f_2(\gamma^2\epsilon_\nu/2) - f_2(\epsilon_\nu/8)\right]/(4\epsilon_\nu^2) \end{aligned} \tag{3.45}$$

$$\begin{aligned} f_1(x) \;=\; & (x+6+3/x)\ln(1+2x) \\ & -(22x^3/3+24x^2+18x+4)(1+2x)^{-2} \\ & -2+2{\rm Li}_2(-2x) \\ \approx\; & 8x^3/9 \quad \text{when } x \ll 1 \end{aligned} \tag{3.46}$$

$$\begin{aligned} f_2(x) \;=\; & \left[x+31/6+5/x+3/(2x^2)\right]\ln(1+2x) \\ & -(22x^3/3+28x^2+103x/3+17+3/x) \\ & \times(1+2x)^{-2} - 2 + {\rm Li}_2(-2x) \\ \approx\; & 4x^2/3 \quad \text{when } x \ll 1 \end{aligned} \tag{3.47}$$

The function Li_2 is called the dilogarithm, and it is defined as

$$\mathrm{Li}_2(x) = -\int_0^x \frac{\ln(1-x')}{x'}dx'. \tag{3.48}$$

This equation for $P_{\rm IC}$ is exact (ignoring multiple scatterings of a single photon) for all $\gamma \gg 1$, working both in the Thomson and Klein-Nishina regime. While it is a complicated formula, it can be evaluated in a straightforward manner numerically. Most scientific coding languages have a predefined function for Li_2, so calculating the inverse Compton power is only a single numerical integration over the seed spectrum.

The total SSC power in the co-moving rest frame is simply

$$P_{\rm TOT}(\gamma) = P_{\rm syn}(\gamma) + P_{\rm IC}(\gamma) \tag{3.49}$$

3.3.1.4 The electron distribution

We find the co-moving electron distribution by solving the continuity equation. Assume there is a source of electron $S(\gamma)$,

$$S(\gamma) = \begin{cases} 0 & \text{when } \gamma < \gamma_m \\ \dot{n}' \left(\gamma/\gamma_m\right)^{-p} & \text{when } \gamma \geq \gamma_m. \end{cases} \tag{3.50}$$

Then the electron distribution is found by solving

$$\frac{\partial n_e'}{\partial t} + \frac{\partial}{\partial \gamma}\left(\dot{\gamma} n_e'\right) = S(\gamma) \tag{3.51}$$

We solve this equation approximately by breaking it into two parts: one where the electrons are effectively uncooled and one where cooling is important, determined by comparing the following two timescales:

$$t'_{\mathrm{dyn}} = \frac{R}{2c\Gamma}, \qquad t'_{\mathrm{cool}} = \frac{m_e c^2 \gamma}{P_{\mathrm{TOT}}(\gamma)} \tag{3.52}$$

Defining a cooling electron Lorentz factor, γ_c, as the electron LF γ where $t'_{\mathrm{dyn}} = t'_{\mathrm{cool}}$, the solution of the continuity equation is:

$$n_e' = \begin{cases} t'_{\mathrm{dyn}} S(\gamma) & \text{when } \gamma \leq \gamma_c \\ \dfrac{m_e c^2}{P_{\mathrm{TOT}}(\gamma)} \displaystyle\int_{\gamma}^{\infty} d\gamma_e S(\gamma_e) & \text{when } \gamma > \gamma_c. \end{cases} \tag{3.53}$$

We desire an n_e' so that the synchrotron flux from n_e' matches the observed X-ray flux f_{ν_i} at ν_i with a spectral slope β, ($f_\nu \propto \nu^{-\beta}$). We choose the source of the electrons, $S(\gamma) = \dot{n}'(\gamma/\gamma_m)^{-p}$, to ensure the X-ray flux is matched as follows:

First we find the electron Lorentz factor whose synchrotron emission peaks at ν_i by inverting eq (3.1)

$$\gamma_i = 2.8 \times 10^5 \sqrt{\frac{\nu_{i,\mathrm{keV}}(1+z)}{B\Gamma}} \tag{3.54}$$

Then we match β by requiring the injected electron index p is

$$p = \begin{cases} 2\beta + 1 & \text{if } \gamma_i < \gamma_c \\ 2\beta + 2 - \left.\dfrac{d\log P_{\mathrm{TOT}}}{d\log\gamma}\right|_{\gamma=\gamma_i} & \text{if } \gamma_i \geq \gamma_c. \end{cases} \tag{3.55}$$

where P_{TOT} is given in eq (3.49). When the cooling is not dominated by Klein-Nishina cooling, $P_{\mathrm{TOT}} \propto \gamma^2$, and the standard cooling regime result $\beta = p/2$ is recovered.

Finally, we match the specific flux at ν_i by choosing a $\dot{n}'$ so that the synchrotron flux given in eq (3.31) is equal to f_i

Now we have described a complete set of equations that can be solved self-consistently for f_ν and n'_e after specifying the following free parameters, R, Γ, B', that will match an observed flux f_i and spectrum β. These equations will work for any set of free parameters, but since we have assumed $\Gamma,\ \gamma \gg 1$ in our derivation of the equations, we do not consider any electrons with $\gamma < 2$ and require $\Gamma \geq 2$. The radiative transfer equation eq (3.27) is no longer valid when the optical depth to Thomson scattering is greater than 1.

3.3.1.5 Energetics

Isotropic equivalent luminosity carried by a particular component of the jet is calculated using the co-moving energy density U'

$$\mathcal{L} = 4\pi U' R^2 c \Gamma^2 \tag{3.56}$$

The luminosity in the magnetic field is

$$\mathcal{L}_B = \frac{1}{2} B'^2 R^2 c \Gamma^2 \tag{3.57}$$

Solving eq (3.54) for B' we find

$$\mathcal{L}_B \approx 10^{60}\ \nu_{i,\mathrm{keV}}^2 \gamma_i^{-4} R_{14}^2 (1+z)^2 \text{ erg/s}. \tag{3.58}$$

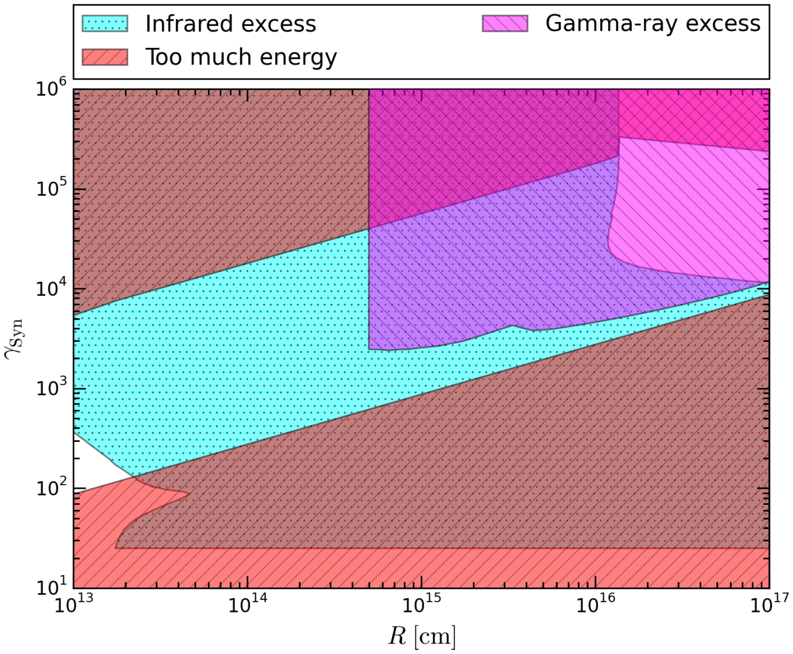

Figure 3.2: This figure shows the various constraints the observations of Sw J1644+57 impose on the synchrotron model. The y-axis is $\gamma_{\rm syn}$, the Lorentz factor of the electrons that radiate at 1 keV. The x-axis is the emission radius, R. Two regions on the plot require too much energy. In the lower region, the magnetic field required for $\gamma_{\rm syn}$ to radiate at 1 keV is too large. In the upper region, the electrons put a much larger fraction of their energy into inverse Compton radiation than synchrotron, *i.e.* Compton $Y \gtrsim 100$. LAT excess is where the XRT-BAT X-ray photons would be up-scattered into the LAT band and violate the strict upper limits measured in Sw J1644+57. Infrared excess is the region where cooled electrons will radiate in the K-band, overproducing the observed flux. Overlapping regions are where the synchrotron model will not work for several reasons. There are two regions where the synchrotron model is allowed, $R \sim 10^{17}$ cm and $R \lesssim 2 \times 10^{13}$ cm. The region at large R is can be ruled out because it requires a very large > 100 bulk Lorentz factor. At small radii, the synchrotron self-absorption break prevents the K-band flux from being too large, and this region of the parameter space, while small, is allowed for an electron index, $p \approx 1.6$.

Requiring the magnetic luminosity to not exceed 10^{50} erg/s places the following restriction on γ_i:

$$\gamma_i \geq 320\ \nu_{i,\mathrm{keV}}^{1/2} R_{14}^{1/2} (1+z)^{1/2}. \tag{3.59}$$

The luminosity required to power the electrons producing the X-ray radiation is

$$\mathcal{L}_e = 4\pi m_e c^3 R^2 \Gamma^2 t'_{\mathrm{dyn}} \int \gamma S(\gamma)\ d\gamma \tag{3.60}$$

$$\mathcal{L}_e \approx \Gamma^2 \gamma_i m_e c^2 N_e \times \max\left\{\frac{1}{t'_{\mathrm{dyn}}}, \frac{1}{t'_{\mathrm{cool}}}\right\}. \tag{3.61}$$

In the vast majority of the parameter space, the electrons are in the fast cooling regime, and the inverse Compton cooling is less important than the synchrotron cooling. When synchrotron cooling is the dominant cooling mechanism, the luminosity required is

$$\mathcal{L}_e \approx 5 \times 10^{48}\ f_{i,\mathrm{mJy}} \nu_{i,\mathrm{keV}} d_{L,28}^2 \ \mathrm{erg/s}, \tag{3.62}$$

when $t'_{\mathrm{dyn}}, t'_{c,\mathrm{IC}} \gg t'_{c,\mathrm{syn}}$, $\mathcal{L}_e \sim 3 \times 10^{47}$ erg/s if $f_i = 0.1$ mJy and $d_{L,28} = 0.58$. Therefore we arrive at the intuitive result that in the fast cooling regime, all of the energy given to the electrons by the shock will come out as radiation. If there are η_p cold protons per electron, the luminosity carried by the protons is

$$\mathcal{L}_p = 4\pi \eta_p m_p c^3 R^2 \Gamma^2 t'_{\mathrm{dyn}} \int S(\gamma)\ d\gamma \approx \eta_p \frac{m_p}{m_e} \gamma_i^{-1} \mathcal{L}_e. \tag{3.63}$$

When $t'_{\mathrm{dyn}}, t'_{c,\mathrm{IC}} \gg t'_{c,\mathrm{syn}}$, the luminosity carried by cold protons is

$$\mathcal{L}_p \approx 9 \times 10^{51}\ \eta_p \gamma_i^{-1} f_{i,\mathrm{mJy}} \nu_{i,\mathrm{keV}} d_{L,28}^2 \ \mathrm{erg/s}, \tag{3.64}$$

or $\sim 3\times 10^{50}\ \eta_p/\gamma_i$ erg/s for the fiducial parameters. From the earlier constraint on γ_i, eq (3.59), we see that the energy carried by the protons will not exceed 10^{50}erg unless η_p is greater than 100–1000.

3.4 Proton Synchrotron

In this section we consider proton synchrotron radiation. We find that proton synchrotron models are capable of reproducing the observed X-ray emission of Sw J1644+57 if the jet is Poynting dominated and the protons producing keV photons are in the fast cooling regime. The proton synchrotron model is not very efficient, with a radiative efficiency on the order of 1%. If the protons are not cooled through synchrotron radiation, then either the proton synchrotron process requires too much energy, or the protons will produce a tremendous amount of γ-rays through photo-pions. As we show in this section, for proton synchrotron to work the jet must be Poynting dominated, and the protons must be accelerated by magnetic reconnection.

As we have seen in the previous sections, preventing a K-band excess is difficult when modeling the observed X-rays of Sw J1644+57. If the X-rays are produced via synchrotron radiation, there are two ways to avoid an excess: either the synchrotron self-absorption frequency is above the optical band, or the cooling frequency, ν_c, is greater than ~ 0.1 keV. Protons are less radiatively efficient than electrons due to their larger mass. The radiative inefficiency of protons means that synchrotron self-absorption cannot prevent a K-band excess in proton synchrotron models. Following a similar argument as eq (3.18) and (3.19), the maximum synchrotron self-absorption frequency from protons radiating in a magnetic field B' is smaller than electrons self-absorption frequency by a factor $(m_p/m_e)^{3/(5+2\beta)}$. The ratio between the two self-absorption frequencies is a factor of ~ 30 if $\beta = 0.8$. We showed the difficulty in making ν_a large enough for electron synchrotron models §3.3.1, and the fact that ν_a is a factor of 30 smaller for proton synchrotron means that ν_a will not be large enough. Therefore, the proton synchrotron model only works if $\nu_i \sim 1$ keV and $\nu_c \gtrsim 0.1$ keV.

Protons with Lorentz factor γ_i in a magnetic field B', will radiate at a frequency

$$\nu_i = 6.3 \times 10^{-15} B' \Gamma \gamma_i^2 (1+z)^{-1} \text{ keV}. \tag{3.65}$$

If there are an isotropic equivalent number of protons, N_p, radiating at this frequency, the observed flux will be

$$f_{\nu_i} = 0.1 \text{ mJy } N_{p,55} B' \Gamma (1+z)/d_{L,28}^2 \tag{3.66}$$

Rewriting the above equations in terms of the luminosity carried by the magnetic field, $\mathcal{L}_B$, we find

$$\gamma_i \sim 8 \times 10^4 \ \nu_{i,\text{keV}}^{1/2} \mathcal{L}_{B,47}^{-1/4} R_{14}^{1/2} (1+z)^{1/2}, \tag{3.67}$$

and

$$N_p = 4 \times 10^{51} f_{\nu,\text{mJy}} \mathcal{L}_{B,47}^{-1/2} R_{14} d_{L,28}^2/(1+z) \tag{3.68}$$

The requirement that the proton cooling frequency be equal to or greater than 1 keV can be easily satisfied because the synchrotron cooling time for protons is larger than the cooling time for electrons by a factor $(m_p/m_e)^3$.

$$\begin{aligned} t'_{c,p}(\gamma_i) &= \frac{6\pi m_p^3 c}{m_e^2 \sigma_T B'^2 \gamma_i} & (3.69) \\ &= 9 \times 10^4 \ \nu_{i,\text{keV}}^{-1/2} \mathcal{L}_{B,47}^{-3/4} R_{14}^{3/2} \Gamma^2 (1+z)^{-1/2} \text{ s.} & (3.70) \end{aligned}$$

The proton synchrotron cooling frequency is

$$\nu_c = 3 \times 10^3 \ \mathcal{L}_{B,47}^{-3/2} R_{14} (1+z)^{-1} \text{ keV}. \tag{3.71}$$

We consider two regimes, one where the protons are slow cooling, $\nu_c > 150$ keV, and one where the protons are fast cooling $\nu_c \lesssim 1$ keV. First we consider the slow cooling regime.

In the slow cooling regime the energy carried by the protons is quite large. The proton luminosity is

$$\mathcal{L}_p = \frac{2\Gamma^3\gamma_i m_p c^3 N_p}{R} \tag{3.72}$$

$$\mathcal{L}_p \approx 3\times 10^{50}\ \Gamma^3\mathcal{L}_{B,47}^{-3/4} f_{\nu,\mathrm{mJy}}\nu_{i,\mathrm{keV}}^{1/2}\frac{R_{14}^{1/2}d_{L,28}^2}{(1+z)^{1/2}}\ \mathrm{erg/s} \tag{3.73}$$

For fiducial values $\mathcal{L}_p \approx 9\times 10^{48}\ \Gamma^3\mathcal{L}_{B,47}^{-3/4}R_{14}^{1/2}$ erg/s. If we assume the observed variability is due to the dynamical time of the jet, $\mathcal{L}_p \approx 9\times 10^{50}\ \mathcal{L}_{B,47}^{-3/4}R_{14}^2\delta t_2^{-3/2}$ erg/s. This luminosity is too large unless $\mathcal{L}_B$ is significantly larger than the observed X-ray luminosity or $R < 10^{14}$ cm. If $\mathcal{L}_B$ is much larger than the observed X-ray luminosity, there will be a cooling break in the BAT band. So the only option is to decrease R. As we now show, in proton synchrotron models R must be greater than 10^{14} cm, because when $R < 10^{14}$ cm, photo-pion emission will dominate. We calculate the photo-pion emission in a similar manner as Crumley & Kumar (2013a).

In the photo-pion process a photon interacts with a proton to cause a resonance that decays into pions. The resonance with the largest cross section is the Δ^+ resonance, $p^+ + \gamma \rightarrow \Delta^+$. The Δ^+ resonance quickly decays via the strong force into pions that further decay into photons, muons, electrons, and neutrinos. A proton with a Lorentz factor γ_i will undergo a photo-pion collision with a photon with an observed frequency $\nu_{p\gamma}$ if

$$\gamma_i\frac{h\nu_{p\gamma}(1+z)}{\Gamma} \geq 200\ \mathrm{MeV} \tag{3.74}$$

Using eq (3.67) for γ_i we find that the characteristic photon energy for the photo-pion process is

$$\nu_{p\gamma} = 2.5\ \mathrm{keV}\ \Gamma\nu_{i,\mathrm{keV}}^{-1/2}\mathcal{L}_{B,47}^{1/4}R_{14}^{-1/2}(1+z)^{-3/2}, \tag{3.75}$$

If $\nu_{p\gamma} \lesssim 10$ keV, we can approximate the number density of photons with frequencies $\gtrsim \nu'_{p\gamma}$ in the comoving frame is

$$n'_{p\gamma} \sim \frac{U'_X}{h\nu'_{p\gamma}} = \frac{L_X}{4\pi R^2 \Gamma^2 c h \nu'_{p\gamma}} \tag{3.76}$$

$$n'_{p\gamma} = 7 \times 10^{15} L_{X,47} \Gamma^{-2} R_{14}^{-3/2} \nu_{i,\mathrm{keV}}^{1/2} \mathcal{L}_{B,47}^{-1/4} (1+z)^{1/2} \ \mathrm{cm}^{-3} \tag{3.77}$$

The optical depth to photo-pion process is $\tau_{p\gamma} = n_{p\gamma}\sigma_{p\gamma} R/\Gamma$, where $\sigma_{p\gamma}$ is the cross section of delta resonance, $\sigma_{p\gamma} = 5 \times 10^{-28}$ cm^2.

$$\tau_{p\gamma} \sim 350 L_{X,47} R_{14}^{-5/2} \Gamma^{-3} \nu_{i,\mathrm{keV}}^{1/2} \mathcal{L}_{B,47}^{-1/4} (1+z)^{1/2} \tag{3.78}$$

Constraining Γ by the variability time we find

$$\tau_{p\gamma} = 5 \ L_{X,47} R_{14}^{-4} \nu_{i,\mathrm{keV}} \mathcal{L}_{B,47}^{-1/4} (1+z)^{-1} \delta t_2^{-3/2} \tag{3.79}$$

A proton will lose ~20% of its energy in a single photo-pion interaction. Since the optical depth to photo-pion scatterings is larger than 5 when $R \lesssim 10^{14}$ cm, nearly all of the luminosity carried by the protons will be put into photo-pions. The photons produced in the photo-pion interaction will be very high energy and not able to escape the jet due to $\gamma + \gamma$ pair opacity. However, the energy will cascade down until it is able to escape the jet releasing $\gtrsim 10^{49}$ erg/s worth of luminosity in the γ rays. A photo-pion bump is not seen, so the slow cooling regime can be ruled out.

We now consider the fast-cooling regime. From eq (3.71), it is clear that ν_c will less than 1 keV if $\mathcal{L}_B \gtrsim 10^{49}$ erg/s and $R \approx 10^{14}$ cm. When the protons are cooled by the synchrotron process, all their energy will come out in X-rays, so

$$\begin{aligned} \mathcal{L}_p &\approx \Gamma^2 \gamma_i m_p c^2 N_p / t'_{c,p}(\gamma_i) && (3.80) \\ &\approx 5 \times 10^{48} f_{\nu_i,\mathrm{mJy}} \nu_{i,\mathrm{keV}} d_{L,28}^2 \ \mathrm{erg/s} && (3.81) \\ &\sim 3 \times 10^{47} \ \mathrm{erg/s}. && (3.82) \end{aligned}$$

For the protons to be cooled, the jet must be strongly Poynting dominated. To calculate the magnetization parameter, σ, we assume that there are η_p cold protons for every proton that is accelerated to γ_i,

$$\sigma = \frac{\mathcal{L}_B}{\mathcal{L}_{p,\mathrm{cold}}} = \frac{\gamma_i}{\eta_p}\frac{\mathcal{L}_B}{\mathcal{L}_p} \tag{3.83}$$

$$\sigma = 5 \times 10^4 \, \mathcal{L}_{B,49}^{3/4} \eta_p^{-1} R_{14} f_{\nu_i,\mathrm{mJy}}^{-1} d_{L,28}^{-2} (1+z)^{3/2} \tag{3.84}$$

$\sigma \approx 2 \times 10^6 \eta_p^{-1} \mathcal{L}_{B,49}^{3/4} R_{14}$ for the fiducial values. Such a large value of sigma will prevent any strong shocks from forming, so shocks will not be able to accelerate the protons. However, magnetic reconnection is be able to accelerate the protons, as long as the energy given to the protons not exceed the initial energy in the magnetic field, or $\gamma_i \leq \sigma$. Using eq (3.67), when $\mathcal{L}_B = 10^{49}$ erg/s, $\gamma_i \approx 3 \times 10^4 R_{14}^{1/2}$ and $\sigma \approx 2 \times 10^6 \eta_p^{-1} R_{14}$. γ_i is less than σ as long as η_p is ≤ 100.

Therefore, the proton synchrotron process can match the X-ray spectrum of Sw J1644+57 if the jet is Poynting dominated with an efficiency $\sim 1\%$. The minimum Lorentz factors of the protons is $\gtrsim 2 \times 10^4$. The magnetization of the jet, σ must be larger than γ_i, or $\sigma \gtrsim 2 \times 10^4$. In the proton synchrotron model, the jet is very Poynting dominated.

3.5 Internal Inverse-Compton Radiation

In this section we consider the possibility that the X-ray emission observed during Sw J1644+57 is produced by Compton scattering lower energy photons that are internal to the jet itself. External inverse Compton is considered in the next section. We show that inverse Compton radiation is not capable of producing the observed averaged keV flux of Sw 1644+57 without causing an excess in a different wavelength or requiring too much energy.

In inverse Compton radiation, a seed photon of frequency ν_s and flux f_{ν_s} are scattered into the keV band by electrons with LF $\gamma_{\rm IC}$ and with Compton Y of $\widetilde{Y}_{\rm IC} = \gamma_{\rm IC}^2 \tau_{\rm IC}$, where $\tau_{\rm IC} = N_e \sigma_T / (4\pi R^2)$, and N_e is the number of electrons with LF greater than $\gamma_{\rm IC}$ that participate in the IC radiation. We can relate the seed photon field to the observed field by using

$$\nu_{\rm IC} \approx \gamma_{\rm IC}^2 \nu_s \approx 1 \text{ keV}; \qquad f_{\nu,{\rm IC}} \approx \tau_{\rm IC} f_{\nu_s} \approx 0.1 \text{ mJy} \tag{3.85}$$

In this section, we can constrain the parameter space allowed for inverse Compton radiation producing the observed X-rays. We try to make as few assumptions as possible about the seed photons. In the inverse Compton process, there are 6 free parameters: f_{ν_s}, ν_s, $\gamma_{\rm IC}$, Y, R, Γ. f_{ν_s} and ν_s are the seed photon flux and frequency in the observer frame. These are left completely free and are solved for by matching the observed flux of ~ 0.1 mJy at 1 keV. $\gamma_{\rm IC}$ is the Lorentz factor of electrons that scatter the seed field to 1 keV. $\widetilde{Y} = \gamma_{\rm IC}^2 \tau_{\rm IC}$ is a quantity closely related to Compton Y, and as before, R is the radius of emission and Γ is the bulk Lorentz factor.

We assume that the seed flux is produced through synchrotron radiation from electrons that may have a different Lorentz factor than $\gamma_{\rm IC}$. Additionally, we do not require that the electrons producing the seed field be part of the same power-law distribution as the electrons with Lorentz factors $\sim \gamma_{\rm IC}$. For the X-ray spectral index to match the observed value of -0.8, the seed flux spectrum above ν_s must be as soft or softer than observed spectrum of $\nu^{-0.8}$. Therefore, the self-absorption frequency must be less than or equal to ν_s. When ν_s is below the K-band, synchrotron self-absorption from the electrons producing the seed field cannot change the K-band flux predicted from the inverse Compton scattered photons. ν_s is below the K-band when $\gamma_{\rm IC} \gtrsim 25$. As we will now show, if $\gamma_{\rm IC} \gtrsim 25$, inverse Compton process cannot be responsible for the keV flux observed in Sw J1644+57.

When $\gamma_{\rm IC} \geq 25$, the electrons will cool rapidly by inverse Compton scattering X-ray photons. The cooled electrons will then overproduce in the K-band because they will scatter the seed field photons to energies $\sim$ 1eV.

The inverse Compton power from an electron with Lorentz factor γ traveling through a photon field with energy density U'_γ can be approximated by breaking the photon field into 2 parts: U'_s, the seed field that gets boosted from frequency ν_s to $\nu_{\rm IC} \sim 1$ keV, and the observed X-ray flux integrated over the XRT and BAT frequencies, f_{ν_x} using eq (3.44):

$$\begin{aligned} P_{\rm IC} &\approx P_{{\rm IC},s} + P_{{\rm IC},X} && (3.86) \\ P_{\rm IC} &= \frac{4}{3}\sigma_T c \gamma^2 U'_s + \frac{12\sigma_T d_L^2}{(\Gamma\gamma^2 R)^2}\int d\nu_x f_{\nu_x} F_{\rm IC}(\epsilon_{\nu_x}, \gamma), && (3.87) \end{aligned}$$

Ignoring Klein-Nishina effects and using $U'_s \approx U'_X/\widetilde{Y}$ where U'_X is the energy density in X-ray photons in the co-moving rest frame, the inverse Compton power is approximately,

$$P_{\rm IC} \approx \frac{4}{3}\sigma_T c \gamma^2 U_X \left(1 + \frac{1}{\widetilde{Y}}\right) \tag{3.88}$$

Re-writing the above equation in terms of the observed X-ray luminosity $U'_X = L_x/(4\pi c R^2 \Gamma^2)$ the cooling time becomes

$$t'_{c,{\rm IC}} \sim 120\ s \frac{R_{14}^2 \Gamma_1^2}{\gamma L_{X,47}} \left(1 + \frac{1}{\widetilde{Y}}\right)^{-1} \tag{3.89}$$

Comparing the inverse Compton cooling time to the dynamical time, $t'_{\rm dyn} = 170 R_{14} \Gamma_1^{-1}$, it is clear that even electrons with Lorentz factor order 2 will cool quickly via inverse Compton radiation at $R = 10^{14}$ cm. The cooling Lorentz factor is $\gamma_{c,\mathrm{IC}}$, and its corresponding inverse Compton frequency is

$$\gamma_{c,\mathrm{IC}} \approx 7\frac{R_{15}\Gamma_1^3}{L_{X,47}}\left(1+\frac{1}{\widetilde{Y}}\right)^{-1} \quad ; \quad \nu_{c,\mathrm{IC}} = \nu_{\mathrm{IC}}\left(\frac{\gamma_{c,\mathrm{IC}}^2}{\gamma_{\mathrm{IC}}^2}\right) \tag{3.90}$$

The inverse Compton flux between $\nu_{c,\mathrm{IC}}$ and ν_{IC} is proportional to $\nu^{-1/2}$, and the inverse Compton flux below $\nu_{c,\mathrm{IC}}$ is proportional to ν^1. When $\gamma_{c,\mathrm{IC}} < \gamma_{\mathrm{IC}}$, the extrapolated K-band flux will be

$$\begin{aligned} f_{\mathrm{K-band}} &\approx f_{\nu,\mathrm{IC}}\left(\frac{\nu_{c,\mathrm{IC}}}{\nu_{\mathrm{IC}}}\right)^{-1/2}\left(\frac{\nu_{\mathrm{K-band}}}{\nu_{c,\mathrm{IC}}}\right) && (3.91)\\ &\approx 5.7\times10^{-4} f_{\nu,\mathrm{IC}}\frac{\gamma_{\mathrm{IC}}^3}{\gamma_{c,\mathrm{IC}}^3} && (3.92)\end{aligned}$$

The measured flux in the K-band at early times was 0.15 mJy, and the measured flux at 1 keV was ~ 0.1 mJy. We find that $\gamma_{\mathrm{IC}} \leq 17\gamma_{c,\mathrm{IC}}$; otherwise the K-band flux will be too large. Therefore

$$\gamma_{\mathrm{IC}} \leq \max\left[25,\ 12\ \frac{R_{14}\Gamma_1^3}{L_{X,47}}\left(1+\frac{1}{\widetilde{Y}}\right)^{-1}\right] \tag{3.93}$$

However, when $12\ R_{14}\Gamma_1^3 L_{X,47}^{-1} \gtrsim 25$, the inverse Compton process will not work due to overproduction in the LAT band. The optical depth at 100 MeV can be approximated using the total X ray luminosity and eq (3.42) and (3.43). The photons with obs energy 100 MeV will pair produce with photon with energy

$$\nu_{\gamma\gamma} \sim\ 2\Gamma^2(1+z)^{-2}\nu_{obs,100\ \mathrm{MeV}}^{-1}\ \mathrm{keV} \tag{3.94}$$

With $\Gamma \sim 10$ pair production will occur with photons with energies in the BAT band. Since the observed spectral index is ~ 1 to 150 keV, we can estimate the number of photons at $\nu_{\gamma\gamma}$ as

$$\begin{aligned} n'_{\gamma\gamma} &\sim \frac{L_X}{4\pi R^2 c\Gamma^2 h\nu'_{\gamma\gamma}} && (3.95)\\ n'_{\gamma\gamma} &\sim 8\times10^{15}\ L_{X,47}R_{14}^{-2}\Gamma^{-3}(1+z)\ \mathrm{cm}^{-3} && (3.96)\end{aligned}$$

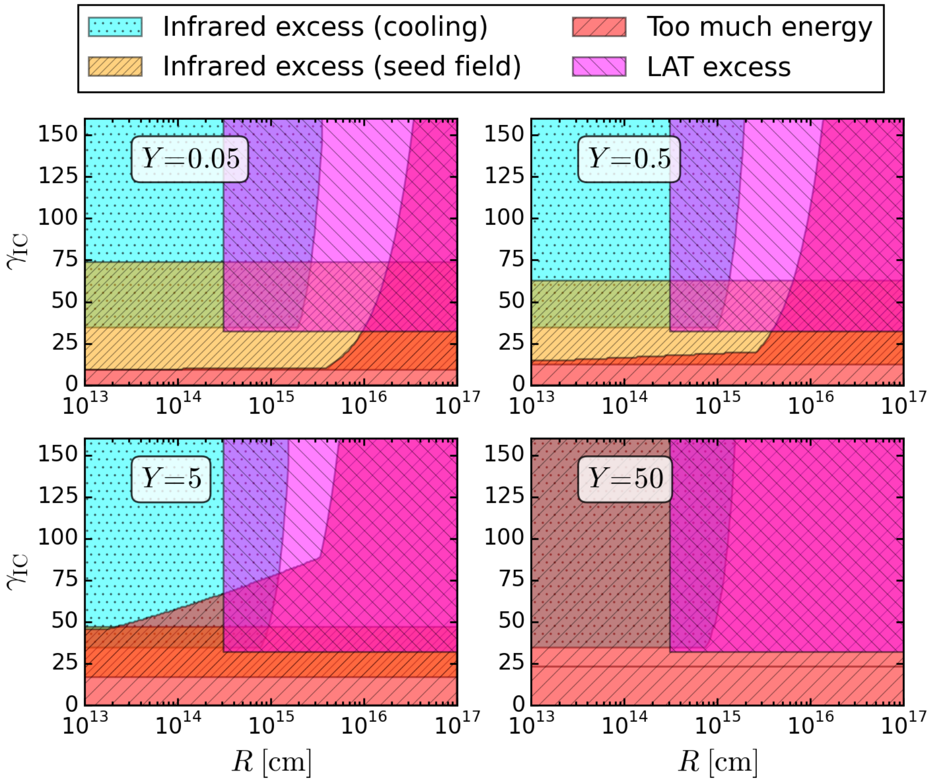

Figure 3.3: This figure shows the various constraints the observations of Sw J1644+57 impose on any internal inverse Compton model (see §3.5 for details). The y-axis is $\gamma_{\rm IC}$, the electrons that scatter a seed photon field to 1 keV. The x-axis is R, the radius of emission. The different panels show different values of Compton Y. Infrared excess (cooling) is the area where cooled electrons will IC scatter the seed field into the infrared and overproduced the observed K-Band flux. Infrared excess (seed field) is the area where the required flux in the seed field that is up-scattered to 1 keV exceeds the observed K-band measurements. LAT excess is where photons of $\sim$ 150 keV would be up-scattered into the LAT band and violate the strict upper limits measured in Sw J1644+57. Too much energy where the energy required is greater than the rest mass of a solar mass star (a luminosity $\gtrsim 10^{50}$erg/s). Overlapping regions are where the internal IC model will not work for several reasons. Since there is no white space in this figure, the internal IC model is ruled out.

Which has a corresponding optical depth of

$$\tau_{\gamma\gamma} = n'_{\gamma\gamma}\sigma_T R/\Gamma \sim 2L_{X,47}R_{14}^{-1}\Gamma_1^{-4} \tag{3.97}$$

If the electrons are uncooled, $12R_{14}\Gamma_1^3 L_{X,47}^{-1} \gtrsim 25$ implies that the optical depth to pair production for photons of energies ~ 100 MeV must be less than

$$\tau_{\gamma\gamma} \lesssim \Gamma_1^{-1} \tag{3.98}$$

The optical depth of pair production to 100 MeV photons is less than one, because Γ_1 is greater than 1 when $R_{14}\Gamma_1^3 \gtrsim 20$ and $t_{\rm dyn} < 100$ seconds. Therefore photons with energies $\gtrsim 100$ MeV will escape the jet. The emission would over produce the stringent upper limits from the LAT unless $\widetilde{Y} \lesssim\, = 4\times 10^{-2}$ (*i.e.*, the ratio of the X-ray luminosity in the XRT band to the upper limits from *Fermi*-LAT). However such a low Compton Y can be disregarded due to the large luminosity required in the seed field of photons. Therefore it is a strict requirement that

$$\gamma_{\rm IC} \lesssim 25 \tag{3.99}$$

When $\gamma_{\rm IC} \lesssim 25$, the seed frequency, ν_s is greater than K-band frequency. In synchrotron spectra, the hardest spectral index achievable is $f_\nu \propto \nu^{5/2}$. Using eq (3.85), the minimum flux at 0.57 eV can be calculated using the observed flux at 1 keV, $f_{\nu,\rm IC}$

$$f_{\rm K-band} \approx \frac{f_{\nu,\rm IC}}{\tau_{\rm IC}}\left(\frac{0.57\ \rm eV}{\nu_{\rm IC}/\gamma_{\rm IC}^2}\right)^{5/2} \tag{3.100}$$

$$f_{\rm K-band} \sim 8\times 10^{-8}\gamma_{\rm IC}^7 \widetilde{Y}^{-1} f_{\nu,\rm IC}\nu_{\rm IC,keV}^{-5/2} \tag{3.101}$$

Requiring $f_{\rm K-band} \lesssim 2f_{\nu,\rm IC}$ to avoid an infrared excess, we come to the tight constraint on $\gamma_{\rm IC}$,

$$\gamma_{\rm IC} \lesssim 11\ \widetilde{Y}^{1/7} \tag{3.102}$$

The total number of electrons required in the jet is

$$N_{e,\mathrm{tot}} = \frac{4\pi R^2 \widetilde{Y}}{\sigma_T \gamma_{\mathrm{IC}}^2} \max\left(1, \frac{t'_{\mathrm{dyn}}}{t'_{c,\mathrm{IC}}}\right) \tag{3.103}$$

As we showed earlier, it is likely to be the case that the electrons are cooled. Using eq (3.89) for the inverse Compton cooling time we find that the total number of electrons in the jet must be greater than

$$N_{e,\mathrm{tot}} \gtrsim 1.5 \times 10^{53} \frac{L_{X,47} t'_{\mathrm{dyn}}}{\Gamma^2 \gamma_{\mathrm{IC}}} \left(\widetilde{Y} + 1\right). \tag{3.104}$$

Assuming η_p cold protons per hot electron in the jet, the luminosity carried by the protons in the jet is

$$\mathcal{L}_p \approx \eta_p \Gamma^2 m_p c^2 N_{e,\mathrm{tot}} / t'_{\mathrm{dyn}}. \tag{3.105}$$

Using eq (3.104) for $N_{e,\mathrm{tot}}$ relation of

$$\mathcal{L}_p \gtrsim 2.3 \times 10^{50} \; \eta_p \frac{L_{X,47}}{\gamma_{\mathrm{IC}}} \left(\widetilde{Y} + 1\right) \; \mathrm{erg/s}. \tag{3.106}$$

Using the inequality for γ_{IC} in eq (3.102)

$$\mathcal{L}_p \gtrsim 2 \times 10^{49} \; \eta_p L_{X,47} \left(\widetilde{Y}^{6/7} + \widetilde{Y}^{-1/7}\right) \tag{3.107}$$

The mean luminosity of Sw J1644+67 for the first 10 days is $\approx 3 \times 10^{47}$ erg/s. Using this luminosity we find $\mathcal{L}_p \gtrsim 9 \times 10^{49}$ erg/s for the first 10^6 seconds of Sw 1644+57. This energy requirement is prohibitive even if $\eta_p \sim 1$. Therefore, the internal inverse Compton radiative mechanism can be ruled out for Sw J1644+57. The constraints outlined in this section are shown graphically in figure 3.3.

3.6 External Inverse-Compton Radiation

Due to the super-Eddington accretion, the jet is likely surrounded by a strong external radiation field (ERF) of near Eddington luminosity. For example, the ERF could come from the super-Eddington wind launched from the accretion disk (Strubbe & Quataert, 2009; Ohsuga & Mineshige, 2011). Since the wind is very optically thick, photons are advected by electron scattering and cool adiabatically to ~ 10 eV before escaping. In this section, we consider the possibility that the X-rays may come from an external inverse-Compton (EIC) process up-scattering soft photons from the super-Eddington wind.

This EIC process will boost soft photons' energy by a factor of $\Gamma^2\gamma_e^2$. Typically, if $\Gamma = 10$ and $\gamma_e = 1$ (cold electrons), the scattered photons will have energy ~ 1 keV. Therefore, EIC emission is a plausible way to produce the observed X-rays in Swift J1644+57. We describe general considerations of an EIC model for Sw J1644+57 in this section. First we describe the characteristics of the jet and the radiation from the wind. Then we calculate the expected EIC luminosity and spectrum in the XRT-BAT band. We find that the EIC model is marginally consistent with the observations if the efficiency in launching the wind is large, and the Lorentz factor of the jet is not too large, $\Gamma \lesssim 5$.

3.6.1 Jet Characteristics

We assume a baryonic (pure-Hydrogen) jet with half opening angle $\theta_j \ll 1$. Electrons' number density is denoted as n_e (BH rest frame) and n'_e (in the jet comoving frame). We denote the optical depth of the jet for an external photon penetrating in the transverse and radial direction as t_{trvs} and

t_r. We have

$$\tau_{trvs} = \frac{\pi\theta_j^2 R^2 \Delta R n_e \sigma_T}{2\pi R\theta_j \Delta R} = \frac{1}{2} R\theta_j n_e \sigma_T \simeq 0.59 \frac{L_{j,48}\theta_{j,-1}}{R_{13}\Gamma_1} \tag{3.108}$$

and

$$\tau_r = R n_e \sigma_T = 11.7 \frac{L_{j,48}}{R_{13}\Gamma_1} \tag{3.109}$$

We can see that it's easier for external photons to penetrate the jet in the transverse direction. Defining the "self-shielding radius" where $\tau_{trvs} = 1$, we have

$$R_{j,self} = 5.9 \times 10^{12} \frac{L_{j,48}\theta_{j,-1}}{\Gamma_1} \text{ cm} \tag{3.110}$$

Note that the optical depth for an internal photon, defined by eq(3.13), is much smaller than τ_{trvs} (by a factor of $2/\Gamma^2\theta_j$), so we can ignore multiple EIC scatterings at radii $R > R_{j,self}$.

3.6.2 Radiation from the Wind

The fallback gas initially in elliptical orbits shocks on itself, circularizes near pericenter and settles in a disk. The shocks (and also the friction in the disk) convert orbital kinetic energy to thermal energy. Due the high density (when the fallback is super-Eddington), thermal energy is quickly converted to radiation energy mostly by free-free emission. However, radiation is trapped by electron scattering and hence the shocked gas is radiation pressure dominated. While the gas accretes inward and releases gravitational energy, some fraction of the mass is likely unbound and leaves the accretion disk in a wind. The wind launching process still has large theoretical uncertainties (Ohsuga & Mineshige, 2011; Narayan et al., 2012b; Jiang et al., 2014). Below, we construct a simple 1-D model of the radiation characteristics from the wind.

Generally, we use upper case R to denote the true radius (in cm) and the lower case r for the dimensionless radius R/R_S (normalized by the Schwarzschild radius $R_S = 3 \times 10^{11} m_6$ cm). Also, the true accretion, outflowing (sub "w"), and fallback (sub "fb") rates (in $M_\odot\ yr^{-1}$) are denoted as upper case $\dot{M}$ and the dimensionless rates are normalized by the Eddington accretion rate as $\dot{m} = \dot{M}/\dot{M}_{Edd}$. The Eddington accretion rate is defined as $\dot{M}_{Edd} = 10 L_{Edd}/c^2$, and $L_{Edd} = 1.5 \times 10^{44} m_6$ erg s^{-1}, where m_6 is BH mass in $10^6 M_\odot$.

For a star with mass $M_* = m_* M_\odot$ and radius $R_* = r_* R_\odot$, the (dimensionless) tidal disruption radius is

$$r_T = \frac{R_*}{R_S}\left(\frac{M_{BH}}{M_*}\right)^{1/3} \simeq 23.3\ m_6^{-2/3} m_*^{-1/3} r_* \tag{3.111}$$

The star's original orbit has pericenter distance $r_p < r_T$. We assume that the wind is launched at close to the escape velocity at radius $r_o \simeq 2r_p$ (i.e. circularization radius), where the radiation energy and kinetic energy are in equipartition:

$$aT_o^4 \simeq \frac{1}{2}\rho_w v_w^2 \tag{3.112}$$

where a is the radiation constant, T_o is the temperature at r_o, ρ_w is wind density, and $v_w \simeq v_{esc}(r_o) \simeq r_o^{-1/2} c$ is the outflowing velocity. Following Strubbe & Quataert (2009), we assume a fraction f_{out} of the fall-back gas is leaves in the wind (assuming spherical geometry), so we have

$$4\pi r_o^2 \rho_w(r_o) v_w = \dot{M}_w = f_{out} \dot{M}_{fb} \tag{3.113}$$

where $\dot{M}_{fb}$ is the mass fall-back rate.

For a thick disk, we expect the viscous time to be much shorter than the fallback time, so the BH accretion rate is $\dot{M} \simeq (1 - f_{out})\dot{M}_{fb}$ (ignoring the mass carried away by the jet). If a fraction f_j of the accretion power $\dot{M}c^2$ is used to power the jet, we have

$$L_j(1-cos\theta_j) \simeq f_j(1-f_{out})\dot{M}_{fb}c^2 \simeq \frac{f_j(1-f_{out})}{f_{out}}\dot{M}_w c^2 \tag{3.114}$$

where L_j is the isotropic jet power, and θ_j is the half opening angle. For example, a set of values $\{f_j = f_{out} = 0.5,\ \theta_j = 0.1\}$ yields $\dot{m}_w = 6.7L_{j,48}m_6^{-1}$. Since the BH's rotation energy may play some role in launching the jet (Blandford & Znajek, 1977; Tchekhovskoy et al., 2011), $f_j > 1$ may be allowed and we leave the jet power L_j as a free parameter.

From eq (3.112) and (3.113), we can get the radiation temperature at the wind launching site

$$T_o \simeq 1.3\times 10^6 r_o^{-5/8} m_6^{-1/4} \dot{m}_w^{1/4}\ \mathrm{K} \tag{3.115}$$

The opacity is dominated by electron scattering (Badnell et al., 2005; Shen et al., 2015), so the optical depth of the $> R$ region is

$$\tau_w = \rho_w \kappa_s R \simeq 4.7\dot{m}_{w,1} r_{o,1}^{1/2} R_{13}^{-1} \tag{3.116}$$

where $\kappa_s = 0.2(1+X)\ \mathrm{cm}^2\ \mathrm{g}^{-1}$ is the opacity from Thomson scattering. We choose a Hydrogen mass fraction of $X = 0.7$, but the results are not sensitive to our choice in X. The wind becomes transparent ($\tau_w = 1$) at radius

$$r_{w,tr} \simeq 1.6\times 10^2 \dot{m}_{w,1} r_{o,1}^{1/2} \tag{3.117}$$

Below $r_{w,tr}$, photons escape by diffusion. The radius where diffusion time equals to the dynamical time (*i.e.*, $\tau_w = c/v_w$) is called the “advection radius”, $r_{w,adv}$

$$r_{w,adv} \simeq 50\dot{m}_{w,1} \tag{3.118}$$

Note that the advection radius is independent of the wind speed. Below $r_{w,adv}$, photons are advected by the wind, so the photon temperature is controlled by adiabatic expansion. Since radiation pressure dominates, we have $P = aT^4/3 \propto \rho^{4/3} \propto r^{-8/3}$, and we get

$$T(r) = T_o(r/r_o)^{-2/3} \tag{3.119}$$

Putting eq (3.115) and (3.118) into (3.119), we get the radiation temperature at the advection radius

$$T_{adv} \equiv T(R_{w,adv}) = 1.9 \times 10^5 r_{o,1}^{1/24} m_6^{-1/4} \dot{m}_{w,1}^{-5/12} \text{ K} \tag{3.120}$$

Above $r_{w,adv}$, photons are no longer advected by wind electrons, and the changing of color by Comptonization can be ignored. Therefore, the bolometric luminosity of the wind is

$$L_{w,bol} \simeq \frac{4\pi R_{w,adv}^2 a T_{adv}^4 v_w}{3} \tag{3.121}$$

$$L_{w,bol} \simeq 8.8 \times 10^{43} r_{o,1}^{-1/3} m_6 \dot{m}_{w,1}^{1/3} \text{ erg s}^{-1} \tag{3.122}$$

We can see the following: the wind luminosity can mildly exceed the Eddington luminosity (when $\dot{m}_w \gg 1$); the wind is generally brighter than the other non-jet components, *e.g.*, the disk and unbound debris (Strubbe & Quataert, 2009; Kasen & Ramirez-Ruiz, 2010).

Many TDE candidates have very bright UV luminosities, which could come from the wind. For instance, PS1-10jh (Gezari et al., 2012) has peak (22 d) luminosity $L \simeq 10^{45} erg/s$ at $T_{BB} \sim 3 \times 10^4 K$ (T_{BB} has large uncertainties). By solving Eq.(3.120) and (3.121), we find $\dot{m}_w = 4.0 \times 10^2 r_{o,1}^{-1/8}$ and $m_6 = 3.3 r_{o,1}^{3/8}$.These values are roughly consistent with the accretion rate and BH mass expected from a TDE.

3.6.3 External Inverse-Compton Luminosity

In this subsection, the EIC luminosities from the regions above and below the wind photosphere ($R_{w,tr}$) are calculated, $L_{IC}^{(1)}$ and $L_{IC}^{(2)}$ respectively. For simplicity, we assume electrons have a single Lorentz factor γ_e in the jet comoving frame. A powerlaw distribution is considered in next subsection, §3.6.4. We show that the EIC process above (below) the photosphere can boost the wind luminosity in Eq.(3.121) by a factor of $\sim \Gamma^2\gamma_e^2\tau_{j,r}$ $(2\Gamma^2\gamma_e^2/\theta_j)$. Therefore the observed X-ray luminosity ($3 \times 10^{47} - -3 \times 10^{48}$ erg/s) can be easily reached by boosting a wind luminosity ($10^{44} - 10^{45}$ erg/s) by a factor of $10^2 - 10^3$.

3.6.3.1 EIC above the photosphere

Right above photosphere, $R_{w,tr}$, the ERF is nearly isotropic. Photons that diffuse out of the photosphere may get scattered back (since $\tau_w = 1$), isotropizing the ERF. As we go farther and farther from the photosphere, the flux from the photosphere decreases as R^{-2} (inverse square law) and the back-scattered flux decreases as R^{-3} (since $\tau_w \propto R^{-1}$). Since the photosphere flux is pointing parallel to the jet moving direction, the EIC emission comes mostly from the back-scattered flux

$$F_{ex}(R) \simeq \frac{L_{w,bol}}{4\pi R_{w,tr}^2}\left(\frac{R_{w,tr}}{R}\right)^{-3} \tag{3.123}$$

where $L_{w,bol}$ is the bolometric luminosity from the wind, eq (3.121). Since the flux in the back-scatter ERF drops off rapidly above the photosphere, the (isotropic) EIC luminosity from above the photosphere mostly comes from radii $R \sim R_{w,tr}$

$$\begin{aligned} L_{IC}^{(1)} &\simeq \begin{array}{l} \Gamma^2\gamma_e^2\left[F_{ex}(R)\min\left(\tau_{trvs}(R),1\right)2\pi R^2\theta_j\right]_{R_{w,tr}} \\ \times\ \min\left(\frac{4}{\theta_j^2},4\Gamma^2\right) \end{array} && (3.124) \\ L_{IC}^{(1)} &\simeq \min\left(1,\theta_j^2\Gamma^2\right)\Gamma^2\gamma_e^2\tau_r(R_{w,tr})L_{w,bol} && (3.125) \end{aligned}$$

where τ_r is the jet optical depth in the radial direction, eq (3.109), and in the second approximation we have used $R_{w,tr} > R_{j,self}$ (usually true). We can see that the EIC process above the photosphere boosts the wind luminosity by a factor of

3.6.3.2 EIC below the photosphere

In the wind region below $R_{w,tr}$ and far from the jet funnel, the radiation energy density U is nearly isotropic, except for a small net flux pointing outwards

$$F_{ex}(R) \simeq \frac{U(R)c}{3\tau_w(R)} \propto \begin{cases} R^{-5/3} & \text{if } R < R_{w,adv} \\ R^{-2} & \text{if } R_{w,adv} < R < R_{w,tr} \end{cases} \qquad (3.126)$$

Near the jet funnel, this net flux enters the jet funnel and the UV photons may be scattered by the jet. At radius $R < R_{j,self}$, the flux entering the funnel is immediately scattered by the jet. At radii $R_{j,self} < R < R_{w,tr}$, photons will completely penetrate the jet in the transverse direction and each funnel wall will feel the existence of the opposite side. In this case, the photon field in the funnel tends to isotropize and approach the same energy density as in the surrounding wind. The number of photons escaping along the radial direction of the funnel are negligible. The only process that prevents the isotropization of the UV photons is the removing of photons by jet scattering. Therefore, we expect the photon field to isotropize when the jet optical depth τ_{trvs} is too small to remove photons away from the funnel. The photon field will isotropize when the removing rate equals to the injecting rate

$$\tau_{trvs} U c = \frac{Uc}{3\tau_w}, \text{ i.e. } \tau_{trvs}\tau_w = \frac{1}{3} \tag{3.127}$$

Note that we use τ_{trvs} instead of $\tau_{j,r}$ because the isotropization happens locally (from R to $R+dR$) in the transverse direction. From Eq.(3.127), we get $r_{w,iso}$, the (dimensionless) 'isotropization radius"

$$r_{w,iso} \simeq 96 m_6^{-1/2} \dot{m}_{w,1}^{1/2} r_{o,1}^{1/4} \left(\frac{L_{j,48}\theta_{j,-1}}{\Gamma_1}\right)^{1/2} \tag{3.128}$$

Above $r_{w,iso}$ the ERF in the funnel is not affected by jet. In this region, the energy density of ERF will reach the same value inside of the funnel as inside of the wind, U. Comparing eq (3.128) with eq (3.118), we can see that the difference between $r_{w,adv}$ and $r_{w,iso}$ is usually small.

Therefore, the (isotropic) EIC luminosity from below $R_{w,tr}$ is

$$\begin{aligned} L_{IC}^{(2)} \quad \simeq \quad & \Gamma^2 \gamma_e^2 \int_{R_{min}}^{R_{w,tr}} \min\left(\tau_{trvs} U c, \tfrac{Uc}{3\tau_w}\right) 2\pi R \theta_j dR \\ & \times \ \min\left(\tfrac{4}{\theta_j^2}, 4\Gamma^2\right) \end{aligned} \tag{3.129}$$

$$\begin{aligned} L_{IC}^{(2)} \quad \simeq \quad & L_{w,bol} \tfrac{2\gamma_e^2 \Gamma^2}{\theta_j} \min\left[1, \left(\tfrac{R_{w,iso}}{R_{w,adv}}\right)^{1/3}\right] \\ & \times \min\left(1, \theta_j^2 \Gamma^2\right) \end{aligned} \tag{3.130}$$

where the the lower limit of the integration, R_{min}, is the radius where the jet accelerated to high Lorentz factor Γ. Below the wind launching radius $R_o \simeq 2R_p$, the ERF possibly comes directly from the inner disk, which is theoretically very uncertain[2]. Fortunately, the contribution from the radii near R_o is small, because most of the EIC luminosity comes from the region

---

[2] See the discussion about super-Eddington accretion with mass loss in Shakura & Sunyaev (1973); Poutanen et al. (2007); Dotan & Shaviv (2011); Begelman (2012).

$R \simeq \min(R_{w,iso}, R_{w,adv}) \gg R_o$. We can see that the EIC process below the photosphere boosts the wind luminosity by a factor of $\sim 2\Gamma^2\gamma_e^2/\theta_j$.

3.6.4 External Inverse-Compton Spectrum

As shown in subsection 3.6.3, EIC emission could come from above and below the photosphere, with EIC luminosities given by $L_{IC}^{(1)}$ (eq 3.124) and $L_{IC}^{(2)}$ (eq 3.130) respectively. Usually, $L_{IC}^{(1)} \ll L_{IC}^{(2)}$. Therefore, we consider the spectrum from below the photosphere ($R < R_{w,tr}$) first and see if it can reproduce the X-ray power law.

Since most of the EIC luminosity comes from the region $R \sim R_{w,iso} \sim R_{w,adv}$ (for simplicity, we ignore the difference between $R_{w,iso}$ and $R_{w,adv}$ hereafter), the νf_ν peak energy of the EIC spectrum is

$$h\nu_p \simeq \Gamma^2\gamma_e^2 3kT_{adv} \simeq 5\Gamma_1^2\gamma_e^2 r_{o,1}^{1/24} m_6^{-1/4} \dot{m}_{w,1}^{-5/12} \text{ keV} \tag{3.131}$$

From eq (3.119) and (3.130), we can see that the EIC emission from below the advection radius ($R < R_{w,adv}$) has a power- law shape

$$\frac{dL_{IC}}{dT} = \frac{dL_{IC}}{dR}\frac{dR}{dT} \propto \frac{RU(R)}{\tau_w(R)} R^{5/3} \propto T^{-3/2} \tag{3.132}$$

We can see that the EIC spectrum above the peak energy ν_p is $F_\nu \propto \nu^{-3/2}$, which is too soft to explain the observations ($F_\nu \propto \nu^{-0.8}$ or $\propto \nu^{-0.4}$ at late time). Around ν_p, there's a big bump coming from the EIC emission at radii $R > R_{w,adv}$. Below ν_p, we expect a blackbody shape, $f_\nu \propto \nu^2$. Simply tuning Γ or γ_e will not work because changing these parameters only changes the position of ν_p but not the the high-energy power-law index.

A possible solution is the case where electrons in the jet have a power-law distribution $dN_e/d\gamma_e \propto \gamma_e^{-p}$ ($\gamma_{e,min} < \gamma_e < \gamma_{e,max}$). If so, we expect the high-energy EIC spectrum to be $f_\nu \propto \nu^{-(p-1)/2}$. An electron population with $p = 2.6$ will reproduce the observed power-law[3] $F_\nu \propto \nu^{-0.8}$. The range of electrons' Lorentz factors must satisfy $\gamma_{e,max}/\gamma_{e,min} \geq (10 \text{ keV}/0.3 \text{ keV})^{1/2} \simeq 5.8$, or $(150 \text{ keV}/0.3 \text{ keV})^{1/2} \sim 20$ (if including the BAT data). If we convolve eq (3.130) with the electrons' Lorentz factor distribution, the isotropic EIC luminosity within the XRT band $(0.3 - 10 \text{ keV})$ becomes

$$L_{IC}^{XRT} \simeq \frac{8\Gamma^2\gamma_{e,min}^2}{\theta_j}\left(\frac{\gamma_{e,0.3\mathrm{keV}}}{\gamma_{e,min}}\right)^{3-p} L_{w,bol} \tag{3.133}$$

This equation matches the observed XRT luminosity within a factor of 20% when $2 < p < 3$. In eq (3.133), $\gamma_{e,0.3\mathrm{keV}}$ is the electron's Lorentz factor corresponding to scattered photons' energy 0.3 keV.

To reproduce the XRT observations, including the luminosity in the $0.3 - 10$ keV band, L_X, and the power-law spectrum, we have two equations

$$\Gamma^2\gamma_{e,min}^2 3kT_{adv} \leq \Gamma^2\gamma_{e,0.3\mathrm{keV}}^2 3kT_{adv} = 0.3(1+z) \text{ keV} \tag{3.134}$$

$$L_X \simeq \frac{8\Gamma^2\gamma_{e,min}^2}{\theta_j}\left(\frac{\gamma_{e,0.3\mathrm{keV}}}{\gamma_{e,min}}\right)^{3-p} L_{w,bol} \tag{3.135}$$

where z is the redshift. Using $z = 0.35$, $p = 2.6$, T_{adv} from Eq.(3.120), $L_{w,bol}$ from Eq.(3.121) and $L_X = 10^{47} L_{X,47}$ erg s^{-1}, we find

$$\Gamma\gamma_{e,min} \lesssim 3\, r_{o,1}^{-1/48} m_6^{1/8} \dot{m}_{w,1}^{5/24} \tag{3.136}$$

$$\Gamma\gamma_{e,min} \simeq 4\, \theta_j^{5/8} L_{X,47}^{5/8} r_{o,1}^{5/24} m_6^{-5/8} \dot{m}_{w,1}^{-5/32} \tag{3.137}$$

If we use $\theta_j \simeq 1/\Gamma$, the second inequality restricts the jet Lorentz factor to a very small value $\Gamma \lesssim 2$, which is inconsistent with the constraints from variability time scale $\delta t \simeq 10^2$ s.

---

[3] At later time, the observed spectrum becomes slightly harder ($f_\nu \propto \nu^{-0.4}$). From eq (3.120), we can see that T_{adv} increases with time, so the EIC spectrum in the XRT band $(0.3 - 10 \text{ keV})$ will get harder at later time.

If the EIC emission comes from above the photosphere ($L_{EIC}^{(1)}$ in eq 3.124), we substitute θ_j in the second inequality above by $2/\tau_{j,r}(R_{w,tr})$, i.e.

$$\begin{aligned}
\Gamma\gamma_{e,min} &\lesssim 3\ r_{o,1}^{-1/48} m_6^{1/8} \dot{m}_{w,1}^{5/24} && (3.138)\\
\Gamma\gamma_{e,min} &\simeq 6\ \tau_{j,r}^{-5/8}(R_{w,tr}) L_{X,47}^{5/8} r_{o,1}^{5/24} m_6^{-5/8} \dot{m}_{w,1}^{-5/32} && (3.139)
\end{aligned}$$

Since $\tau_{j,r}(R_{w,tr})$ can range from $0.1 - 1$, the EIC emission from above the photosphere gives less stringent constraints on the Lorentz factors than from below the photosphere. Recall that the wind mass loss rate is $\dot{m}_w = f_{out}\dot{m}_{fb}$. In the first few weeks $\dot{m}_{fb} \sim 10^2$, so the EIC model is marginally consistent with the observations if: (1) the EIC emission comes from above the photosphere, (2) the wind mass loss has high efficiency $f_{out} \simeq 1$, (3) the jet Lorentz factor is not too high $\Gamma \lesssim 5$, and (4) electrons' minimum Lorentz factor $\gamma_{e,min} \simeq 1$.

As pointed out in §3.5, hot electrons suffer from strong cooling, due to the inverse Compton scattering of the observed XRT X-ray photons. The ratio of IC cooling timescale to the dynamical timescale for an electron with Lorentz factor γ_e at radius R is

$$\frac{t'_{\rm IC}}{t'_{\rm dyn}} = \frac{4\pi R\Gamma^3 m_e c^3}{L_x \gamma_e \sigma_T} \simeq 4.6 \times 10^{-2} L_{X,47}^{-1} R_{13} \Gamma_1^3 \gamma_e^{-1} \qquad (3.140)$$

Therefore, all electrons are in the fast cooling regime. To achieve a final power-law index of 2.6, the acceleration mechanism must be injecting electrons with original power-law index $p = 1.6$, which is hard to achieve in shocks.

3.7 Photospheric model of TDE SW J1644+57

Another mechanism that has been studied in relativistic jets in order to explain non-thermal emission, in the context of GRBs, is the photospheric process (Thompson, 1994; Ghisellini & Celotti, 1999a; Mészáros & Rees, 2000;

Rees & Mészáros, 2005; Thompson et al., 2007; Pe'er, 2008; Giannios, 2008; Beloborodov, 2010). Unlike the other mechanisms discussed in this work, the spectrum for the photospheric process is produced while the medium is optically thick. In this section, we determine if the high-energy spectrum of the photospheric process can explain the hard $f_\nu \propto \nu^{-0.8}$ X-ray spectrum observed in Sw J1644+57. To model the X-ray and gamma-ray observations of SW J1644+57 with the photospheric process, we first briefly describe the expected spectrum for the photospheric process. We then discuss the conditions that need to be satisfied to apply the photospheric process to SW J1644+57. Then, we discuss a Monte Carlo (MC) code we used to simulate the photospheric process, described in greater detail in (Santana et al., 2015). finally, we discuss the results for the output spectrum from our photospheric simulations.

3.7.1 Spectrum for Photospheric Process

The predicted spectrum for the photospheric process is a smoothly joined power-law, with a spectrum below the peak energy ranging from $f_\nu \propto \nu^2$ to $f_\nu \propto \nu^0$ (Vurm et al., 2013; Lundman et al., 2013; Deng & Zhang, 2014) and a typical spectrum above the peak energy $f_\nu \propto \nu^{-1}$ (Lazzati & Begelman, 2010). The main goal of the photospheric process is to broaden a blackbody (BB) spectrum by Comptonization, i.e. hot electrons IC scattering photons multiple times (Pozdnyakov et al., 1983). The seed photons for the photospheric process are assumed to be produced near the central engine. As the jet travels outward, the photons are advected with the outflow and are taken to quickly thermalize into a BB spectrum since the jet is initially very optically thick. When the optical depth of the outflow reaches $\sim 2-5$, a dissipation event is assumed to occur, which accelerates electrons to mildly relativistic speeds. The hot electrons then IC scatter the photons to higher energies. A power-law spectrum is developed above the initial BB peak because only a fraction f of the photons get scattered once by a hot electron to higher energies, only a fraction f^2 of the photons get scattered twice by a hot electron to higher energies, and so on (Lazzati & Begelman, 2010; Ghisellini, 2013). Determining the spectral slope analytically for the high-energy spectrum of the photospheric process is difficult. Thus, we use MC code from Santana et al. (2015) to simulate the photospheric process for TDE parameters. However, before discussing the code, we determine if there is a parameter space where the jet is optically thick so that we can apply the photospheric process and we also determine the number of photons and electrons needed to simulate the photospheric process.

3.7.2 Photospheric Radius and Photon to Electron Ratio for SW J1644+57

The optical depth to Thomson scattering in a baryonic jet, i.e. a jet where the kinetic energy of the outflow is primarily carried by protons, is given by

$$\tau = \frac{L\sigma_T}{8\pi m_p c^3 \Gamma^3 R}, \tag{3.141}$$

where σ_T is the Thomson cross-section, m_p is the proton mass, and R is the distance from the central engine in the observer frame. From the equation for τ, we can determine the location of the photospheric radius ($R_{\rm ph}$), i.e. the location where the medium becomes optically thin and the photon spectrum is no longer significantly modified since the probability for an electron scattering a photon is low. Setting $\tau = 1$ in Equation 3.141 and solving for R, we find

$$R_{\rm ph} = \frac{L\sigma_T}{8\pi m_p c^3 \Gamma^3} = (6 \times 10^{11}{\rm cm}) L_{48} \Gamma_1^{-3}. \tag{3.142}$$

In order to ensure that there is a parameter space where the medium is optically thick, the condition $R_S < R_{\rm ph}$ must be satisfied, where R_S is the Schwarzschild radius. Taking the mass of the SMBH for SW J1644+57 to be $1 \times 10^6 M_\odot$, $R_S = (3 \times 10^{11}{\rm cm}) M_6$, where M_6 is the mass of the SMBH in units of $10^6 M_\odot$. For $\Gamma = 10$, $R_{\rm ph}$ is only greater than R_S by a factor of 2. Thus, the only available parameter space for Γ to ensure than $R_S < R_{\rm ph}$ is $2 \leq \Gamma \leq 10$. Already we can see the difficulties faced by the photospheric process. At late times when the X-ray luminosity drops by a factor ~ 100, the optical depth will be less than one for a relativistic jet placed at the Schwarzschild radius. However, the jet will optically thin when it is launched because it will initially be moving at sub-relativistic speeds. Rather, it means that as soon as the jet is accelerated to mildly relativistic speeds, it will become optically thin. Therefore at late times $\Gamma \lesssim 2$ at the photosphere.

Next, we determine the ratio of photons to electrons for the photospheric process for SW J1644+57, since it determines the number of photons and electrons needed for a MC simulation. For a baryonic jet, the ratio of the density of photons in thermal equilibrium in the jet comoving frame (n'_γ) to the electron density in the jet-comoving frame (n'_e) is given by

$$\frac{n'_\gamma}{n'_e} = (2 \times 10^7) \Gamma_1 R_{0,12}^{1/2} L_{48}^{-1/4}, \tag{3.143}$$

where R_0 is the radius at which the outflow is launched. In this expression, R_0 is normalized to a few Schwarzschild radii. Thus, from Equation 3.143, a ratio of photons to electrons $\sim 10^7$ is required to simulate the photospheric process for SW J1644+57.

3.7.3 Input Parameters for MC Photospheric Simulations

We use the MC code described in Santana et al. (2015), where it was used to simulate the photospheric process for the GRB prompt emission. In this work, we apply this code for typical TDE parameters to model Sw J1644+57. The details of the algorithm and implementation of the code can be found in Santana et al. (2015). Here, we discuss the input parameters we use for the MC code to model the x-ray and gamma-ray emission of SW J1644+57 with the photospheric process.

- Γ—In Section 3.7.2, we showed that in order to satisfy $R_S < R_{\rm ph}$, Γ if confined to the range $2 \leq \Gamma \leq 10$. To ensure $R_S < R_{\rm ph}$ is more easily satisfied, we considered $\Gamma = 5$ for our simulations.
- L—We consider $L = 10^{48}$ ergs/s for our simulations.
- $\tau_{\rm initial}$—The optical depth corresponding to the location where the photons are initialized and the location where a dissipation event, which heats up the electrons, is assumed to occur. We consider values in the range $\tau_{\rm initial} \sim 2-5$. The distance from the central engine in the observer frame, R, for a particular τ, can be found with Equation 3.141.
- $\tau_{\rm ph}$—The optical depth corresponding to the location of the photosphere. We consider $\tau_{\rm ph} = 1$ for our simulations.
- N_e—The number of electrons in a simulation. Previous MC photospheric simulations (Lazzati & Begelman, 2010; Chhotray & Lazzati, 2015) have shown that 10^3 electrons are enough to get an accurate representation for an electron distribution. However, since we are considering a photon to electron ratio of 10^7 (Equation 3.143), considering $N_e = 10^3$ would

mean that we would need to consider 10^{10} photons. Since simulating 10^{10} photons is very computationally expensive for our code (we would need $\sim$ 850 GB of RAM for our code), we instead consider $N_e = 100$.

- N_γ—The number of photons in a simulation. Since we consider $N_e = 100$, to reach $N_\gamma/N_e = 10^7$, we consider $N_\gamma = 10^9$ for our simulations.

- T'_γ—The photons are initialized to have a Blackbody (BB) spectrum with temperature T'_γ in the jet comoving frame. Since the observed spectrum in the XRT-BAT band is a single power-law, the photospheric spectrum must peak below 0.3 keV (low-energy end of XRT band). Thus, we consider $k_B T'_\gamma = 6$ eV so that the spectrum peaks at $2.8 k_B T'_\gamma \Gamma/(1+z) \sim 0.1$ keV in the observer frame.

- Electron Distribution—We consider two different distributions for the electrons: 1. mono-energetic electrons (all electrons initialized to the same electron Lorentz factor γ_e) with the initial γ_e of the electrons as the input parameter. 2. Maxwell-Boltzmann (MB) distribution of electrons with T'_e as an input parameter.T'_e is the temperature of the electrons in the jet comoving frame. Since the electrons are assumed to be heated through an unknown dissipation mechanism after the photons have a BB spectrum, $T'_e \gg T'_\gamma$.

- N_{collect}—The number of photons collected for the output spectrum. We consider $N_{\text{collect}} = N_\gamma/3$ for our simulations as in previous MC simulations Lazzati & Begelman 2010; Santana et al. 2015. By plotting the first $N_\gamma/3$ photons that escape the photosphere for an output spectrum, we are plotting a time-averaged spectrum.

Lastly, we discuss the values we consider for γ_e, or T'_e, and electron re-heating. γ_e is a very important parameter since it determines the available energy electrons have to transfer to photons. In the photospheric model, in order to avoid synchrotron cooling from the magnetic field that is expected to be present in the jet, the synchrotron emission must be self-absorbed. The largest γ_e that can be considered is found by setting the optical depth for synchrotron self-absorption equal to 1. For a MB distribution distribution of electrons, the synchrotron self-absorption optical depth $\tau_{\text{syn}}^{\text{MB}}$ is given by (Rybicki & Lightman, 1986; Lazzati & Begelman, 2010)

$$\tau_{\text{syn}}^{\text{MB}} = \frac{10^{10}}{(\gamma_e)^5 \epsilon_B^{1/2} (E'_\gamma/10 \text{ eV})^2}. \tag{3.144}$$

In this equation, $E'_\gamma \sim 2.8 k_B T'_\gamma$ is the peak energy of the BB spectrum in the jet-comoving frame and $\epsilon_B = U'_B/U'_{\text{rad}}$, where U'_B (U'_{rad}) is the energy density in the magnetic field (radiation). Setting $\tau_{\text{syn}}^{\text{MB}} = 1$, for $\epsilon_B \sim 0.1$ (magnetic field subdominant to radiation) and $E'_\gamma \sim 2.8 \times 6$ eV, the upper limit we find is $\gamma_e \sim 100$.

For mono-energetic electrons, we considered all electrons initialized to $\gamma'_e = 2$, 30, and 100. For MB distribution electrons, we considered $k_B T'_e = (2-1) m_e c^2$, $k_B T'_e = (30-1) m_e c^2$, and $k_B T'_e = (100-1) m_e c^2$ ($k_B T'_e = (\gamma'_e - 1) m_e c^2$ since $k_B T'_e$ measures the kinetic energy of the electrons).

Lastly, as we will show later in this section, the electrons rapidly cool by IC scatterings and then the electrons no longer have much energy to transfer to the photons. Therefore to match the observed spectra in TDEs, we require electron re-heating to increase the energy electrons have available to transfer to photons. In our code, we can specify the number of re-heating events. After

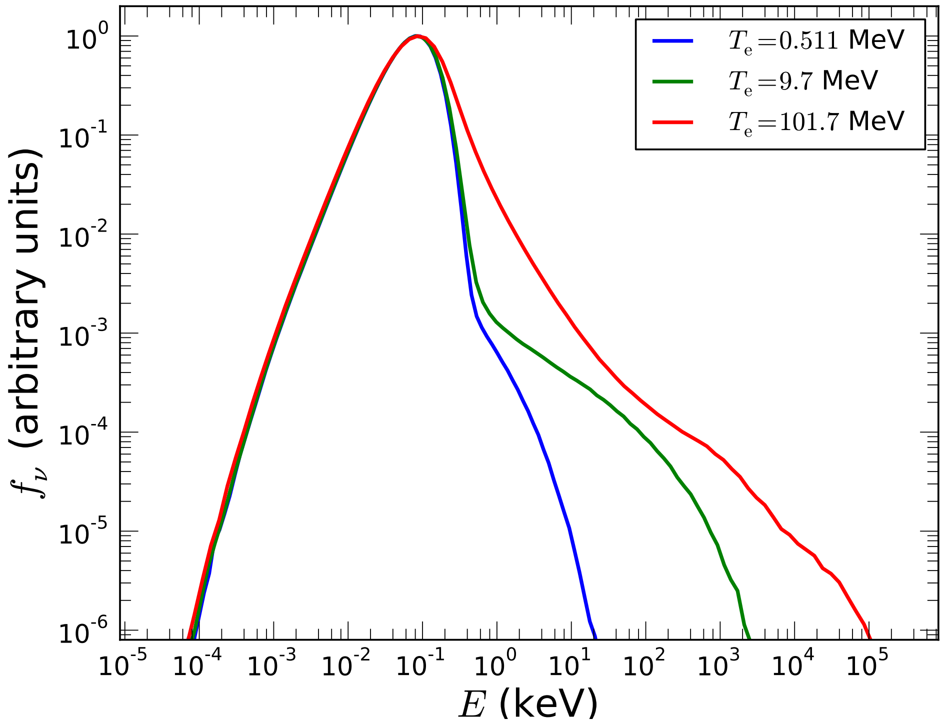

Figure 3.4: MC photospheric simulation results for peak normalized spectrum for $\tau_{\text{initial}} = 2$ and MB electron with $k_B T'_e = (2-1)m_e c^2, (30-1)m_e c^2, (100-1)m_e c^2$.

a re-heating event, we simply bring the electrons back to the same distribution that they were initialized to.

3.7.4 MC Photospheric Simulation Results With One Electron Heating Event

In Figure 3.4, we show simulations for $\tau_{\text{initial}} = 2$ and for MB electrons with initial $k_B T'_e = (2-1)m_e c^2, (30-1)m_e c^2, (100-1)m_e c^2$. The simulations with $k_B T'_e = (2-1)m_e c^2, (30-1)m_e c^2$ show a sharp drop in f_ν by ~ 3 orders of magnitude after the peak energy, in disagreement with the expected spectrum for the photospheric model and the observed x-ray spectrum for SW J1644+57. The spectrum for the simulation with $k_B T_e' = (100 - 1) m_e c^2$ is beginning to show a power-law above the peak energy, but the spectrum is still curved and not quite a power-law yet. Furthermore, it is far softer than the observed Sw J1644+57 spectrum.[4]

To understand why there is a huge drop off just above the peak energy of the spectrum, we need to determine the number of photons that need to be upscattered to energies larger than $E'_{\rm pk}$ (peak energy of BB in jet-comoving frame) to produce a power-law. We refer to this quantity as $N_{\rm pl}$. We then compare $N_{\rm pl}$ to the total number of photons that are upscattered to energies larger than $E'_{\rm pk}$ in a MC simulation, which is given by the number of scatterings it takes to cool an electron ($N_{\rm cool}$) times the total number of electrons in a simulation (N_e). Thus, in order to produce a power-law above $E'_{\rm pk}$, we need the condition

$$N_e N_{\rm cool} \sim N_{\rm pl} \tag{3.145}$$

to be satisfied. We now compute $N_{\rm pl}$ and $N_{\rm cool}$ for our MC simulations.

3.7.4.1 Estimating $N_{\rm pl}$

To produce a power-law above the peak energy, a large fraction of the photons near the peak need to be upscattered to higher energies. Thus,

---

[4] Some of the spectra, say $\gamma_e \sim 20$, show a hard power-law after the initial drop off. One might think it is possible to have this power-law in the XRT-BAT band. Then the huge bump around the peak will be hidden in the soft X-rays where it will be absorbed by the host galaxy absorption, and not possible to be observed. However, the energy carried in this component far exceeds the energy in the X-rays, by a factor 10^3, and therefore such a scenario can be ruled out.

denoting the number of photons near the peak energy as $N_{\rm pk}$, we approximate $N_{\rm pl} \sim N_{\rm pk}$. In a BB spectrum, the majority of the photons are near the peak energy. Since the total number of photons in an output spectrum for our simulations is $N_{\rm collect} = N_\gamma/3$, we approximate $N_{\rm pl} \sim N_{\rm pk} \sim N_\gamma/3 \sim 3 \times 10^8$. For a more detailed discussion on the estimate for $N_{\rm pl}$, see Santana et al. (2015).

3.7.4.2 Estimating $N_{\rm cool}$

$N_{\rm cool}$ is the number of times an electron can IC scatter a photon before the electron is cooled to an energy where it no longer has enough energy to help populate the non-thermal power law. Or in other words, $N_{\rm cool}$ is approximately the number of photons a single electron can put into the non-thermal power law in the photospheric process. We derive $N_{\rm cool}$ in this subsection.

In the Thomson regime, a single inverse Compton scattering of a photon with energy E'_γ by an electron with Lorentz factor γ will cause the electron to lose energy by an amount

$$\Delta E \approx -\frac{4}{3}\gamma^2\beta^2 E'_\gamma \tag{3.146}$$

In the Thomson regime, the energy lost per scattering is small and eq (3.146) can be treated as an differential equation. Solving this differential equation, we find the total number of scatterings it takes for an electron to go from γ_i to γ_f

$$N_{\rm sc} = \frac{3}{8}\frac{m_e c^2}{E'_\gamma} \ln\left[\frac{(\gamma_i - 1)(\gamma_f + 1)}{(\gamma_i + 1)(\gamma_f - 1)}\right] \tag{3.147}$$

For an electron to significantly change the energy of the photon in an IC scattering, $\frac{4}{3}\gamma^2\beta^2 \gtrsim 2$. Therefore, we calculate $N_{\rm cool}$ using eq (3.147) with $\gamma_f \sim \sqrt{5/2}$.

$$N_{\rm cool} \approx \frac{3}{8}\frac{m_e c^2}{E'_\gamma}\left\{\ln\left[\frac{(\gamma_i - 1)}{(\gamma_i + 1)}\right] + 1.5\right\} \qquad (3.148)$$

In Sw J1644+57, $E_\gamma = 2.8T'_\gamma = 16.8$ eV. When $\gamma_i = 2$, $N_{\rm cool} = 4500$. When $\gamma_i \gg 1$, $N_{\rm cool} \sim 1.7 \times 10^4$. To smoothly join a high energy power-law above the blackbody peak, $N_{\rm cool}N_e \sim N_{\rm pl}$, or $N_{\rm cool} \gtrsim \frac{1}{3}n_\gamma/n_e$. We showed in eq (3.143) that $n_\gamma/n_e \sim 10^6$ when $\Gamma = 5$ and $N_{\rm cool}$ is always $\lesssim 1.7 \times 10^4$. Since $N_{\rm cool} \ll n_\gamma/n_e$ for both mildly relativistic and relativistic electrons, not enough photons are upscattered to higher energies to populate a smoothly-joined power-law spectrum for the simulations with one heating event.

3.7.5 Estimating Number of Electron Re-heating Events Needed To Produce A Power-Law Spectrum

$N_{\rm cool}$ from the previous subsection can be used to calculate $N_{\rm reheat,min}$, the minimum number of re-heating events needed to populate a power-law spectrum above the peak energy. With $N_{\rm reheat}$ electron re-heating events, the number of photons that can be upscattered to higher energies is $\sim N_{\rm reheat}N_E N_{\rm cool}$. $N_{\rm reheat,min}$ is found by the condition where enough photons are upscattered to energies larger than $E'_{\rm pk}$ to populate a power-law spectrum, i.e. $N_E N_{\rm cool} N_{\rm reheat} \sim N_{\rm PL}$, or

$$N_{\rm reheat,min} N_{\rm cool} \sim \frac{1}{3}\frac{n_\gamma}{n_e} \qquad (3.149)$$

is satisfied. Thus, $N_{\rm reheat,min} = n_\gamma/(3n_e N_{\rm cool})$. For $\gamma_i \sim 2$, $N_{\rm reheat,min} \sim (3 \times 10^6)/(4500) \sim 740$, and for highly relativistic electrons ($\gamma_i \gg 1$) $N_{\rm reheat,min} \sim (3 \times 10^6)/(1.7 \times 10^4) \sim 175$. Therefore, to match the observed spectrum in Sw J1644+57, the electrons must be reheated many times just below the photosphere. If the variability timescale for the reheating is linked to the central engine (*e.g.*, in internal shocks), a single reheating event can happen on a timescale $\sim R_s/c$. By the time there has been N_{reheat} number of reheatings, the jet will have traveled $\sim N_{\text{reheat}} c t_{\text{var}} \sim N_{\text{reheat}} R_s$. Since we predict we will need $\gtrsim 100$ reheating events, the radius of emission must be greater than $100 R_s \sim 3 \times 10^{13}$ cm, and the radius of emission is much greater than the photosphere. Therefore, the reheating must occur in a process that can happen at much smaller timescales than the dynamical time of the Schwarzschild radius.

3.8 Poynting-Dominated jet

The idea that the relativistic jets in AGN extract energy from the SMBH through magnetic fields through some sort of Blandford-Znajek (Blandford & Znajek, 1977) process has observational and theoretical evidence (*e.g.*, Begelman et al., 1984; Vlahakis & Königl, 2004; Tchekhovskoy et al., 2011; Ghisellini et al., 2014). The jets in tidal disruptions such as Sw J1644+57 may also be powered by magnetic flux, but the magnetic flux from the star is not enough to power a TDE without some sort of dynamo that is capable of generating a large scale magnetic field (Bloom et al., 2011). Others have suggested that the stellar debris could bring in the magnetic flux from a fossil accretion disk as it returns to the pericenter (Kelley et al., 2014). The possibility that Sw J1644+57 is magnetically dominated was considered by Burrows et al. (2011); Tchekhovskoy et al. (2014); Piran et al. (2015). In this section we model the consequences of a Poynting-dominated jet on the observed radiation of Sw J1644+57.

How the magnetic energy is dissipated in astrophysical systems through reconnection is not well understood. Instead of modeling the details of the reconnection process, we use the general considerations for any reconnection process derived through basic global properties of the magnetic field. We provided these derivations in Chapter 2 of this thesis. As we have shown in the previous sections, fast cooling of the keV producing electrons is nearly unavoidable in Sw J1644+57; this is because the cooling time is very short when compared to the dynamical time. This short cooling time forces the source injecting hot electrons to do so rapidly. If the electrons are not reheated, excess flux can occur at lower wavelengths. Magnetic reconnection models can avoid this problem in two ways. First, the acceleration process can happen throughout a large domain in which the electrons can spend a significant fraction of time. In these acceleration regions, the electrons will not cool significantly until the rate at which they lose energy is greater than the rate at which they gain energy through magnetic reconnection. Secondly, there are multiple reconnection regions that are radiating all at once. After leaving a reconnection region, the electron will cool rapidly, as before. However, it can enter into another reconnection site and be reaccelerated.

When the jet is magnetically dominated, the magnetic field is

$$B_0' = \frac{(L/c)^{1/2}}{\Gamma R} = (580\ \mathrm{G})\ \frac{L_{48}^{1/2}}{\Gamma_1 R_{15}}; \tag{3.150}$$

L is the isotropic equivalent energy in the jet. If electrons in the particle acceleration region are producing keV synchrotron photons, the typical electron Lorentz factor must be

$$\gamma_i \approx \left[\frac{2\pi m_e \nu R c^{3/2}}{q L^{1/2}(1+z)^{-1}}\right]^{1/2} = 4\times 10^3 \frac{[R_{15}\nu_{\mathrm{kev}}(1+z)]^{1/2}}{L_{48}^{1/4}}. \tag{3.151}$$

The total number of electrons radiating at 1 keV to an observed flux f_ν is

$$N_e \approx 1.2\times 10^{49} f_{\nu,\mathrm{mJy}} L_{48}^{-1/2} R_{15} d_{L,28}^2 (1+z)^{-1}, \tag{3.152}$$

and the corresponding luminosity carried by these electrons is

$$\begin{aligned} L_e &\approx \frac{N_e m_e c^3 \gamma_e \Gamma}{(R/\Gamma^2)} \\ &= (1.2\times 10^{42}\ \mathrm{erg\,s^{-1}}) \frac{\Gamma^3 f_{\nu,mJy} R_{15}^{1/2} d_{L,28}^2 \nu_{keV}^{1/2}}{L_{48}^{3/4}(1+z)^{1/2}}, \end{aligned} \tag{3.153}$$

Since the energy carried by electrons cannot exceed the energy in magnetic fields for a Poynting jet, we find following constraint on the bulk Lorentz factor

$$L_e/L \lesssim 1 \quad \Longrightarrow \quad \Gamma \lesssim 90\, \frac{L_{48}^{7/12}(1+z)^{1/6}}{f_{\nu,mJy}^{1/3} R_{15}^{1/6} d_{L,28}^{2/3} \nu_{keV}^{1/6}}. \tag{3.154}$$

The reason for the approximate inequality sign in the above equation is because magnetic fields of a Poynting jet could be compressed by a factor a few and thus L_e could in principle exceed L by order unity.

The Compton $\widetilde{Y}$ of the radiating electrons is

$$\widetilde{Y} = 10\ \nu_{\mathrm{keV}} f_{\nu,\mathrm{mJy}} L_{48}^{-1} d_{L,28}^2 \tag{3.155}$$

Assuming an X-ray efficiency of 10% (*i.e.*, $L_{48} \sim 3$) and a flux at 1 keV of $f_{\nu,\mathrm{mJy}} \sim 0.1$, we find that $\widetilde{Y}$ is ~ 0.1 This value means that if the jet is transparent to the peak of the SSC emission, there will be an LAT excess unless Y is suppressed due to Klein-Nishina effects. As R increases, the opacity due to pair production decreases, but γ_i also increases. At about $R \sim 10^{16}$cm, the entire XRT band is Klein-Nishina suppressed, and the LAT constraint is no longer an issue as long as the minimum Lorentz factor of the electrons is $\sim \gamma_i$. We calculated the expected integrated flux SSC in the LAT band using eq (3.37) accounting for both Klein-Nishina suppression and using the observed X-ray flux and an electron distribution given by $n = (\gamma/\gamma_i)^{-2.6} N_e/(4\pi R^2 (R/\Gamma))$, using the γ_i, N_e given in eqs (3.151) & (3.152) . If the integrated flux is greater than 8.5×10^{-11} erg/s/cm^2, then the parameter space is ruled out for any photospheric model. We show the allowed R—Γ parameter space in Figure 3.5.

Assuming that there are ${\eta_p}^5$ protons for every electron with LF $\sim \gamma_i$, the luminosity carried by protons is

$$L_p = 5 \times 10^{41} \frac{\Gamma^3 \eta_p f_{\nu,\mathrm{mJy}} d_{L,28}^2}{L_{48}^{1/2}(1+z)} \tag{3.156}$$

The magnetization parameter $\sigma \equiv B'^2/(8\pi n_e' m_p c^2) = L/L_p$ is then

$$\sigma = 2 \times 10^6 \ \Gamma^{-3} \eta_p^{-1} f_{\nu,\mathrm{mJy}}^{-1} L_{48}^{3/2} d_{L,28}^{-2}(1+z) \tag{3.157}$$

If the percentage of electrons that are accelerated to is $\sim$ 5%, $\Gamma \sim 20$, the overall luminosity of the jet $L_{48} \sim 3$ (corresponding to a radiative efficiency of 10%), and $f_{\nu,\mathrm{mJy}} \sim 0.1$, the magnetization parameter $\sigma \sim 2800$ at the emission radius. At the base of the jet the magnetization is larger by a factor of Γ and is 5.5×10^4. These values mean that the jet is highly magnetized. σ could be smaller if the jet is very efficient at converting its Poynting flux to radiation. If the radiation efficiency is $\sim$ 50%, the magnetization (at the emission region) would be $\sim$ 250 and 5000 at the base of the jet (assuming a $\Gamma \sim 20$).

Following Kumar & Crumley (2015, *in prep*), we assume that, inside of a causally connected region of the jet, there are a number of acceleration sites where electron acceleration takes place. We assume that, on average electrons,

---

[5] If there are no $e^{\pm}$ pairs, $\eta_p \geq 1$. It is unlikely that the jet will be pair-dominated, because for the majority of the kinetic energy of the jet to be in pairs there must be 1000 pairs to every proton. The temperature at the base of the jet is simply not high enough for electron positron pairs to be thermal. If there are a significant number of pairs in the jet η_p could be less than one and the estimated magnetization parameter would be larger than the value estimated in this section.

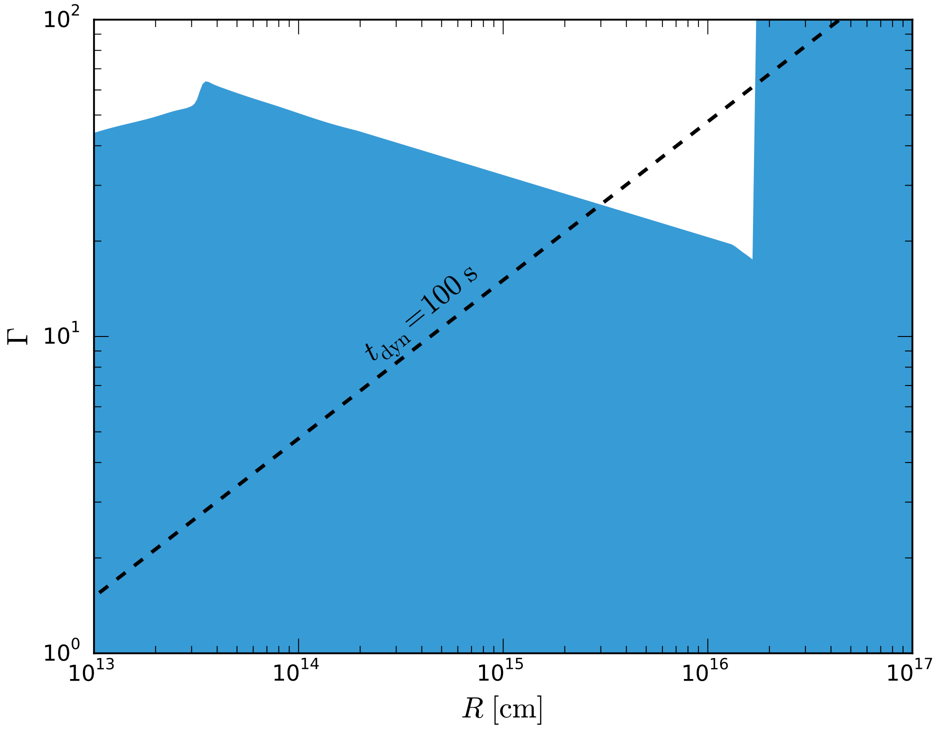

Figure 3.5: The available parameter space for any magnetic jet model that will not violate the LAT upper limits for Sw J1644+57. We assumed a 10% efficiency for the jet, and matched the average keV flux of Sw J1644+57. The blue region is the parameter space where there won't be a LAT excess due to self-Compton scattering of keV photons. The sharp rise at 10^{14} cm is the where the electrons producing the hot X-rays ($>$ 10 keV) become Klein-Nishina suppressed. The sharp rise at $\sim 10^{16}$ cm occurs because the electrons producing the soft X-rays become Klein-Nishina suppressed as well. Other considerations may rule out some of the space in blue; for instance it is unlikely that $\Gamma \gg 10$.

spend a time $\xi t'_{\rm dyn}$ in a current sheet. Inside of these regions, the electrons are heated to a power-law distribution. The hot electrons leave the acceleration regions and then cool through synchrotron radiation. The resulting observed synchrotron spectrum is a superposition of the radiation from electrons inside of the reconnection regions and electrons that have left the reconnection sites. On average, the electron spend $\sim \zeta t'_{\rm dyn}$ of their time outside of the reconnection regions. The cooling electron Lorentz factor is

$$\gamma_c = \frac{7}{\zeta}\Gamma_1^3 R_{16} L_{48}^{-1}, \tag{3.158}$$

with a corresponding synchrotron frequency of

$$\nu_c = 3\times 10^{-7}\ \text{keV}\ \zeta^{-2}\Gamma_1^6 R_{16} L_{48}^{-3/2}(1+z)^{-1} \tag{3.159}$$

If ν_c is $\sim .1$ keV, that is, when R, Γ, are large and $\zeta \ll 1$, the Poynting jet model will work as long as $\nu_i \sim 0.1.keV$. If the X-ray emission is dominated by electrons inside of acceleration regions, the expected value for p is 2.6, and if it is dominated by the electrons outside of the acceleration regions, $p = 1.6$. For a large swatch of the parameter space, ν_c is small enough to potentially cause an infrared excess. However, as we will now show, the emission at 1 keV is likely dominated by electrons inside of the acceleration region. This means that it is no longer true that the spectrum between ν_i and ν_c is $\nu^{-1/2}$. If the emission at ν_i is greatly dominated by electrons inside of accelerations sites, the flux below ν_i will be $\propto \nu^{1/3}$ close to ν_i and it will soften to the $\propto \nu^{-1/2}$ at frequencies much less than ν_i.

The ratio of synchrotron flux inside of the particle acceleration region to the flux outside of the particle acceleration region at 1 keV is calculated as in Kumar & Crumley (2015)

$$\mathcal{R}_{\rm keV} \approx \frac{\xi t'_{\rm dyn}}{t'_{\rm cool}(\gamma_i)}. \tag{3.160}$$

$$\mathcal{R}_{\rm keV} = 6\times10^{3}\xi L_{48}^{3/4}\nu_{\rm keV}^{1/2}(1+z)^{1/2}\Gamma_1^{-3}R_{15}^{-1/2} \tag{3.161}$$

This ratio is $\gg 1$ for the allowed parameter space of Sw J1644+57 as long as ξ is not very small ($\lesssim 10^{-3}$). Because $\mathcal{R}_{\rm keV} \gg 1$, the observed flux is mostly coming from electrons inside of the acceleration region. When this is the case, an infrared excess will be avoided as long as $\mathcal{R}_{\rm keV}$ is sufficiently large. This is shown graphically in figure 3.6

The keV flux contribution from outside of particle acceleration regions is roughly $f_{\rm keV}/\mathcal{R}_{\rm keV}$. From eq (3.159) we know that ν_c is likely below the K-band, so the expected infrared flux is $\sim \mathcal{R}_{\rm keV}^{-1} f_{\rm keV}\left(\nu_{\rm K-band}/\nu_{\rm keV}\right)^{-1/2}$. The flux in the K-band is roughly the same as the average flux at 1 keV, so to prevent particles outside of the particle acceleration region from overproducing the K-band flux, the ratio $\mathcal{R}_{\rm keV}$ must be greater than 30. $\mathcal{R}_{\rm keV} \gtrsim 30$ can be achieved for the entirety of the radial parameter space plotted in Figure 3.5 as long as Γ_1 is less than a few. An example of a spectrum that matches the observed properties is plotted in figure 3.6

One small downside with having the keV emission come from the reconnection regions is that the electron spectral index, p, is related to the observed photon spectral index, β as $\beta = (p-1)/2$. So for a β of 0.8, p should be approximately 2.6. This value is softer than what is observed in particle-in-cell simulations of magnetic reconnection, that generally see a $p < 2$ electron distribution. The softer spectrum could be attributed to the fact that, at any time, we are seeing emission from multiple particle acceleration regions. At late times ($t > 10^7$ s), the spectrum hardens from $\beta = 0.8$ to $\beta = 0.4$ (Saxton et al., 2012). During this time, $p \sim 1.8$, which is consistent with electron PIC simulations.

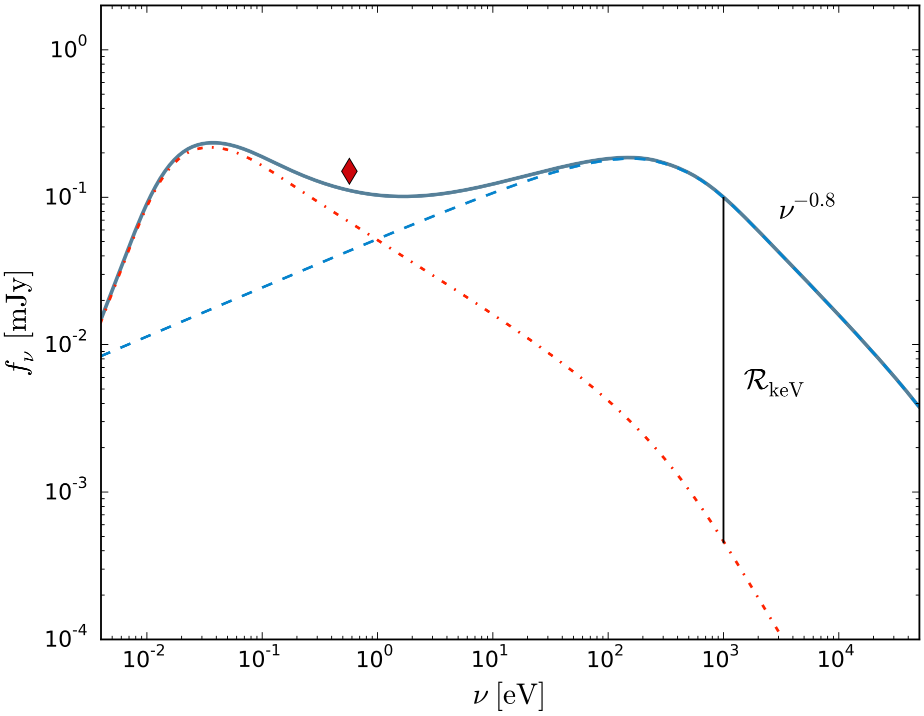

Figure 3.6: A sample spectrum from a Poynting dominated jet matching the observed spectrum of Sw J1644+57 is shown as a solid line. The contributions to the observed flux from the electrons in the particle acceleration region (blue dashed line) and the electrons outside of current sheets (red dash-dotted line). The ratio of the flux from electrons inside of particle acceleration regions to the flux from electrons outside is labeled $\mathcal{R}_k eV$. To avoid a K-band excess, $\mathcal{R}_{\mathrm{keV}}$ must be greater than 30, or ν_c must be greater than 100 eV. The K-band flux is the red diamond plotted at $\sim 1eV$. The parameter were chosen as follows Luminosity in the jet is 3×10^{48} erg/s, $\xi = 5 \times 10^{-3}$, $\zeta = 1 \times 10^{-2}$, $R = 5 \times 10^{14}$ cm, and $\Gamma = 10$.

3.9 Conclusions

A tidal disruption event with a relativistic jet like Sw J1644+57 presents a unique opportunity to test the non-thermal emission models used in modeling other relativistic jets such as the ones observed in AGN and GRB. Sw J1644+57 had a period of intense, high-luminosity flaring that lasted ~ 10 days, allowing for plenty of time to do multi-wavelength measurements in the γ-rays, optical, infrared, and radio. These measurements put strong constraints on the allowed parameter space of any emission model. Since TDEs have a lower luminosity and have a larger minimum radius than GRBs, the photosphere is close to where the jet is launched. Since the TDE creates the accretion disk that feeds the super-massive black hole, the total energy budget of Sw J1644 is well constrained at $\sim 1 M_{\odot}$.

In this paper, we comprehensively considered emission mechanisms for the Swift XRT-BAT radiation observed in the tidal disruption event Sw J1644+57. We found that we can robustly rule out internal inverse Compton models for the Sw J1644+57. Internal inverse Compton cannot explain the Sw J1644+57 spectrum because inverse Compton cooling from the X-ray photons will cause too much flux in the infrared band.

We developed a new way to calculate the synchrotron radiation from shocks that accounts for Klein-Nishina effects, self-consistently calculates the synchrotron self-absorption frequency when $\nu_c < \nu_a$, and is applicable to non power-law electron distributions. We find the synchrotron model with a single episode of acceleration of particle has difficulties satisfying all observational constraints. There does exists a small area at small radii ($R \lesssim 2 \times 10^{13}$ cm) where synchrotron self-absorption can prevent the K-band from being overproduced by cooled electrons. Since the emission is in the fast cooling regime, the required electron index is quite hard ~ 1.6 at early times and ~ 0.8 at late times. Since such a hard electron index will be difficult to achieve in any Fermi process and the allowed parameter space is quite small, synchrotron radiation produced in shocks is an unlikely source of the X-rays of Sw J1644+57.

We found that proton synchrotron model for the X-ray emission of Sw J1644+57 may be able to explain the observed spectrum, if the jet is Poynting dominated. The proton synchrotron model requires a large minimum proton Lorentz factor $\gtrsim 10^4$, which requires a magnetization parameter $\sigma \gtrsim 10^4$. The proton model also has a relatively low radiative efficiency of $\sim 1\%$

We also considered external inverse Compton of UV radiation from the accretion disk wind by the relativistic jet. We find that the EIC model is marginally consistent with the observations if the scattering happens above the photosphere, the efficiency in launching the wind is large, and the Lorentz factor of the jet is not too large, $\Gamma \lesssim 5$. Matching the observed spectrum requires hot, non-thermal electrons in jet. These hot electrons will be cooled rapidly through inverse Compton scattering the observed X-rays. To match the observed spectrum, the external inverse Compton process requires either a hard electron index or continually reheated electrons. How energy is dissipated to heat the electrons is unknown and beyond the scope of the paper. At late times, the inverse Compton cooling rate decreases significantly, $\propto L_X$, and the temperature of the wind increases. These two effects may be able to explain the observed hardening of the X-ray spectrum without two values of p.

Photospheric models, where a thermal spectrum is reprocessed through inverse Compton scattering by hot electrons, face severe difficulties in reproducing the observed spectrum of Sw J1644+57. The main problems is due to the fact that the hot electrons that are scattering photons lose too much of their energy before they are able to populate a hard spectrum, such as the one observed in Sw J1644+57. It may be possible to match the spectrum if there are many ($\gtrsim 175$) reheating events just below the photosphere in Sw J1644+57.

Finally we considered magnetic reconnection in a Poynting-dominated jet. We find that the luminosity and the spectrum can be easily matched with a model of magnetic reconnection based off of very general principles for a large swath of the available parameter space. The magnetization of the jet is large $\sigma \sim 250 - 2800$. The emission is dominated by electrons inside of reconnection regions where the electrons are unable to cool. Outside of the reconnection region, they cool very quickly through synchrotron radiation. But because the number of electrons that radiate at 1 keV is much higher inside of the reconnection region, the cooled electrons will not cause an infrared excess. We feel that a Poynting-dominated jet with magnetic reconnection is the most likely model for the X-rays observed in Sw J1644+57.

Chapter 4

Radio-synchrotron Emission from the Extended Object at the Galactic Center, G2

Chapter Précis

The radio flux from the synchrotron emission of electrons accelerated in the forward bow shock of G2 is expected to peak when the forward shock passes pericenter, possibly 7-9 months before the center of mass of G2 reaches pericentre $\sim 3 \times 10^{15}$ cm from the Galactic Center. We calculate the radio emission from the forward and reverse shock if G2 is a momentum-supported bow shock of a faint star with a high mass-loss rate as suggested by Scoville & Burkert (2013). We show that the radio flux lies well below the quiescent radio flux of Sgr A and will be difficult to detect. By contrast, in the cloud model of G2, the radio flux of the forward shock is predicted to be much larger than the quiescent radio flux and therefore should have already been detected. Therefore, radio measurements can reveal the nature of G2 well before G2 completes its periapsis passage.

4.1 Introduction

G2, a recently discovered spatially-extended red source, is on a nearly radial orbit headed towards the $M \sim 4.31 \times 10^6\ M_\odot$ ($R_s = 2GM/c^2 \sim 1.27 \times$

[†] This chapter has been previously published as Crumley & Kumar (2013b)

10^{12} cm), supermassive black hole at the Galactic center, Sgr A* (Gillessen et al., 2012). As G2 plunges towards Sgr A* at a supersonic speed, it will drive a bow shock into the hot interstellar medium (ISM). As electrons cross the forward shock, they will be accelerated and emit synchrotron radiation. The radio synchrotron emission from the forward shock has been predicted to be observable by Narayan et al. (2012a); Sądowski et al. (2013b). Sądowski et al. (2013a) predicted that the radio emission should peak 7 to 9 months before the center of mass crosses periapsis in spring of 2014, reaching a distance of a mere $\sim 3 \times 10^{15}$ cm ($\sim 2400 R_s$) away from Sgr A* (Phifer et al., 2013; Gillessen et al., 2013b). G2's close encounter may give a unique opportunity to probe the accretion disk of Sgr A* and the ISM near periapsis by measuring the radio flux of the forward bow shock. The radio flux from the forward shock has yet to be observed; depending on the orbital parameters of G2, it may not be expected to peak until late summer or early autumn of 2013, although perhaps $\sim 10\%$ of G2 has already passed periapsis (Gillessen et al., 2013b). In this letter, we show that the expected radio flux from the forward shock is model dependent, suggesting an intriguing possibility: the radio flux from the forward shock may reveal the nature of G2.

The nature of G2 is undetermined. When first discovered, Gillessen et al. (2012, 2013a) hypothesized that G2 was a pressure-confined, non-self-gravitating gas cloud, due to the fact that the Brackett-gamma (Br-γ) luminosity of G2 is not changing with time, $L_{\mathrm{Br}\gamma} \sim 2 \times 10^{-3} L_{\odot}$, and the Br-$\gamma$ velocity dispersion is increasing in a manner that is well fit by a gas cloud with a radius of $\sim 2 \times 10^{15}$ cm being tidally sheared by Sgr A*. The compactness of G2 necessitates that this gas cloud must have formed shortly before G2 was first discovered in 2002. However, there is not a clear source of a gas cloud in the region as the ISM at a distance $\sim 5 \times 10^{16}$ cm from Sgr A* is not susceptible to thermal instabilities. One possible source of a gas cloud is colliding stellar winds (Burkert et al., 2012; Schartmann et al., 2012). Alternatively, there is another class of models where G2 contains a very faint stellar core that emits gas as it falls towards Sgr A* (Scoville & Burkert, 2013; Ballone et al., 2013). The ionized gas is then tidally sheared and is the source of the Br-γ radiation seen as G2. In Scoville & Burkert (2013), the ionized gas that is the source of the Br-γ radiation is located in the cold dense inner shock of a momentum-supported bow shock between a stellar wind from a hidden, young star and the hot ISM. Ballone et al. (2013) performed hydrodynamical simulations in which they evolved the stellar wind shock in the gravitational potential of Sgr A*, and they found that the v_{lsr} dispersion observations are well-matched by a star with a mass-loss rate of $\dot{M} = 8.8 \times 10^{-8} M_{\odot}/\mathrm{yr}$ and with a wind speed of 50 km/s. The ionization source of the inner shock in this model is not entirely clear, as the predicted Br-γ radiation does not perfectly match the observations. Scoville & Burkert (2013) proposed that hydrogen is collisionally ionized in the inner shock of the stellar wind, although they overestimated the ionization ability of the wind and underestimated the ionizing background from the O stars in the galactic center. Ballone et al. (2013) just assumed the entire inner shock was ionized, which leads to the Br-γ flux increasing as G2 approaches pericenter, which is not what has been observed. Future work will need to be done to understand the radiation mechanism in the stellar wind model of G2.

If G2 is a pressure-confined diffuse cloud, then it will likely be destroyed during periapsis passage. If G2 is the inner bow shock of a star it will likely survive (Gillessen et al., 2012; Anninos et al., 2012; Schartmann et al., 2012;

Scoville & Burkert, 2013). Additionally, if G2 is a cloud, how its size changes as it approaches Sgr A* is not clear while the stellar wind model of G2 makes a strong prediction about how the size of the forward bow shock evolves as G2 passes through periapsis.

In the cloud model, as G2 heads closer to Sgr A* it will be stretched in the longitudinal direction, compressed in the transverse direction by tidal forces, and compressed further by the increasing pressure of the ISM. In the 3-D simulation by Anninos et al. (2012), for an isothermal cloud that formed in 1995.5 with a radius of 1.875×10^{15} cm, they find that the cross sectional area of G2 one year before periapsis shrunk by a factor of 4 to $\sim \pi \times 10^{30}\text{cm}^2$. It appears to be the same size at periapsis. The cloud is in the process of being completely disrupted, so it is difficult to tell.

In this letter, we use the term "cloud model" to mean a model where the cross section of G2 is approximately constant as it passes through periapsis as in Narayan et al. (2012a); Sądowski et al. (2013b). In the stellar wind model, far away from Sgr A* the size of the shock is approximately the same as in the cloud model, but when G2 gets close to periapsis, its size shrinks significantly, inversely proportional to the increase of the pressure of the ISM. In other words, the area is proportional to the distance from Sgr A* squared (see eq 4.7). The hydrodynamic simulations in Ballone et al. (2013) show a similar decrease to the shocked wind area. The decrease in area at periapsis drastically reduces the expected radio flux.

G2 appears to be an extended object with the compact head structure called G2, and a less dense and larger tail-like structure, G2t (Gillessen et al., 2013b). This paper focuses solely on the over-dense head, G2, as the origin of G2t is not well known. If G2 is a diffuse cloud then G2t is either material that was stripped from G2 as it fell towards Sgr A*, or it was somehow formed through a similar process as G2. If G2 has a stellar core emitting a wind, the tail may have been from the outflow of the star when it was closer to apocenter.

In this letter, we extend the work of Narayan et al. (2012a); Sądowski et al. (2013b) to the stellar wind model of G2. We apply Wilkin (1996) analytic solution of the momentum-supported bow shock model proposed by Baranov et al. (1971) to estimate the size of the bow shock of G2. Analytical calculations are better suited to estimate the forward shock size than a hydrodynamic simulation such as Ballone et al. (2013) because of stability issues in the simulation. The ISM surrounding Sgr A* is convectively unstable. Previous simulations (with the exception of Sądowski et al., 2013a) dealt with this issue by evolving a passive tracer field along with G2 and resetting the ISM to its equilibrium value whenever a cell did not have a sufficient ratio of tracer particles to ISM particles (Anninos et al., 2012; Schartmann et al., 2012). As noted in Ballone et al. (2013), this stabilization technique suppresses the forward shock in the ISM, making these simulations incapable of properly resolving the forward shock. Analytical calculations also allow us to predict how the radio flux depends on the undetermined parameters of the stellar wind.

We use the geometry of the bow shock to calculate the expected synchrotron flux in the radio band of both the outer forward shock and the inner termination shock for the stellar wind model of G2. The predicted flux of the forward shock is roughly two orders of magnitude less than the flux predicted by Sądowski et al. (2013b), and lies an order of magnitude below the quiescent radio emission of Sgr A* at 2 GHz. If the stellar wind model is correct, G2 will likely not be observable in radio frequencies. Therefore, a radio detection of G2 will shed light on the nature of G2 well before periapsis passage.

In section 4.2 of this letter, we briefly describe the model we used for the ISM at the Galactic Center as well as the geometry of the bow shock. In section 4.3 we show how the expected peak synchrotron flux at 1.4 GHz and spectrum depend on the nature of G2. In section 4.4 we extend our results to the star S2. Finally, in section 4.5 we briefly discuss our findings.

4.2 Methodology

4.2.1 Environment at the Galactic Center

For the hot ISM environment surrounding Sgr A*, we adopt the same dependence of density and temperature on distance d from Sgr A* as those used by Schartmann et al. (2012), who used the model of Yuan et al. (2003). However, the most recent *Chandra* X-ray observations of the Galactic Centre suggest that the radial density profile may be flatter than the one used by Schartmann et al. (2012). (Wang et al., 2013)

$$n_{\rm ISM} = 930\ {\rm cm}^{-3} \left(\frac{1.4\times10^4 R_s}{d}\right) = 1660\ d_{16}^{-1}\ {\rm cm}^{-3} \tag{4.1}$$

$$T_{\rm ISM} = 1.2\times10^8\ {\rm K} \left(\frac{1.4\times10^4 R_s}{d}\right) = 2.1\times10^8 d_{16}^{-1}\ {\rm K} \tag{4.2}$$

Throughout this paper the convention $Q_x \equiv \frac{Q}{10^x}$ is used, and unless otherwise noted all units are cgs. To calculate the distance and velocity of G2, we use the orbital parameters derived from the Br-γ observations given in Gillessen et al. (2013b). However, for the purposes of illustration G2's velocity is well matched by a free fall approximation, *i.e.* $v_* \approx \sqrt{2GM/d} = 3.4\times10^8 d_{16}^{-0.5}$ cm/s. The Mach number is approximately $\mathcal{M}_* \approx 2$. Because of the approximation we made to the velocity, the Mach number has no time dependence, but it will change with time when using the proper elliptical motion of the orbit.

4.2.2 Geometry of the Bow Shock

To calculate the radio flux from the forward bow shock of G2, we need to determine the area of its cylindrical cross section. We use the same parameters for the isothermal stellar wind as in Ballone et al. (2013): a star with a mass-loss rate of $\dot{M}_* = 8.8\times10^{-8} M_\odot/\mathrm{yr}$, a constant wind speed of $v_w = 50$ km/s, and a temperature of $T_w = 10^4$ K. We include the dependence of our results on the stellar wind parameters as they are not precisely constrained by observations. The wind is supersonic, with a Mach number of $\mathcal{M}_w = 4.26\, T_4^{-0.5}(v_w/50\ \mathrm{km/s})$. To calculate the properties of a stellar wind bow shock, we used the equations given in Baranov et al. (1971) instead of Dyson (1975) because Baranov et al. (1971) correctly accounts for the centrifugal force due to the fluid moving in a curved path inside of the shock. The effect of the centrifugal force is to produce a larger bow shock, *e.g.* Baranov et al. (1971), than the solution given in Dyson (1975) (see figure 4.1 for a comparison). The stagnation radius, r_0, is the same in both solutions and it occurs where the two ram pressures equal one another, *i.e.* $\rho_w v_w^2 = \rho_{\mathrm{ISM}} v_*^2$. For the adopted parameters of $\dot{M}_*$ and v_w,

$$r_0 = \sqrt{\frac{\dot{M}_* v_w}{4\pi m_p n_{\mathrm{ISM}} v_*^2}} \approx 8\times10^{13}\ d_{16}\left(\tfrac{\dot{M}_* v_w}{2.8\times10^{25}\ \mathrm{dyn}}\right)^{0.5}\ \mathrm{cm} \tag{4.3}$$

The shock is axisymmetric about the stellar velocity vector, and the distance of the bow-shock surface from the star depends on the azimuthal angle measured from the stagnation point, φ, and can be written as $r(\varphi) = \xi(\varphi) r_0$ where ξ is given as an analytical function in Wilkin (1996),

$$\xi(\varphi) = \csc(\varphi)\sqrt{3\,(1-\varphi\cot\varphi)} \tag{4.4}$$

The velocity of the gas inside of the bow shock is tangential to the shock surface and equal to

$$v_l = v_w \frac{\sqrt{(\varphi - \sin\varphi\cos\varphi)^2 + (3(1-\varphi\cot\varphi) - \sin^2\varphi)^2}}{2(1-\cos\varphi) + 3v_w(1-\varphi\cot\varphi)/v_*} \tag{4.5}$$

The strength of the outer shock depends on the angle φ. The shock will terminate at an angle, $\varphi_{\max}$, where the normal component of the velocity of the ISM with respect to the star, v_{*n}, is equal to the sound speed of the ISM. As in Baranov et al. (1971), it is useful to define the following angles: $y = \arctan(\mathrm{d}\ln\xi/\mathrm{d}\varphi)$, and $x = y + \pi/2 - \varphi$, so that $v_{*n} = v_* \sin x$. Then $\varphi_{\max}$ is found by solving $\mathcal{M}_* \sin x = 1$. When $\mathcal{M}_* = 2$, $\varphi_{\max} \approx 106°$ and $\xi_{\max} \equiv \xi(\varphi_{\max}) \approx 2.2$. The cylindrical cross-section area of the forward shock is

$$\begin{aligned} A &= \pi r_0^2 \xi_{\max}^2 \sin^2\varphi_{\max} && (4.6)\\ &\sim 10^{29}\, d_{16}^2 \left(\frac{\dot{M}_* v_w}{2.8\times10^{25}\ \mathrm{dyn}}\right)\ \mathrm{cm}^2. && (4.7)\end{aligned}$$

$\mathcal{M}_*$ has some degree of uncertainty from modeling the Galactic Center, and the fact that the inclination of G2's trajectory with respect to a possible accretion disk of Sgr A* is unknown. The change in the area can be estimated using $\xi_{\max}^2 \sin^2\varphi_{\max} \approx 3.5\mathcal{M}_* - 2.4$, when $\mathcal{M}_* \geq 1.5$. The cross-sectional area versus time is plotted in figure 4.1. The area in the wind models decreases by ~ 2 orders of magnitude as G2 approaches periapsis. Synchrotron flux is expected to peak at periapsis where the magnetic field is strongest. The decrease in the area of the forward shock as G2 approaches periapsis is responsible for the

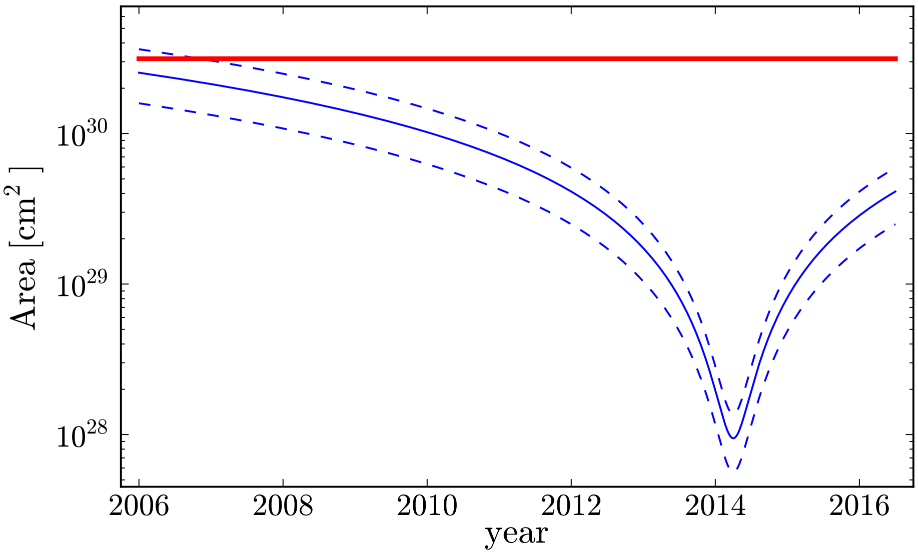

Figure 4.1: The cross section area of the forward shock as G2 approaches periapsis. The solid blue line is the cross sectional area of the forward shock calculated in a bow shock correcting for the centrifugal force. The lower dashed blue line is the size of the forward shock if using the bow shock model of Dyson (1975) as did Scoville & Burkert (2013). The upper dashed blue line is $\pi \times \dot{M} v_w/(4\pi nkT)$, the cross-sectional area of the inner shock of G2, which agrees very well with the simulation by Ballone et al. (2013). The thick red line is the area used in Sądowski et al. (2013b), $\pi \times 10^{30}$ cm.

large difference in flux for the pressure-confined cloud and stellar wind models.

4.3 Results

4.3.1 Radio Flux of Forward Shock

To calculate the expected synchrotron emission of the forward shock of G2 we extend the methodology of Sądowski et al. (2013b) to the stellar wind model of G2, who used particle-in-cell simulations of low Mach number shocks to estimate the electron population accelerated by G2. As in Sądowski et al. (2013b), we assume that a fraction $\eta \sim 5\%$ of the electrons swept into the forward shock are accelerated to a high-energy power law spectrum with a slope of $p = 2.4$ and that has a minimum Lorentz factor $\gamma - 1 = \zeta kT/m_e c^2$, where $\zeta = 7.5$ and T is the preshock temperature. η and ζ were empirically determined by Sądowski et al. (2013b) with simulations. They found η and ζ to be nearly independent of T and $\mathcal{M}_*$. It may be counter-intuitive that the injection energy of the power law spectrum depends on the preshocked rather than shocked temperature, but because of the very narrow range of $\mathcal{M}_*$ applicable to G2 and considered by Sądowski et al. (2013b), *i.e.* $1.5 \leq \mathcal{M}_* \lesssim 3.5$, it makes little difference which temperature one chooses (as long as ζ is adjusted accordingly).

The energy distribution of the rate at which electrons enter the shock is given by (Sądowski et al., 2013b),

$$\frac{\mathrm{d}N}{\mathrm{d}\gamma \mathrm{d}t} = \eta A v_* n \frac{(p-1)(\zeta kT/m_e c^2)^{p-1}}{(\gamma - 1)^p} \tag{4.8}$$

for $\gamma - 1 > \zeta kT/m_e c^2$, and where A, v_*, n, and T are all functions of time. To calculate the expected radio flux, we assume that $P_{\mathrm{mag}} = \chi P_{\mathrm{gas}}$, where P_{gas} is the pressure of the unshocked ISM to calculate the unshocked magnetic field. The shocked magnetic field is calculated assuming only shock compression with no additional amplification of the magnetic field, as expected for small Mach number shocks. We use the Rankine-Hugoniot jump conditions of an adiabatic shock to find the shocked magnetic field from (Narayan et al., 2012a),

$$B \approx 0.01\ \chi_{-1}^{0.5} d_{16}^{-1}\ \mathrm{G} \tag{4.9}$$

$$B' \approx \frac{(\hat{\gamma}+1)\mathcal{M}_*^2}{(\hat{\gamma}-1)\mathcal{M}_*^2 + 2} B \sim 0.02\ \chi_{-1}^{0.5} d_{16}^{-1} \mathrm{G}, \tag{4.10}$$

when $\mathcal{M}_* \approx 2$, $\hat{\gamma} = 5/3$. As an upper limit on B', we make sure that the shocked magnetic pressure does not exceed the ram pressure of the ISM, which is true for all Mach numbers if $\chi \leq m_p v_*^2/(16kT) \sim 0.4$. We take $\chi = 0.3$, which corresponds to the trajectory with largest flux at 1.4 GHz in Sądowski et al. (2013b). The synchrotron specific luminosity at the frequency ν is

$$P_\nu(t) = \tfrac{\sqrt{3}q^3CB}{m_ec^2(p+1)}\Gamma\left(\tfrac{p}{4}+\tfrac{19}{12}\right)\Gamma\left(\tfrac{p}{4}-\tfrac{1}{12}\right)\left(\tfrac{2\pi m_e c\nu}{3qB}\right)^{-\frac{p-1}{2}} \tag{4.11}$$

where C is the number of electrons with $\gamma \geq 2$ at time t. The observed flux is calculated using a distance to the Galactic Center of $d_{A*} = 8.33$ kpc:

$$F_\nu(t) = \frac{P_\nu(t)}{4\pi d_{\mathrm{A}*}^2} \approx 5\frac{C_{45}B}{(p+1)}\left(\frac{2\pi m_e c\nu}{3qB}\right)^{-\frac{p-1}{2}} \ \text{Jy/G} \tag{4.12}$$

To calculate the flux, we extend the two scenarios defined in Sądowski et al. (2013b) to a bow shock with changing area which starts accelerating electrons at sometime t_i and the forward shock reaches periapsis at t_0. The two models are (1) the plow model, where every electron that enters the shock stays in the shocked area and radiates in the shocked magnetic field, and (2) the local model, where the electrons are energized by the shock but then they quickly exit the shock and radiate *in situ* in the unshocked local magnetic field.

In the plow model, the flux at 1.4 GHz is calculated from eq (4.12) using the area from eq (4.6) and the shocked magnetic field, eq (4.10). When $t \leq t_0$, C_{plow} is

$$C_{\mathrm{plow}}(t) = \eta A(p-1)\textstyle\int_{t_i}^{t} v_* n\left(\tfrac{\zeta kT}{m_ec^2}\right)^{p-1}\,\mathrm{d}t, \tag{4.13}$$

where A is the instantaneous bow shock area at time t. When $t > t_0$, C_{plow} is

$$C_{\mathrm{plow}}(t) = C_{\mathrm{plow}}(t_0) + \eta(p-1)\textstyle\int_{t_0}^{t} A v_* n\left(\tfrac{\zeta kT}{m_ec^2}\right)^{p-1}\,\mathrm{d}t \tag{4.14}$$

In the local model, the flux is calculated with the unshocked magnetic field

$$F_{\mathrm{local}} = \frac{5 \times 10^{-45}}{p+1} \int_{t_i}^{t} B \left(\frac{2\pi m_e c \nu}{3qB} \right)^{-\frac{p-1}{2}} \left. \frac{\mathrm{d}N}{\mathrm{d}\gamma \mathrm{d}t} \right|_{\gamma=2} \mathrm{d}t \tag{4.15}$$

The light curves of the flux at 1.4 GHz in the stellar wind model of G2 are shown near pericenter passage of the forward shock in the inset of figure 4.2. The light curves in the stellar wind model peak shortly after t_0 as in the cloud model of Sądowski et al. (2013b). To compare the expected fluxes from the stellar wind and cloud models, we also calculate the expected flux using a constant area of $A = \pi \times 10^{30}$ cm^2 in equations (4.13) and (4.15). The light curves close to pericenter of both the cloud and stellar wind models are plotted in figure 4.2.

To see how our results depend on our parameter choices, we estimate C in both the plow and local models by multiplying $\left.\frac{\mathrm{d}N}{\mathrm{d}\gamma \mathrm{d}t}\right|_{\gamma=2}$ by the dynamical time ($\sim d/v_*$) and using the area from eq (4.7).

$$\begin{aligned} C &\sim \eta A (p-1) n d (\zeta k T / m_e c^2)^{p-1} &(4.16)\\ &\sim 2 \times 10^{46} d_{16}^{0.6} \left(\frac{\dot{M}_* v_w}{2.8 \times 10^{25}\ \mathrm{dyn}} \right) &(4.17)\end{aligned}$$

Then the flux at 1.4 GHz when $t \leq t_0$ is estimated using eq (4.12) with magnetic fields from eq (4.9) and (4.10) for the local and plow model respectively

$$F_{\rm local} \sim 0.6 \left(\frac{\chi}{.3}\right)^{0.85} d_{16}^{-1.1} \left(\frac{\dot{M}_* v_w}{2.8\times10^{25}\ \rm dyn}\right) \ {\rm mJy} \tag{4.18}$$

$$\sim 3\ {\rm mJy} \quad {\rm at} \quad t = t_0 \tag{4.19}$$

$$F_{\rm plow} \sim 4 \left(\frac{\chi}{.3}\right)^{0.85} d_{16}^{-1.1} \left(\frac{\dot{M}_* v_w}{2.8\times10^{25}\ \rm dyn}\right) \ {\rm mJy} \tag{4.20}$$

$$\sim 13\ {\rm mJy} \quad {\rm at} \quad t = t_0 \tag{4.21}$$

The analytical results given by equations (4.18) and (4.20) are found to be within a factor of 2 from the numerical results in figure 4.2.

4.3.2 Radio Flux of Inner Shock

In the stellar wind model of G2, electrons will be accelerated at both the outer, forward shock traveling into the ISM as well as at the inner, termination shock of the stellar wind. For the inner shock to radiate at 1.4 GHz, it must be able to accelerate electrons from a upstream temperature of ~ 1 eV to $\sim 3\times10^7$ eV. It is not clear whether a non-relativistic shock with $\mathcal{M}_w \approx 4$ will be capable of accelerating high energy electrons efficiently. Therefore, our estimation of the radio flux from the inner shock in this section should be taken as an upper limit. We find the flux at 1.4 GHz lies four orders of magnitude below the fluxes calculated in the previous section. Therefore the inner shock will not contribute to the radio synchrotron flux of G2.

The stellar wind at the bow shock is much more dense than the ISM, its density equal to

$$n_w(r_0) = \frac{n_{\rm ISM} v_*^2}{v_w^2} \approx 8\times10^6\ d_{16}^{-2} \left(\frac{50\ \rm km/s}{v_w}\right)^2\ {\rm cm}^{-3} \tag{4.22}$$

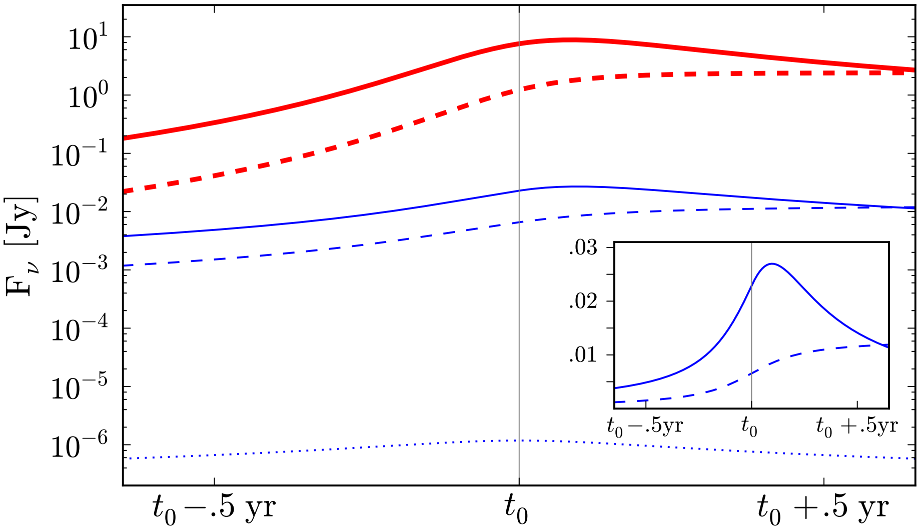

Figure 4.2: The expected synchrotron flux at 1.4 GHz around pericenter passage of the forward shock, t_0, for different models of G2. Solid lines correspond to the plow model, where all of the accelerated electrons stay inside of the shock. The dashed lines correspond to the local model, where the electrons quickly leave the bow shock region after being accelerated. Thick red lines correspond to when G2 is a cloud with an area of $\pi \times 10^{30}$ cm^2 as in Narayan et al. (2012a); Sądowski et al. (2013b). The lower blue lines represent when G2 is a stellar wind with an area calculated using eq (4.6). The dotted blue line is the flux from electrons residing in the inner shock of the stellar wind assuming a steady state solution. *Inset*: A plot showing the flux at 1.4 GHz in Jy for a stellar wind model of G2 in a linear scale.

The shocked gas will radiate efficiently and cool quickly, and therefore the shock can be taken to be isothermal. So n_w will be boosted by a factor $\mathcal{M}_w^2$:

$$n'_w(r_0) = \mathcal{M}_w^2 n_w(r_0) \approx 1.4 \times 10^8\ d_{16}^{-2} T_{w,4}^{-1}\ \mathrm{cm}^{-3} \tag{4.23}$$

Assuming that in the shocked wind $P'_{\rm mag} = \chi'_w P'_{\rm wind}$, $\chi'_w \leq 1$, the magnetic field inside of the inner shock is

$$B'_{\rm in} = \sqrt{8\pi\chi'_w n'_w(r_0) k T_w} \approx 0.07\ \chi_w'^{0.5} d_{16}^{-1}\ \mathrm{G} \tag{4.24}$$

We calculate the volume of the inner shock by assuming that it is in steady state. In a steady state, the thickness of the shock, t_l, is found by numerically solving the continuity equation for t_l as a function of φ,

$$2\pi r_0 \xi t_l v_l n'_w \sin\varphi \approx 2\pi n_w r_0^2 \xi^2 v_w (1 - \cos\varphi). \tag{4.25}$$

t_l is estimated as being constant in φ and equal to $t_l \sim r_0/\mathcal{M}_w^2$:

$$t_l \sim 4 \times 10^{12} d_{16} T_{w,4} \left(\tfrac{\dot{M}/(M_\odot/\mathrm{yr})}{8.8\times10^{-8}}\right)^{0.5} \left(\tfrac{50\ \mathrm{km/s}}{v_w}\right)^{1.5}\ \mathrm{cm} \tag{4.26}$$

We calculate the volume of the inner shock, $V_{\rm in}$, accounting for the geometry of the bow shock and solving eq (4.25) for t_l. Approximately, $V_{\rm in} \sim 4\pi r_0^2 t_l$. Using $V_{\rm in}$ we calculate $C_{\rm in}$, the number of electrons in the inner shock with $\gamma \geq 2$:

$$C_{\rm in} = \eta V_{\rm in} n'_w (p-1)(\zeta k T_w/m_e c^2)^{p-1} \tag{4.27}$$

$$\sim 5 \times 10^{41} d_{16} T_{w,4}^{1.4} \left(\tfrac{\dot{M}/(M_\odot/\mathrm{yr})}{8.8\times10^{-8}}\right)^{1.5} \left(\tfrac{50\ \mathrm{km/s}}{v_w}\right)^{0.5} \tag{4.28}$$

The flux is estimated using eq (4.12):

$$F_\nu \sim 2 \times 10^{-7} d_{16}^{-0.7} \chi_w'^{0.85} T_{w,4}^{1.4} \tag{4.29}$$

$$\times \left(\frac{\dot{M}/(M_\odot/\mathrm{yr})}{8.8 \times 10^{-8}}\right)^{1.5} \left(\frac{50\ \mathrm{km/s}}{v_w}\right)^{0.5}\ \mathrm{Jy} \tag{4.30}$$

$$\sim 0.5\ \mu\mathrm{Jy} \quad \text{at} \quad t = t_0 \tag{4.31}$$

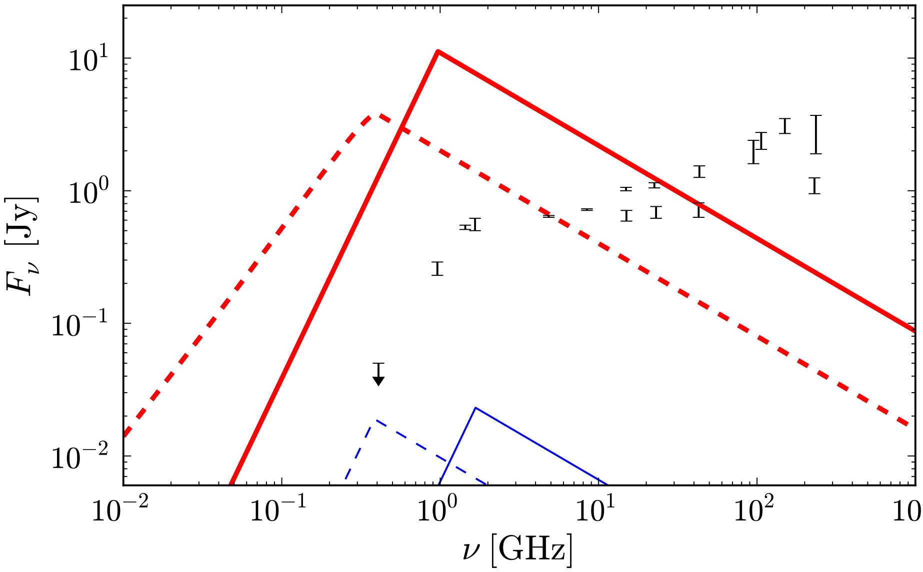

Figure 4.3: Spectra at a time $t_0 + 0.05$ yr, where t_0 is the periapsis crossing time of the forward shock. The color scheme is the same as figure 4.2, where solid lines correspond to the plow model, and dashed lines to the local model. Thick red lines represent the spectra if G2 is a cloud, while the lower blue lines are if G2 is a stellar wind. The data points are radio fluxes measured during periods of inactivity of Sgr A* by Davies et al. (1976); Falcke et al. (1998); Zhao et al. (2003).

Using eq (4.27), (4.24), (4.11) and (4.12), we calculate the expected radio flux for the inner shock at 1.4 GHz, and plot it in figure 4.2. Our estimate underpredicts the more accurate calculation of the inner shock radio flux at periapsis by a factor $\lesssim 2$. The radio flux from the inner shock lies well below the forward shock and can be ignored.

4.3.3 Spectra

In figure 4.3 we show the spectra expected from forward shock at 0.05 years after periapsis of the forward shock. To calculate the synchrotron self absorption frequency in the plowing models, we simply use the surface area of the forward shock at time $t_0 + 0.05$ years, accounting for the geometry of the bow shock in the stellar wind model. In the local models, we use the same approach as Sądowski et al. (2013b), where synchrotron self absorption frequency and F_ν are calculated separately for each time step Δt up until $t_0 + 0.05$ yr, and then the fluxes are summed. The surface area of the radiation in the local model is $2\pi r v_* \Delta t$, where $r = 10^{15}$ cm in the cloud model and is $r_0 \xi_{\max} \sin\varphi_{\max}$ in the stellar wind model. The radio flux in the stellar wind model lies below the quiescent flux of Sgr A* at all frequencies and therefore will likely not be observable.

4.4 Application to the Star S2

There is a cluster of young stars at the galactic center, and one of the brightest of these stars S2, a B type star that has an orbital period of 15.5 years, reaches nearly twice as close to Sgr A* as G2 (a distance of $\sim 1.8 \times 10^{15}$ cm) (Gillessen et al., 2009). S2 is expected to have a strong wind which will form a momentum-supported bow shock similar to G2 in the stellar wind model. The X-ray radiation from the inner shock was investigated by Giannios & Sironi (2013), who estimated the S2's wind has a mass-loss rate $\dot{M} \sim 10^{-7} \dot{M}_\odot$/yr and a velocity ~ 1000 km/s. Using these parameters, we estimate peak radio flux at periapsis from the electrons accelerated by the outer shock of S2 using eq (4.20). We estimate that the peak flux from the forward shock of S2 at 1.4 GHz is $\sim .5$ Jy and $\sim .1$ Jy at 14 GHz (assuming $p = 2.4$). The last pericenter crossing of S2 was in 2002.3 and there is good data of Sgr A* around this time. The flux at 15 GHz varies from ∼0.8–1.1 Jy and the flux at 23 GHz varies from ∼0.8–1.2 Jy (Herrnstein et al., 2004). While there is variability in the radio flux before and after the pericenter crossing of S2, there is not a flare that lasts for a long time or is spectrally consistent with synchrotron radiation from S2. Throughout the pericenter crossing time the flux at 23 GHz is equal to or larger than the flux at 15 GHz, while the opposite would be expected from the synchrotron radiation of an electron power-law distribution with $p = 2.4$. Thus it is likely this variation is due to intrinsic variation of Sgr A* and not due to S2. The lack of detection of the forward shock of S2 in 2002.3 gives us additional confidence in our prediction that the forward-shock of G2 will not be observable in the radio band.

4.5 Conclusions

In this paper we calculated the expected radio flux from the forward shock and reverse shock of G2 assuming that G2 is the inner bow shock of a stellar wind as suggested by Scoville & Burkert (2013); Ballone et al. (2013). We used an analytic solution of a momentum-supported bow shock to calculate the geometry of the forward shock and provide analytical estimates of the flux at 1.4 GHz at pericenter passage of the forward and reverse shock to show how the flux depends on the undetermined parameters of the stellar wind. If G2 is the inner shock of a stellar wind, its forward shock cylindrical cross section will decrease as G2 approaches Sgr A* and the ram pressure increases, driving the stagnation point to a smaller distance from the star. The decrease in area by over two orders of magnitude of results in a similar decrease in the radio flux expected at periapsis, falling well below the previous estimates of ∼1-20

Jy predicted by Narayan et al. (2012a); Sądowski et al. (2013b), where they assumed that G2 was a gas cloud that formed in pressure equilibrium and that the cross section area stayed constant. If G2 is the inner bow shock from a stellar wind, the radio flux from the forward shock lies below the quiescent radio emission of Sgr A* at all frequencies, so it will be difficult to detect.

If G2 is a pressure-supported gas cloud, it will likely be destroyed during pericenter passage; on the other hand G2 will survive if it is the inner bow shock of a stellar wind. Therefore whether or not G2 survives will be important in determining the makeup of G2. However, the radio emission will peak when the forward shock crosses periapsis, which in the cloud model is predicted to happen 7 to 9 months before G2 passes through periapsis. We have shown that the stellar wind model makes a very different prediction of the radio synchrotron flux of G2, so the radio flux will be an important early clue about the nature of G2.

Chapter 5

Hadronic Models of Gamma-ray Bursts

Chapter Précis

This chapter examines the possibility that hadronic processes produce the $\gtrsim$100 MeV photons in the prompt phase of gamma-ray bursts (GRBs) observed by the Fermi-Large Area Telescope (LAT). We calculate analytically the radiation from protons and from secondary electronpositron pairs produced by high-energy protons interacting with γ-rays inside of the GRB jet. We consider both photopion and Bethe-Heitler pair production processes to create secondary electrons and positrons that then radiate via inverse Compton and synchrotron processes. We also consider synchrotron radiation from the protons themselves. We calculate the necessary energy in protons to produce typical Fermi-LAT fluxes of a few μJy at 100 MeV. For both of the photopion and BetheHeitler processes, we find that the required energy in protons is larger than the observed γ-ray energy by a factor of a thousand or more. For the proton synchrotron model, the protons have a minimum Lorentz factor $\sim 2 \times 10^6$. This is much larger than expected if the protons are accelerated by relativistic collisionless shocks in GRBs. We also provide estimates of neutrino fluxes expected from photohadronic processes. Although the flux from a single burst is below IceCube detection limits, it may be possible to rule

---

[†] This chapter has been previously published as Crumley & Kumar (2013a)

out photohadronic models by adding up the contribution of several bursts. Therefore, photohadronic processes seem an unlikely candidate for producing the Fermi-LAT radiation during the prompt phase of GRBs.

5.1 Introduction

The *Fermi* satellite has detected 29 gamma-ray bursts (GRBs) with photons of energies $\gtrsim 100$ MeV with the Large Area Telescope (LAT) (Atwood et al., 2009) as of 2012. The photons detected during the prompt phase of GRBs by the *Fermi*-LAT are emitted with a delay of a few seconds for long GRBs, and are observed for a longer duration of time compared to the lower-energy photons ($\sim$1 MeV) observed by the *Fermi* Gamma-ray Burst Monitor (GBM) (Abdo et al., 2009b). Hadronic models could explain the delayed emission detected by the *Fermi*-LAT because of the additional time needed to energize the protons (Razzaque et al., 2010; Asano & Mészáros, 2012). Since protons do not suffer from radiative losses like electrons, it is possible that GRBs accelerate protons much more efficiently, causing the hadronic emission to dominate at high energies, (Asano et al., 2009; Murase et al., 2012). The relative efficiency of accelerating protons or electrons in GRBs depends on the mechanism that accelerates the particles. Two likely mechanisms for particle acceleration in GRBs are shock acceleration (*e.g.*, Bell, 1978; Blandford & Ostriker, 1978; Blandford & Eichler, 1987) or magnetic dissipation (*e.g.*, Usov, 1992; Drenkhahn & Spruit, 2002; Lyutikov & Blandford, 2003; Lyutikov, 2006). In this work, instead of dealing with the detailed specifics of particle acceleration for realistic GRB jet models, we assume that high energy protons exist as a power-law distribution and calculate the energy required in protons to reproduce the high-energy photon flux observed in the LAT band during the prompt phase.

There is a growing body of evidence that the observed emission in the LAT band after the prompt phase may be due to synchrotron radiation from the early afterglow emission, where electrons from the medium surrounding the GRB are accelerated by the external forward shock (Kumar & Barniol Duran, 2009; Gao et al., 2009; Corsi et al., 2010; Kumar & Barniol Duran, 2010). The most convincing evidence of external forward shock producing the $\gtrsim 100$ MeV photons is that the late time optical and X-ray afterglow data can accurately predict the earlier flux in the LAT band (Kumar & Barniol Duran, 2009). Under the external forward shock origin for the LAT emission, the delay in the LAT is due to the delayed onset of the external forward shock emission. The external-forward shock emission begins when the jet emitted by the central engine deposits half of its kinetic energy to the surrounding medium. Therefore, there remains the possibility that while the later time ($T \geq T_{90}$[1]) LAT-band flux is from the early afterglow, the earliest high energy photons observed during the prompt phase are created by a different process. The external forward shock is unable to explain the claimed variability present in the LAT prompt emission (Maxham et al., 2011). Furthermore, although the most GRB spectra can be fit with a smoothly-joined broken power law extending several decades in energy (*i.e.* the Band function, Band et al., 1993), a few bursts exhibit deviations from the simple Band function. Notably, GRBs 090902B, 090926A, and 090510 show evidence of an additional high-energy spectral component (Zhang et al., 2011; Abdo et al., 2009a; Ackermann et al., 2011). This spectral feature is usually transient and disappears before the prompt phase is over. For example, in GRB 090510, which has a T_{90} of 1.5

---

[1] T_{90} is the time at which the GRB has radiated 90% of its observed photon energy

s, it becomes statistically impossible to distinguish the additional power-law component ~ 0.8 s after the trigger (Asano et al., 2009). Similar spectral evolution was seen in GRB 090926A, where an additional power law component appears after ~ 11 s, and T_{90} is 13.6 s (Ackermann et al., 2011). These differences suggest that the high-energy prompt emission may have a different origin than the extended high-energy emission for some GRBs.

This paper is similar to Asano et al. (2009) and Asano et al. (2010) in that it addresses interactions between high-energy protons and the low-energy (GBM) photons as a possible mechanism to produced the high-energy photons observed in *Fermi*-LAT detected GRBs, but it differs in a few major ways. First, this paper investigates hadronic models of radiation—*i.e.* photo-pion production, Bethe-Heitler pair production, and proton synchrotron not only to explain the extra spectral components of the few GRB that exhibit them, but also to investigate the possibility that hadronic models are responsible for the majority of the GRB prompt emission observed in the *Fermi*-LAT. Second, instead of using Monte Carlo methods or detailed numerical codes, we use simplifying assumptions to calculate everything analytically or semi-analytically whenever feasible. Finally, the most important point of this paper is to provide analytical estimates of the energy required in protons to explain the LAT flux with hadronic emission. These estimates allow us to see how the energy requirement depends on various parameters.

The LAT and GBM detected photons are likely to have separate origins during the prompt phase because of the measured delay between them. Since we are interested in explaining the observed LAT flux of GRBs, we will assume that the < 100 MeV portion of the GRB emission is of unknown origin and perfectly described by a Band function fit with an observed peak energy of $\nu_p \sim 1$ MeV (the exact value, is of course, different for different bursts, and ν_p also evolves with time during a single burst). The Band function has a low energy index α and a high energy index β. We only consider interactions between the photons from the Band function and high-energy protons in the GRB jet. That is, we do not consider second-order processes, such as proton colliding with a pion-produced positron, et cetera. This choice greatly decreases the computational difficulty but produces results that only hold in regions where the contributions from these processes are likely small, *i.e.* above the photosphere. In two zone models, the lower energy emission is produced at a significantly smaller radius than the radius where high energy emission is produced. As Zou et al. (2011); Hascoët et al. (2012) have noted, a two zone model will reduce the minimum Lorentz factor by a factor of $\sim 2-5$ compared to the value obtained using a one zone model such as Lithwick & Sari (2001b); Abdo et al. (2009b); Greiner et al. (2009). A two zone model is unlikely to change our results by a significant factor. We provide the dependencies of the efficiency on Lorentz factor to help determine if a lower Lorentz factor could make the energy requirement more attractive.

The chapter is organized as follows: In section 5.2 we calculate the positrons produced through the photo-pion process. In section 5.2.1 we provide an analytical estimate for the required luminosity in protons to match a flux of 1 μJy at 100 MeV with the photo-pion process and provide the corresponding neutrino flux in 5.2.1.1. The required proton luminosity calculation is then repeated in section 5.2.2 however it is done numerically and more accurately. In addition, the maximum efficiency of the photo-pion process is calculated for given GRB parameters. In section 5.3, we calculate the electrons produced through Bethe-Heitler pair production and compare our result to the photo-pion calculation in §5.2.2. Section 5.4 contains a calculation of the maximum efficiency for the proton synchrotron production of typical fluxes for LAT detected GRBs, as well as an expected neutrino flux from the proton synchrotron model. Finally, in section 5.5 we summarize and discuss our results.

5.2 Photo-pion Production

The photo-pion process refers to the production of pions (π^0 and $\pi^\pm$) in collisions of photons with protons. The decay of these pions produces high energy electrons and positrons that can then produce high energy photons via synchrotron radiation. The photo-pion process is likely to be important in situations where electrons are unable to be accelerated efficiently to very high Lorentz factors, but protons are. It also offers a way to beat the well known limit on the maximum synchrotron photon energy of $\sim 50\frac{\Gamma}{1+z}$ MeV for shock-accelerated electrons, where Γ is the Lorentz factor of the source and z is the redshift (de Jager et al., 1996).

The delta resonance, $p^+ + \gamma \rightarrow \Delta^+$, has the largest cross section and has the lowest energy threshold of the photo-proton resonances and is therefore the most important photo-pion interaction to consider. The delta resonance has two main decay channels, $\Delta^+ \rightarrow \pi^+ + n$ and $\Delta^+ \rightarrow \pi^0 + p^+$. The neutral pions quickly decay further as $\pi^0 \rightarrow \gamma + \gamma$. The threshold photon energy for photo-pion production is approximately 200 MeV in the proton rest frame. The photon energy at the peak of the GRB spectrum, in jet comoving frame, is $\nu_p(1+z)/\Gamma$, where the peak frequency in the observer frame is ν_p and the GRB jet is moving with a Lorentz factor Γ. For a proton to undergo pion production with photons of energy ν_p, the proton Lorentz factor must satisfy

$$\gamma_p \gtrsim 2 \times 10^4 \Gamma_2 \nu_{p,6}^{-1} (1+z)^{-1}, \tag{5.1}$$

where $\nu_{p,6}$ is the observed peak frequency in units of 10^6 eV; the standard notation $X_n \equiv \frac{X}{10^n}$ is used. At the threshold, the π^0 is produced more or less at rest with respect to the proton. Therefore, the π^0 will decay into two photons with energies $\sim 100\ \Gamma_2^2 \nu_{p,6}^{-1} (1+z)^{-2}$ TeV in the observer rest frame, an energy is well outside the *Fermi*-LAT band. The high-energy photons created through π^0 decay will interact with the lower energy photons to produce $e^{\pm}$ pairs. If the optical depth of the $\gamma + \gamma$ pair production for 1 TeV photons is much greater than one, they will readily produce $e^{\pm}$ pairs with Lorentz factors of $\sim 10^6\ \Gamma_2 \nu_{p,6}^{-1} (1+z)^{-1}$, a similar value to the electrons produced by π^+ decay, see eq (5.2). If the optical depth of $\gamma + \gamma$ pair production is much less than one, then the photons will escape the GRB jet, and the π^0 will not affect the $\sim$ 100 MeV flux directly. However, the photons may interact with infrared background photons to create pairs which then inverse Compton (IC) scatter the cosmic microwave background photons to high energies (Dai & Lu, 2002; Razzaque et al., 2004).

The π^+ decays as $\pi^+ \rightarrow \mu^+ + \nu_\mu$, and the anti-muon decays further as $\mu^+ \rightarrow e^+ + \bar{\nu}_\mu + \nu_e$. Isospin conservation arguments suggest a branching ratio for the delta resonance for $\pi^+ : \pi^0$ of 1 : 2. However, for protons interacting with a power-law distribution of photons, where there are a sufficient number of high-energy photons to excite higher energy resonances as well as allow direct pion production, the ratio of charged pions, $\pi^{\pm}$, to neutral pions is actually closer to 2 : 1. This ratio is more or less independent of the photon index (Rachen & Mészáros, 1998). As an approximation, we take the cross section of the delta resonance, but only consider the high energy electrons produced by the $\pi^{\pm}$ decay. This approximation underestimates the high energy electron production rate by a factor of 3 when the GRB jet is opaque to photons from the π^0 decay.

5.2.1 Analytical Estimate

As with the π^0, at the threshold energy, the π^+ (and subsequently the μ^+) are produced almost at rest in the rest frame of the proton and therefore have the same Lorentz factor as the proton given in eq(5.1). On average, the positron carries roughly one-third of the energy of the muon (the remaining two-thirds goes to neutrinos). The Lorentz factor of the e^+ in the comoving jet rest frame is

$$\gamma_e \sim \frac{1}{3}\frac{m_\mu}{m_e}\gamma_p \sim 10^6 \Gamma_2 \nu_{p,6}^{-1} (1+z)^{-1}, \tag{5.2}$$

m_μ and m_e are the muon and electron masses respectively.

By requiring that a typical positron produced through pion decay, with Lorentz factor given by eq (5.2) and charge q, radiates at a desired frequency ν ($\sim$ 100 MeV for Fermi-LAT), we solve for the magnetic field in the jet rest frame, B, in Gauss.

$$\frac{qB\gamma_e^2\Gamma}{2\pi m_e c(1+z)} \sim 1.6\times 10^{-4}\nu_8 \text{ erg} \Rightarrow B \sim 100 \nu_8 \nu_{p,6}^2 (1+z)^3 \Gamma_2^{-3} \text{ Gauss} \tag{5.3}$$

The above value for B requires the minimal proton energy to match an observed flux. If the energy requirements are too large when B is equal to eq (5.3), they will be even worse when the magnetic field is not equal to eq (5.3).[2]

---

[2] Equation (5.3) is close to the magnetic field value requiring the minimal proton energy when the peak frequency of a positron with Lorentz factor given by eq (5.2) is above the cooling frequency ν_c. If a typical photo-pion produced positron is not cooled by synchrotron

The observed specific synchrotron flux, f_ν, is

$$f_\nu = \frac{\sqrt{3} q^3 B N_e \Gamma (1+z)}{4\pi d_L^2 m_e c^2} \approx 1.2\ \mu\mathrm{Jy}\ N_{e,50} B \Gamma d_{L,28}^{-2} (1+z), \tag{5.4}$$

where N_e is the number of electrons that radiate at ν, and d_L is the luminosity distance to the GRB. Thus, the number of e^+ needed to produce the observed flux at ν is

$$N_e \approx 8 \times 10^{47} \frac{f_{\nu,\mu\mathrm{Jy}} d_{L,28}^2}{B \Gamma_2 (1+z)}. \tag{5.5}$$

where $f_{\nu,\mu\mathrm{Jy}}$ is the observed flux in μJy.

The number of protons, with energy above the pion production threshold, required to produce the necessary electrons in eq (5.5) is $N_p \approx \frac{3}{2} N_e / \tau_{p\gamma}$, where $\tau_{p\gamma}$ is the probability that a photon of frequency $\sim \nu_p (1+z)/\Gamma$ collides with a proton with a Lorentz factor given by eq (5.1) and produces a pion. The probability of a proton undergoing a photopion reaction is approximately equal to the optical depth to pion production and is given by $\tau_{p\gamma} = \sigma_{p\gamma} n_\gamma R / \Gamma$, where $\sigma_{p\gamma}$ is the cross section for the delta resonance, $\sigma_{p\gamma} = 5 \times 10^{-28}$ cm^2. n_γ is the number density of photons in the comoving frame of the GRB jet, and R is the distance from the center of the explosion. For a GRB of observed isotropic luminosity L_γ (integrated over the sub-MeV part of the Band function spectrum) and observed peak frequency ν_p (in eV), the number density of photons in the comoving frame of a GRB jet is

$$n_\gamma = \frac{L_\gamma (1+z)^{-1}}{4\pi R^2 \Gamma c \nu_p (1.6 \times 10^{-12}\ \mathrm{erg/eV})} \approx 2 \times 10^{14} L_{\gamma,52} R_{15}^{-2} \Gamma_2^{-1} \nu_{p,6}^{-1} (1+z)^{-1}\ \mathrm{cm}^{-3}. \tag{5.6}$$

---

radiation, for typical GRB spectra and efficient proton acceleration, the minimum necessary proton luminosity will occur at a B such that ν_c is 100 MeV. For the vast majority of allowed GRB parameter space, the photo-pion peak is cooled, so the statement that eq (5.3) is a best case scenario holds.

We find an optical depth of photopion production of

$$\tau_{p\gamma} \approx 0.8 L_{\gamma,52} R_{15}^{-1} \Gamma_2^{-2} \nu_{p,6}^{-1} (1+z)^{-1}. \tag{5.7}$$

Using (5.5) and (5.7) the number of protons needed to produce a specific flux, f_ν, is

$$N_p \approx 10^{48} f_{\nu,\mu\mathrm{Jy}} d_{L,28}^2 \Gamma_2 R_{15} \nu_{p,6} B^{-1} L_{\gamma,52}^{-1}. \tag{5.8}$$

The corresponding energy in these protons is

$$E_p \approx N_p(\gamma_p m_p c^2)\Gamma \approx 3.0 \times 10^{51} \ \frac{\Gamma_2^3 f_{\nu,\mu\mathrm{Jy}} d_{L,28}^2 R_{15}}{B L_{\gamma,52}(1+z)} \ \mathrm{erg}. \tag{5.9}$$

It is more useful to consider the luminosity carried by these protons, L_p, as the proton luminosity can be directly compared to the observed γ-ray luminosity, L_γ. The ratio L_γ/L_p will allow us to determine the efficiency of the photopion process for the generation of $\gtrsim 100$ MeV γ-rays. The proton luminosity is related to E_p by

$$L_p = E_p \Gamma \times \max\left\{t_{\mathrm{dyn}}^{-1}, t_{\mathrm{cool}}^{-1}\right\}, \tag{5.10}$$

where t_{dyn} is the dynamical time in the jet comoving frame,

$$t_{\mathrm{dyn}} = \frac{R}{2c\Gamma} \approx 170 R_{15} \Gamma_2^{-1} \ \mathrm{s}, \tag{5.11}$$

and $t_{\mathrm{cool}} = \gamma_e m_e c^2 / P_{\mathrm{syn}}$ is the synchrotron cooling time in the jet frame. P_{syn} is the total synchrotron power radiated by a positron. Using the magnetic field in the jet comoving frame given in eq (5.3), t_{cool} becomes

$$t_{\mathrm{cool}} = \frac{6\pi m_e c}{\sigma_T B^2 \gamma_e} \approx 8 \times 10^{-2} \ \frac{\Gamma_2^5}{\nu_8^2 \nu_{p,6}^3 (1+z)^5} \ \mathrm{s}. \tag{5.12}$$

Inverse Compton cooling is neglected because the electrons considered here have a Lorentz factor of $\gtrsim 10^6$; so the IC radiation is greatly decreased because of Klein-Nishina suppression.

Substituting Equations (5.3), (5.9), (5.11), & (5.12) into (5.10), we find the minimum proton luminosity necessary to match a flux of $f_{\nu,\mu\mathrm{Jy}}$ at ν_8 with the photo-pion process is

$$L_p \gtrsim \begin{cases} 2\times10^{49}\ \Gamma_2^8 L_{\gamma,52}^{-1}\nu_8^{-1}\nu_{p,6}^{-2} f_{\nu,\mu\mathrm{Jy}} d_{L,28}^2 (1+z)^{-4}\ \mathrm{erg\ s^{-1}} & t_{\mathrm{dyn}} < t_{\mathrm{cool}} \\ 4\times10^{52}\ \Gamma_2^2 R_{15} L_{\gamma,52}^{-1}\nu_8 \nu_{p,6} f_{\nu,\mu\mathrm{Jy}} d_{L,28}^2 (1+z)\ \mathrm{erg\ s^{-1}} & t_{\mathrm{cool}} < t_{\mathrm{dyn}}. \end{cases} \tag{5.13}$$

At first glance, the proton luminosity does not seem prohibitively large. However, the strong dependence on Γ has the potential to increase the proton energy requirement tremendously.

To assess the viability of the photo-pion process producing the $\gtrsim 100$ MeV photons detected by *Fermi*, let us consider a bright *Fermi*-LAT burst, GRB 080916C (Abdo et al., 2009b). This burst was detected at a redshift of 4.3, which has a corresponding $d_{L,28} = 12$. The peak of the observed spectrum was at 400 keV, and the flux at 100 MeV during the prompt emission was $f_\nu \sim 3\ \mu$Jy. The γ-ray isotropic luminosity for GRB 080916C was $L_{\gamma,52} \sim 20$, and the minimum jet Lorentz factor was estimated to be $\Gamma_2 \sim 9$ (Abdo et al., 2009b). For these parameters, we find $t_{\mathrm{cool}} < t_{\mathrm{dyn}}$ as long as $R > 10^{15}$ cm, implying that the required luminosity in protons with $\gamma_p \gtrsim 10^5$ is $L_p \sim 1.5 \times 10^{56}\ R_{15}$ erg s^{-1}. This proton luminosity is a factor of $\sim$ 700 times larger than the γ-ray luminosity at $R = 10^{15}$ cm. Below $R = 10^{15}$, $t_{\mathrm{dyn}} < t_{\mathrm{cool}}$ and the proton luminosity has no R dependence.[3] This efficiency is below the efficiencies of the order 10-20% estimated for other GRBs using afterglow modeling (*e.g.*, Panaitescu & Kumar, 2002; Fan & Piran, 2006; Zhang et al.,

---

[3] See previous footnote about how the luminosity estimate may be too pessimistic when $t_{\mathrm{dyn}} < t_{\mathrm{cool}}$. A more accurate calculation that accurately minimizes L_p with respect to B for a given R, Γ, *etc*, is presented in the §5.2.2.

2007) and makes the photo-pion process an unlikely candidate to produce the prompt-LAT emission observed in this GRB.

5.2.1.1 Neutrino Flux

In addition to producing high energy electrons, photo-pion production also results in high energy neutrinos. For the photo-pion production models of the observed LAT emission, it is possible to directly correlate the flux at 100 MeV to an expected flux of neutrinos. Since there are two muon neutrinos created for every e^+ in π^+ decay, we can simply use eq (5.5) and (5.3) to find corresponding number of neutrinos,

$$N_\nu = 10^{46}\ f_{\nu,\mu\mathrm{Jy}} d_{L,28}^2 \nu_8^{-1} \nu_{p,6}^{-2} \Gamma_2^2 (1+z)^{-4} \tag{5.14}$$

These neutrinos will have the same energy as the electrons on average, with an observed energy of

$$E_\nu = 10^5 \Gamma_2^2 \nu_{p,6}^{-1} (1+z)^{-2}\ \mathrm{GeV} \tag{5.15}$$

Therefore, we expect an observed neutrino flux, F_ν, at $10^5\ \Gamma_2^2 \nu_{p,6}^{-1}(1+z)^{-2}$ GeV of

$$F_\nu = E_\nu (1+z) N_\nu \Gamma \times \frac{1}{4\pi d_L^2} \max\left\{t_{\mathrm{dyn}}^{-1}, t_{\mathrm{cool}}^{-1}\right\}, \tag{5.16}$$

$$F_\nu \approx \begin{cases} 5\times 10^{-7}\ f_{\nu,\mu\mathrm{Jy}} R_{15}^{-1} \Gamma_2^6 \nu_8^{-1} \nu_{p,6}^{-3} (1+z)^{-5}\ \mathrm{GeV\ cm^{-2} s^{-1}} & t_{\mathrm{dyn}} < t_{\mathrm{cool}} \\ 10^{-3}\ f_{\nu,\mu\mathrm{Jy}} \nu_8\ \mathrm{GeV\ cm^{-2} s^{-1}} & t_{\mathrm{cool}} < t_{\mathrm{dyn}}. \end{cases} \tag{5.17}$$

The neutrino flux does not depend on the luminosity of the GRB, as it is fixed by the flux at ν_8, the peak of the photo-pion synchrotron emission. When the photo-pion electrons are in the cooled regime—as is expected for much of the GRB parameter space—the neutrino flux does not depend on any of the jet parameters. The neutrino flux depends only on the observed LAT flux at 100 MeV; when the electrons are in the fast cooling regime, the synchrotron flux depends directly on the electron energy flux, and the neutrino flux depends directly on the electron energy flux. Of course, the neutrino energy does depend on Γ, as seen from eq (5.15).

To get a rough idea of an expected neutrino count-rate at IceCube, we fit the averaged effective area for muon neutrinos at IceCube given in Abbasi et al. (2012) by $A \approx 100\ \mathrm{m}^2 \times \sqrt{E_\nu/(100\ \mathrm{TeV})}$. Our fit agrees well with the averaged effective area of 59-string detector when $E_\nu > 3 \times 10^4$ GeV. We expect the following neutrino counts per second of LAT emission from the photo-pion process:

$$\frac{dN_\nu}{dt} \approx \begin{cases} 5 \times 10^{-6}\ f_{\nu,\mu\mathrm{Jy}} R_{15}^{-1} \Gamma_2^{5} \nu_8^{-1} \nu_{p,6}^{-2.5} (1+z)^{-4}\ \mathrm{counts\ s}^{-1} & t_{\mathrm{dyn}} < t_{\mathrm{cool}} \\ 10^{-2}\ f_{\nu,\mu\mathrm{Jy}} \Gamma_2^{-1} \nu_8 \nu_{p,6}^{0.5} (1+z)\ \mathrm{counts\ s}^{-1} & t_{\mathrm{cool}} < t_{\mathrm{dyn}}. \end{cases} \tag{5.18}$$

Therefore for a bright GRB detected by the *Fermi*-LAT with $f_{\nu,\mu\mathrm{Jy}} \sim 2$, $\Gamma_2 \sim 9$, $z \sim 2$, $\nu_{p,6} \sim 1$, and $T_{90} = 10$ s, We find that $t_{\mathrm{cool}} < t_{\mathrm{dyn}}$ if $R > 10^{15}$ cm. If $R > 10^{15}$ cm, we expect about 0.07 neutrinos of energy 9.0×10^5 GeV over the course of the burst. If $R < 10^{15}$ cm, the number of neutrinos is increased by a factor R_{15}^{-1} and the energy stays 9.0×10^5 GeV. And so if we add up the contributions from all *Fermi*-LAT bursts, we expect IceCube to detect ~ 1 neutrino.

5.2.2 Numerical Calculation

The calculation presented in §5.2.1 is a rough estimate to the energy requirement for protons, but it doesn't give any spectral information about the photo-pion radiation and assumes that all the protons have the same energy. Furthermore, it doesn't take the finite width of the delta resonance into account. All of these corrections go in the direction of decreasing the efficiency of the photo-pion process. A more rigorous calculation is presented in this subsection.

The distribution of photons in the jet rest frame is assumed to be isotropic, and the Band function is approximated by

$$\frac{dn}{d\epsilon}(\epsilon) = n_{\epsilon_p} \times \begin{cases} \left(\frac{\epsilon}{\epsilon_p}\right)^{-\alpha} & \text{for } \epsilon_{\min} \le \epsilon \le \epsilon_p \\ \\ \left(\frac{\epsilon}{\epsilon_p}\right)^{-\beta} & \text{for } \epsilon_p < \epsilon. \end{cases} \tag{5.19}$$

Here $\epsilon_p = h\nu_p(1+z)/(\Gamma m_e c^2) \approx .02\Gamma_2^{-1}\nu_{p,6}(1+z)$ is the dimensionless photon energy at the peak of the spectrum in the jet comoving frame, and $\epsilon_{\min}$ is the dimensionless photon energy below which the Band function no longer fits the observed GRB spectrum. $\epsilon_{\min}$ is poorly constrained by GRB observations, and depends on the prompt radiation mechanism and radius of emission for the prompt emission. If $\epsilon_{\min}$ corresponds to the synchrotron self-absorption frequency, it is likely of order 10^{-7}, corresponding to an observed frequency of a few eV. We more conservatively assign an $\epsilon_{\min}$ value based on the lowest observed frequencies by *Fermi* $\nu_{\min} \sim 1$ keV, with a corresponding $\epsilon_{\min} \approx 2 \times 10^{-5}\Gamma_2^{-1}\nu_{\min,3}(1+z)$. In reality, the choice of $\epsilon_{\min}$ has very little effect on the synchrotron flux in the *Fermi*-LAT band, as the photo-pion positrons and electrons produced from a proton interacting with photons of energy $\epsilon_{\min}$ will be of very high Lorentz factor, $\gamma_e \sim 10^9$. For our calculation, $\epsilon_{\rm min}$ corresponds to a $\nu_{\rm min}$ of $\sim$ 1 keV and is included in our calculations only for completeness.

If $\alpha \sim 1$ and the GRB has an isotropic luminosity L_γ, then the value for the number density of photons per $m_e c^2$ at ϵ_p, n_{ϵ_p}, is

$$n_{\epsilon_p} = 8 \times 10^{15} L_{\gamma,52} R_{15}^{-2} \nu_{p,6}{}^{-2} \left(1+z\right)^{-2} \quad \mathrm{cm}^{-3}. \tag{5.20}$$

We assume that the proton number distribution is a power law,

$$dN_p(\gamma_p) = N_{p,i} \left(\frac{\gamma_p}{\gamma_i}\right)^{-p} d\gamma_p \quad \gamma_i < \gamma_p < \gamma_{\rm max}. \tag{5.21}$$

with a minimum Lorentz factor $\gamma_i \sim 10$ and a maximum Lorentz factor given by requiring the protons to be confined to the jet, *i.e.*, the Hillas criterion, $\gamma_{\rm max} = \frac{qBR}{\Gamma m_p c^2} = 3 \times 10^6 B R_{15} \Gamma_2^{-1}$ (Hillas, 1984). $N_{p,i}$ is the number of protons in the emitting region of a GRB between γ_i and $\gamma_i + d\gamma_p$. As these high energy protons travel through the jet, they will interact with the photons that make up the Band function, creating secondary particles. The total interaction rate, $\dot{N}_{p\gamma}$, for a proton with Lorentz factor γ_p and a photon with energy ϵ depends on the angle-integrated cross section: $\sigma_{p\gamma}(\epsilon')$. ϵ' is the energy of the photon in the nuclear rest frame, $\epsilon' = \gamma_p \epsilon (1 - \beta_p \mu)$, where μ is the cosine of the angle between the proton and photon and β_p is the velocity of the proton divided by c. The interaction rate is

$$\dot{N}_{p\gamma} = \frac{c}{4\pi} \int d\Omega \int d\epsilon \; n(\epsilon, \Omega)(1 - \beta_p \mu) \sigma_{p\gamma}(\epsilon'). \tag{5.22}$$

Since $\gamma_p \gg 1$, $\beta_p \sim 1$, and we are approximating the sub-MeV Band photons as isotropic in the rest frame of the jet, the number of scatterings is approximated by

$$\frac{d\dot{N}_{p\gamma}}{d\gamma_p} = \frac{c}{2\gamma_p^2} \frac{dN_p}{d\gamma_p} \int_0^\infty d\epsilon \; \frac{n(\epsilon)}{\epsilon^2} \int_0^{2\gamma_p \epsilon} d\epsilon' \; \epsilon' \sigma_{p\gamma}(\epsilon'). \tag{5.23}$$

We approximate the cross section of the delta resonance, $\sigma_{p\pi}(\epsilon')$, as 5×10^{-28} cm^2 if $530 < \epsilon' < 760$ and 0 otherwise. As before, we treat the pion and muon as decaying instantaneously without any energy losses and approximate $\gamma_e = 70\gamma_p$. Equation (5.23), re-written in terms of the produced electrons, is

$$\frac{d\dot{N}_e}{d\gamma_e} = \frac{c}{10^4\gamma_e^2}\frac{dN_p}{d\gamma_p}\frac{d\gamma_p}{d\gamma_e}\int_0^\infty d\epsilon\ \frac{n(\epsilon)}{\epsilon^2}\int_0^{2\gamma_p\epsilon} d\epsilon'\ \epsilon'\sigma_{p\gamma}(\epsilon'). \tag{5.24}$$

When evaluating the scattering rate, it is convenient to define two electron Lorentz factors of interest: $\gamma_{\rm peak}$, the electron that is produced from a proton interacting with photons at the observed peak in the gamma-rays, and $\gamma_{\rm break}$, the electron that is produced from a proton interacting with the lowest energy photon in the Band function, which is taken to be $\nu_{\rm min}$. $\gamma_{\rm peak}$ and $\gamma_{\rm break}$ are equal to

$$\begin{aligned}\gamma_{\rm peak} &= 1.2\times 10^6\Gamma_2\nu_{p,6}^{-1}(1+z)^{-1} && (5.25)\\ \gamma_{\rm break} &= 1.2\times 10^9\Gamma_2\nu_{{\rm min},3}^{-1}(1+z)^{-1}. && (5.26)\end{aligned}$$

Carrying out the integration in equation (5.24), we find the rate of electrons produced through the photo-pion processes is

$$\frac{d\dot{N}}{d\gamma_e} \approx \begin{cases} N_{e,p}\left(\dfrac{\gamma_e}{70\gamma_i}\right)^{\beta-p-1}, & 70\gamma_i \le \gamma_e \le \gamma_{\rm peak} \\ N_{e,p}\left(\dfrac{\gamma_{\rm peak}}{70\gamma_i}\right)^{\beta-p-1}\left(\dfrac{\gamma_e}{\gamma_{\rm peak}}\right)^{\alpha-p-1}, & \gamma_{\rm peak} < \gamma_e \le \gamma_{\rm break} \\ N_{e,p}\left(\dfrac{\gamma_{\rm peak}}{70\gamma_i}\right)^{\beta-p-1}\left(\dfrac{\gamma_{\rm break}}{\gamma_{\rm peak}}\right)^{\alpha-p-1}\left(\dfrac{\gamma_e}{\gamma_{\rm break}}\right)^{-p-2}, & \gamma_{\rm break} < \gamma_e \end{cases} \tag{5.27}$$

$$N_{e,p} \approx 0.3(6\times 10^{-5})^\beta N_{p,i}\gamma_i^{\beta-1}L_{\gamma,52}R_{15}^{-2}\nu_{p,6}^{\beta-2}\,(1+z)^{\beta-2}\,\Gamma_2^{-\beta}/(\beta+1). \tag{5.28}$$

We now derive the previous estimate of how much energy the protons would need to carry to produce the observed Fermi-LAT flux at 100 MeV.

For simplicity, we set α and β to the typical GRB parameters $\alpha = 1$ and $\beta = 2.2$. We assume the protons have a power law index of $p = 2$ and $\gamma_i = 10$, corresponding to efficient acceleration in shocks. Then, the majority of the energy in the photo-pion electrons is contained in the electrons with $\gamma_{\rm peak} \leq \gamma_e \leq \gamma_{\rm break}$. This section of the power law is

$$\frac{d\dot{N}}{d\gamma_e} = 7 \times 10^{-12} N_{p,i} L_{\gamma,52} R_{15}^{-2} \nu_{p,6}^{-1} (1+z)^{-1} \Gamma_2^{-1} \left(\frac{\gamma_e}{10^6}\right)^{-2}. \tag{5.29}$$

To calculate the total number of electrons produced, we solve the following continuity equation

$$\frac{\partial N(\gamma_e)}{\partial t} + \frac{\partial}{\partial \gamma_e} \left\{ \dot{\gamma}_e N(\gamma_e) \right\} = \frac{d\dot{N}}{d\gamma_e}. \tag{5.30}$$

We approximately solve this equation by following the standard procedure of breaking up the continuity equation into two regimes: one where the electrons are cooling slowly, *i.e.*, $t_{\rm dyn} < t_{\rm cool}$, and another where cooling losses are important, $t_{\rm dyn} > t_{\rm cool}$. The solution of differential equation (5.30) is then approximately:

$$N(\gamma_e) = \begin{cases} t_{\rm dyn} \dfrac{d\dot{N}}{d\gamma_e}, & t_{\rm dyn} < t_{\rm cool} \\ \\ \dfrac{1}{\dot{\gamma}_e} \displaystyle\int_{\gamma_e}^{\infty} d\gamma \dfrac{d\dot{N}}{d\gamma}, & t_{\rm dyn} > t_{\rm cool}, \end{cases} \tag{5.31}$$

Two different cooling mechanisms are considered: synchrotron and inverse Compton cooling. To see which is the more dominant cooling process, we compare the power radiated by each process. The synchrotron power for electrons with $\gamma_e = \gamma_{\rm peak}$ is

$$P_{\rm syn}(\gamma_{\rm peak}) = 1.6 \times 10^{-3} \Gamma_2^2 (1+z)^{-2} \nu_{p,6}^{-2} B^2 \text{ erg/s}. \tag{5.32}$$

From the condition $t_{\rm cool} < t_{\rm dyn}$, the electrons at the peak of the distribution will be cooled via synchrotron if

$$B > 2\ R_{15}^{-0.5}\nu_{p,6}^{0.5}(1+z)^{0.5}\ \text{Gauss}. \tag{5.33}$$

eq (5.33) tells us that synchrotron cooling losses are important to consider. However, for completeness, our estimate will consider both possibilities, when $\gamma_{\rm peak}$ is above cooling and below cooling.

For inverse Compton losses, while the energy density in the photons can be very large, particularly at distances less than $\sim 10^{16}$ cm, the inverse Compton radiated power is greatly reduced due to Klein-Nishina suppression. For the electron Lorentz factor given in eq (5.25), all of the prompt sub-MeV emission will be in the Klein-Nishina regime if $\gamma_{\rm peak}\epsilon_{\rm min} > 1$, or $\nu_{p,6} < 20\nu_{\rm min,3}$. The power radiated due to IC scattering in the Klein-Nishina regime is given in Blumenthal (1971):

$$P_{KN}(\gamma) = m_e c^3 \pi r_0^2 \int_{\frac{1}{\gamma}}^{\infty} d\epsilon\ \frac{1}{\epsilon}\frac{dn}{d\epsilon}\left(\log\left(4\gamma\epsilon\right) - \frac{11}{6}\right). \tag{5.34}$$

where r_0 is the classical electron radius. For $\gamma = \gamma_{\rm peak}$, neglecting the logarithmic dependencies of variables and assuming $\alpha \sim 1$, the IC radiated power is

$$P_{KN}(\gamma_{\rm peak}) = 2\times 10^{-1} L_{\gamma,52} R_{15}^{-2}\nu_{p,6}^{-2}(1+z)^{-2}\left(\frac{\nu_{p,6}}{\nu_{\rm min,3}}\right). \tag{5.35}$$

From equations (5.32) and (5.35), the ratio of synchrotron power to Inverse Compton power at $\gamma_{\rm peak}$ is

$$\frac{P_{syn}}{P_{KN}} = 8\times 10^{-3} L_{\gamma,52}^{-1}\Gamma_2^2 B^2 R_{15}^2\left(\frac{\nu_{\rm min,3}}{\nu_{p,6}}\right). \tag{5.36}$$

If we define ϵ_B as the ratio of energy density in the magnetic field to energy density in radiation, the ratio becomes

$$\frac{P_{syn}}{P_{KN}} = 50\epsilon_{B,-2}\left(\frac{\nu_{\rm min,3}}{\nu_{p,6}}\right). \tag{5.37}$$

Unless ϵ_B is small, the synchrotron emission will dominate over the inverse Compton emission. The inverse Compton scattered photons will have on average an energy in the jet's rest frame of $\gamma_e m_e c^2 \sim 0.5$ TeV for electrons with $\gamma_e = \gamma_{\rm peak}$. These photons will quickly pair produce and form a cascade of secondary particles. A full treatment of the hadronic cascade is beyond the scope of this paper. In any case, as can be seen in equation (5.37), the energy in this cascade will be less than the synchrotron energy radiated by the photo-pion produced electrons; allowing us to ignore these $e^{\pm}$ pairs when for estimating the flux at 100 MeV.

The electron number distribution created by the photo-pion process for $\gamma_{\rm peak} \leq \gamma_e \leq \gamma_{\rm break}$ is

$$\frac{dN}{d\gamma_e} = \begin{cases} 10^{-9}\ N_{p,i} L_{\gamma,52} R_{15}^{-1} \nu_{p,6}^{-1} (1+z)^{-1} \Gamma_2^{-2} \gamma_{e,6}^{-2}, & t_{\rm dyn} < t_{\rm cool} \\ 5 \times 10^{-9}\ B^{-2} N_{p,i} L_{\gamma,52} R_{15}^{-2} \nu_{p,6}^{-1} (1+z)^{-1} \Gamma_2^{-1} \gamma_{e,6}^{-3}, & t_{\rm dyn} > t_{\rm cool}. \end{cases} \tag{5.38}$$

The observed synchrotron flux, f_v, at $\nu \sim 100$ MeV, is calculated using the following approximation for synchrotron radiation:

$$f_\nu = (1+z) \int_{\gamma_\nu}^{\gamma_{\rm max}} d\gamma_e \frac{\sqrt{3} q^3 \Gamma B N(\gamma_e)}{4\pi d_L^2 m_e c^2} \left(\frac{\gamma_\nu}{\gamma_e}\right)^{2/3}, \tag{5.39}$$

$$\gamma_\nu^2 = \frac{2\pi m_e c (1+z) \nu}{q B \Gamma (4.13 \times 10^{-15}\ \text{eV s})}. \tag{5.40}$$

Using equation (5.3) for the magnetic field value, we calculate the necessary luminosity in protons to produce γ-rays through the photo-pion process. The result we found for L_p is

$$L_p = \begin{cases} 3 \times 10^{51}\ \Gamma_2^8 L_{\gamma,52}^{-1} \nu_8^{-1} \nu_{p,6}^{-2} f_{\nu,\mu\rm Jy} d_{L,28}^2 (1+z)^{-4}\ \text{erg s}^{-1}, & t_{\rm dyn} < t_{\rm cool} \\ 7 \times 10^{54}\ \Gamma_2^2 R_{15} L_{\gamma,52}^{-1} \nu_8 \nu_{p,6} f_{\nu,\mu\rm Jy} d_{L,28}^2 (1+z)\ \text{erg s}^{-1}, & t_{\rm dyn} > t_{\rm cool}. \end{cases} \tag{5.41}$$

In comparison to the previous estimate for L_p given in equation (5.13), the values for L_p in equation (5.41) are considerably larger, by a factor of ~ 100. A factor of ~ 20 is attributable to the fact that unlike the estimate given in §5.2.1, this calculation considers protons that are part of a power law distribution that extends over several decades of energy. Additional factors come from the finite width of the delta resonance and keeping track of the factors that come from integration. For the parameters of GRB 080916C, for the expected case $t_{\rm cool} < t_{\rm dyn}$, the required proton luminosity is $L_p \sim 3 \times 10^{58}\ R_{15}$ erg s^{-1}. So, the luminosity in the protons is 10^5 times larger than luminosity in the γ-rays at R_{15}, which is too large to be realistic for a stellar mass object.

We define the efficiency, η, as

$$\eta \equiv \frac{L_\gamma}{L_p} = \begin{cases} 3\ \Gamma_2^{-8} L_{\gamma,52}^2 \nu_8 \nu_{p,6}^2 f_{\nu,\mu{\rm Jy}}^{-1} d_{L,28}^{-2} (1+z)^4, & t_{\rm dyn} < t_{\rm cool} \\ 10^{-3}\ \Gamma_2^{-2} R_{15}^{-1} L_{\gamma,52}^2 \nu_8^{-1} \nu_{p,6}^{-1} f_{\nu,\mu{\rm Jy}}^{-1} d_{L,28}^{-2} (1+z)^{-1}, & t_{\rm dyn} > t_{\rm cool}. \end{cases} \tag{5.42}$$

In the previous equation, the cooled and uncooled estimates for η were calculated by choosing a magnetic field to ensure the energy peak of the photo-pion-produced electrons radiated at 100 MeV. While this is convenient and pretty accurate maximum efficiency for analytical estimation, we also numerically calculated the maximum efficiency, allowing B to be a free parameter while fixing all the other parameters (R, Γ, L_γ, ν_p, *etc*). As bounds on B, we set the minimum magnetic field value by requiring that the power radiated through inverse Compton is no more than 100 times the synchrotron power for an electron that has a synchrotron peak at 100 MeV. We set a maximum value for B such that the energy in the magnetic field is at most 10 times the energy in the photons. For the parameter space we considered, the B that maximized η was well within these bounds. For a given L, Γ, R, and p, we calculate the maximum efficiency of photo-pion electrons radiating the desired flux of 1 μJy at 100 MeV. This maximum efficiency is plotted in figure 5.1. The part of equation (5.42) corresponding to fast electron cooling gives an accurate prediction of the maximum η. In the slow cooling regime, equation (5.42) predicts too small a value of η; in this case the maximum efficiency is found when B is a value such that 100 MeV is ν_c.

As illustrated in figure 5.1 and equation (5.42), R, Γ and L_γ are the only parameters capable of changing η significantly; p can as well, but it is fixed by the desired photo-pion spectrum and therefore not a free parameter. From typical GRB spectra, we expect p to be in the rage 2.4–2.8 to match typical LAT spectra. In the bottom right panel of figure 5.1, we can see that p has almost no effect on η when we only consider the protons creating the > 100 MeV photons (see upper red line in figure 5.1). In figure 5.2, to explore how the efficiency changes with R, Γ, and L_γ we plotted η in the $R-\Gamma$ plane for various L_γ. It is interesting to note that although η scales as L_γ^2 for a fixed R, Γ, the maximum efficiency in the $R-\Gamma$ plane only scales as $\sim L_\gamma$ because the available parameter space decreases with increasing L_γ due to $\gamma+\gamma$ pair production

5.3 Bethe-Heitler Pair Production

Through Bethe-Heitler pair production, protons and photons interact to create electron-position pairs directly, $p+\gamma \rightarrow p+e^{+}+e^{-}$. The Bethe-Heitler cross-section and the energy of the produced electron-positron pair depend strongly on the angle between the outgoing electron/positron and the proton. Therefore, it is not possible to use the integrated cross section to calculate the secondary electron production. Assuming that the protons and photons are

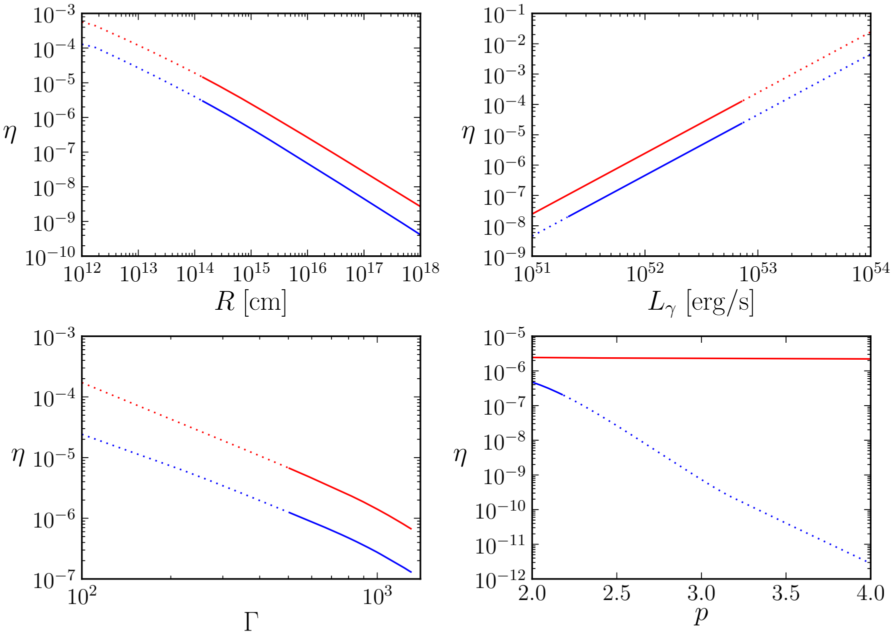

Figure 5.1: A plot of the maximum efficiencies for the photo-pion process radiating a typical *Fermi*-LAT flux of 1 μJy at 100 MeV as a function of R, L, Γ, and p. The lower blue lines corresponds to a more physically realistic case of a proton power law extending from a Lorentz factor of 10 to the Hillas criterion for the confinement of protons. The upper red lines are the efficiency only considering the energy in the protons that produce the pions and then electrons that radiate at LAT frequencies. These red lines represent an absolute maximum possible efficiency and corresponds roughly to our calculation in §5.2.1. The dotted line corresponds to the cases when LAT emission could not be seen by an observer, either because the emission happens below the photosphere or because the jet would be opaque to photons of 10 GeV due to $\gamma + \gamma$ pair production. When the parameters are not on the x-axis, values of $L_\gamma = 10^{52}$ erg/s, $R = 10^{15}$ cm, $\Gamma = 800$, $\nu_p = 1$ MeV, $z = 2$, $d_L = 4.9 \times 10^{28}$ cm, and $p = 2$ are taken. The photon power law indices of the Band function were set to $\alpha = 1$ and $\beta = 2.2$. Since ν_p, α, and β are unable to change the maximum η by more than an order of magnitude, their corresponding plots are omitted.

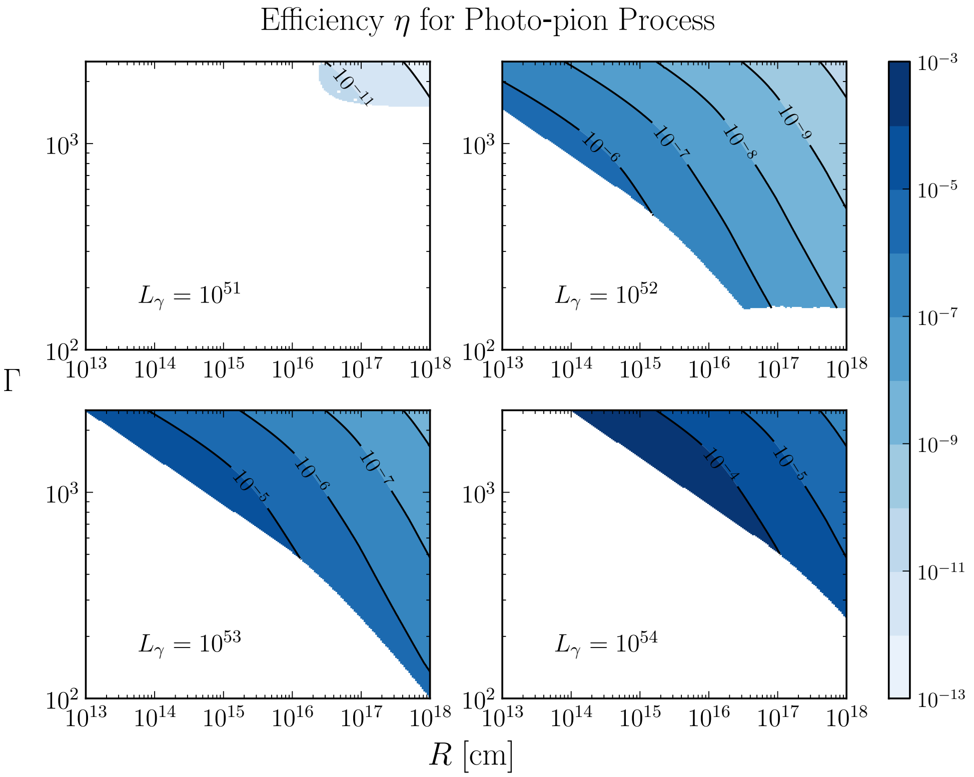

Figure 5.2: The maximum η is plotted in the $R-\Gamma$ plane for various values of L_γ to match a flux of $f_\nu = 1$ μJy at 100 MeV. As in Figure 5.1, we fix $\nu_p = 1$ MeV, $z = 2$, $d_L = 4.9 \times 10^{28}$ cm, and $p = 2$. The values of η in this figure correspond to the maximum possible efficiency, *i.e.*, the red lines in figure 5.1. The photon power law indices were set to typical values for the Band function, $\alpha = 1$ and $\beta = 2.2$. Where η is not shown, the place of emission is either below the photosphere or opaque to radiation of 10 GeV due to $\gamma+\gamma$ pair production.

isotropic in the jet's rest frame and using the head on approximation, *i.e.*, the angle between the photon and proton is zero, *i.e.* $\epsilon' = 2\gamma_p \epsilon$, the equation for the rate of production of secondary electrons is:

$$\frac{d\dot{N}_e}{d\gamma_e}(\gamma_e) = 2c \int_0^\infty d\epsilon \; n(\epsilon) \int_1^\infty d\gamma_p \; N_p(\gamma_p) \frac{d\sigma(\epsilon, \gamma_p)}{d\gamma_e}. \tag{5.43}$$

In this equation $N_p(\gamma_p)$ is the number of protons with Lorentz factor γ_p and $n(\epsilon)$ is number density of photons with energy ϵ. The formula for the differential Bethe-Heitler cross section, σ_{BH}, in the Born approximation, integrated over angles in the highly relativistic regime, was derived by Bethe & Maximon (1954) (see Rachen (1996) for a more recent review).

$$\frac{d\sigma_{BH}}{d\gamma'_+} = \frac{3\alpha_f \sigma_T}{2\pi \epsilon'^3} \left({\gamma'_+}^2 + {\gamma'_-}^2 + \frac{2}{3}\gamma'_+ \gamma'_- \right) \left(\log \frac{2\gamma'_+ \gamma'_-}{\epsilon'} - \frac{1}{2} \right). \tag{5.44}$$

In this equation, $\gamma'_+ (\gamma'_-)$ is the Lorentz factor of the positron (electron), α_f is the fine structure constant, and all of the above quantities are in the proton rest frame. Much of the contribution to the angle-integrated cross section comes from angles between the photon and outgoing $e^\pm$ of order $\theta'_\pm = \frac{1}{\gamma'_\pm}$. When $\gamma_p \gg \gamma'_\pm$, the Lorentz factor of $e^\pm$ in the jet's rest frame is

$$\gamma_\pm = \gamma_p \gamma'_\pm \left(1 - \beta_p \beta'_\pm \cos\theta'_\pm\right) \approx \frac{\gamma_p \gamma'_\pm}{2} \left(\gamma_p^{-2} + {\gamma'_\pm}^{-2} + {\theta'_\pm}^{-2} \right) \approx \frac{\gamma_p}{\gamma'_\pm}. \tag{5.45}$$

Therefore, most pairs produced via the Bethe-Heitler process have Lorentz factors (in the jet comoving frame) that are smaller than the proton that created it.

If $\epsilon' \ll m_p/m_e \sim 10^3$, the nuclear recoil of the proton can be neglected and the following equality holds:

$$\gamma'_+ + \gamma'_- = \epsilon'. \tag{5.46}$$

For large ϵ', the differential cross section decreases very rapidly when $\gamma'_\pm < 2$. Therefore, we only consider $\gamma'_\pm \geq 2$, where the differential cross section is more or less constant. In this regime, the differential cross section simplifies to

$$\frac{d\sigma_{BH}}{d\gamma'_+} \approx \frac{\alpha\sigma_T}{\epsilon'}, \text{ if } 2 \leq \gamma'_+ \leq \epsilon' - 2. \tag{5.47}$$

Re-writing eq (5.47) in the jet comoving frame and using the $\epsilon' \approx 2\gamma_p\epsilon$, we find

$$\frac{d\sigma_{BH}}{d\gamma_+} \approx \frac{\alpha\sigma_T}{2\epsilon\gamma_+^2}, \text{ if } \frac{1}{2\epsilon} \leq \gamma_+ \leq \frac{\gamma_p}{2}. \tag{5.48}$$

The integral in equation (5.43) is simplified by considering the approximate expression for the cross-section. The integral is now straight forward to calculate for a Band spectrum with indices α, β and a proton index of p. The result is

$$\frac{d\dot{N}_e}{d\gamma_e}(\gamma_e) \approx \begin{cases} \frac{2c\alpha_f\sigma_T}{\beta(p+1)\gamma_e} n_{\epsilon_p} N_{p,i} \left(\frac{\gamma_e\epsilon_p}{5}\right)^{\beta} \left(\frac{2\gamma_e}{\gamma_i}\right)^{-p} & \text{for } \frac{\gamma_i}{2} \leq \gamma_e \leq 5/\epsilon_p \\ \frac{2c\alpha_f\sigma_T\epsilon_p}{5\beta(p+1)} n_{\epsilon_p} N_{p,i} \left(\frac{10}{\epsilon_p\gamma_i}\right)^{-p} \left(\frac{\epsilon_p\gamma_e}{5}\right)^{\alpha-p-1} & \text{for } 5/\epsilon_p \leq \gamma_e \leq 5/\epsilon_{\min}. \end{cases} \tag{5.49}$$

We now compare Bethe-Heitler pair production to the photo-pion process. The integrated cross section for Bethe-Heitler process is roughly 10 times larger than the cross section for the photo-pion Δ-resonance. For any given proton Lorentz factor γ_p, the photon energy required for Bethe-Heitler is roughly 50 times smaller than for the Δ-resonance. For a given γ_p, the photo-pair will have an average Lorentz factor of $\sim \gamma_p/5$ while the delta resonance will decay to a electron with an energy $\sim 70\gamma_p$. Consider the case where protons with a power-law distribution function with index p are scattering with a isotropic photon power-law spectrum $n(\epsilon) \propto \epsilon^{-a}$. The ratio of the number of $e^\pm$ above a fixed Lorentz factor generated by Bethe-Heitler process compared to those generated by photo-pion process is $\sim 2 \times 10 \times (10^4)^{a-1} \times (300)^{-p+1}$—the first factor comes from the fact that Bethe-Heitler produces a electron-positron pair compared to a single positron produced in the delta-resonance, the second factor is the ratio of the total cross sections for the Bethe-Heitler and photo-pion scatterings, the third factor accounts for the larger number of photons that participate in the Bethe-Heitler process (the threshold energy for Bethe-Heitler is $\epsilon \sim \gamma_e^{-1}$ and the threshold energy for photo-pion is $\sim 10^4 \gamma_e^{-1}$) and the final factor is due to the fewer number of protons that can create electrons with Lorentz factor $\gtrsim \gamma_e$. Therefore, the process that dominates depends strongly on which part of the Band function the protons are interacting with to produce $e^{\pm}$ with Lorentz factor $\gtrsim \gamma_e$. For $\gamma_e \gtrsim 10^6$, the energy threshold for both processes lies below the peak of the Band function, so $a = \alpha \approx 1$. Thus, in this regime, the photo-pion pairs dominate.

However, for $\gamma_e \lesssim 10^3$, the threshold photon energy for both process is above the peak of the gamma ray spectrum, so $a = \beta \approx 2.2$ and the Bethe-Heitler process is a lot more efficient than the photo-pion process. Although relativistic shocks are likely capable of accelerating electrons to $\gamma_e \sim 10^3$, Bethe-Heitler process could still be important if the number of electrons produced above the photosphere vastly outnumber the electrons expected to be in the GRB jet from simple charge neutrality. If the GRB has proton luminosity L_p given by $L_p = \eta^{-1} L_\gamma$, the comoving electron density is $n_e = n_p \approx 2 \times 10^9 \eta^{-1} L_{\gamma,52} \Gamma_2^{-2} R_{15}^{-2}$ cm^{-3}. The number density of Bethe-Heitler produced electrons, n_{BH} is

$$n_{BH} \sim \alpha_f \sigma_T n_\gamma n_p R/\Gamma \quad \Rightarrow \quad \frac{n_{BH}}{n_e} = \alpha_f \sigma_T n_\gamma R/\Gamma. \tag{5.50}$$

Since we want to restrict ourselves to above the photosphere, the optical depth

$\sigma_T n_e R/\Gamma < 1$ or

$$\frac{n_{BH}}{n_e} < \alpha_f \frac{n_\gamma}{n_e} \sim 10^3 \eta \Gamma_2 \nu_{p,6}^{-1} (1+z)^{-1}, \tag{5.51}$$

where n_γ is given by eq (5.6). It is somewhat counter-intuitive, but the Bethe-Heitler process is likely to be most important in jets with lower baryon loading, *i.e.* when η is large. The Bethe-Heitler process could be important for $\gamma_e' \ll 10^5$—especially if for some reason the Fermi mechanism is unable to accelerate electrons to this Lorentz factor in GRB shocks—but for these $e^\pm$ to account for the 100 MeV photons from GRBs via the synchrotron process requires a very large magnetic field and the luminosity carried by such a magnetic field would greatly exceed 10^{52} erg/s. Therefore, it seems that at best there might just be a small part of the parameter space for GRBs where the Bethe-Heitler mechanism could play an interesting role in the generation of prompt γ-ray radiation.

5.4 Proton Synchrotron

Massive particles have suffer less radiative losses than lighter particles, and therefore more massive particles may be able to attain a much larger maximum Lorentz factors than lighter particles in shocks. The maximum Lorentz factor that protons can attain is much larger than the maximum Lorentz factor of electrons. The maximum synchrotron photon energy from a shock-accelerated particle is given by requiring that the synchrotron energy radiated during one acceleration time (on the order of the Larmor time) is equal the energy gained in an acceleration cycle—half of the particle's energy. *i.e.* $\gamma mc/(qB) \times 4B^2 q^4 \gamma^2/(9m^2c^3) \lesssim \gamma mc/2$. The maximum photon energy for a source moving with a Lorentz factor Γ at redshift z is

$$\nu_{\max} \approx \frac{9\Gamma m c^3}{16\pi q^2(1+z)} \sim 50\frac{\Gamma}{1+z}\left(\frac{m}{m_e}\right)\ \mathrm{MeV}. \tag{5.52}$$

While electron synchrotron radiation can only produce photons up to an energy $\sim 50\Gamma/(1+z)$ MeV, the proton synchrotron process can radiate photons up to $10^2\Gamma/(1+z)$ GeV. For this reason, when photons of energies larger than what is allowed by electron synchrotron are detected from a source, proton synchrotron is frequently suggested as a possible radiation mechanism (*e.g.*, Böttcher & Dermer, 1998; Totani, 1998; Aharonian, 2000; Zhang & Mészáros, 2001; Mücke et al., 2003; Reimer et al., 2004; Razzaque et al., 2010).

However, while the lower radiative efficiency of protons allows the protons to radiate at higher frequencies, it also means that the proton-synchrotron model requires more energy in the magnetic field to match an observed flux. Because of the large Poynting flux required, we find that to match the typical observations of *Fermi*-LAT GRBs, either the energy requirements are prohibitive or the proton power-law distribution would have to begin at extremely high Lorentz factors.

As before, we are considering protons with a power-law distribution $dN_p(\gamma_p) \propto \gamma_p^{-p}\, d\gamma_p$ if $\gamma_p \geq \gamma_i$. The proton injection frequency, ν_i, is

$$\nu_i = \frac{qB\Gamma\gamma_i^2}{2\pi m_p c(1+z)} \approx 6.3\times 10^{-10} B\Gamma_2\gamma_i^2(1+z)^{-1}\ eV. \tag{5.53}$$

We define the cooling frequency, ν_c, as the frequency where the synchrotron cooling time of the protons that radiate at ν_c is equal to the dynamical time. The cooling time for protons is increased by a factor $\left(\frac{m_p}{m_e}\right)^3$ compared to the cooling time of electrons. The cooling frequency for proton synchrotron is

$$\nu_c \approx 5\times 10^{23} B^{-3} R_{15}^{-2}\Gamma_2^3(1+z)^{-1}\ \mathrm{eV}. \tag{5.54}$$

Since nearly all GRB observed in the *Fermi*-LAT band have a spectrum that can be fit by a single power law in the LAT band, we examine two possible spectral orderings: $\nu_i \sim \nu_c \leq \nu$ and the slow cooling regime $\nu_i \leq \nu \leq \nu_c$.

ν must be above ν_i to match the spectra of *Fermi*-LAT GRBs: $\nu \leq \nu_i$ cannot produce GRB LAT emission because if the protons are cooled (uncooled), the spectrum is $f_\nu \propto \nu^{-1/2}$ ($\nu^{1/3}$). These spectra are harder than what is observed for most GRB, which have a typical high energy f_ν index < -1 (Fermi Large Area Telescope Team et al., 2012). Therefore, we take $\nu_i \leq \nu$ to agree with a typical GRB spectrum. The synchrotron flux f_ν at the peak of the spectrum ($\nu_i = \min(\nu_i, \nu_c)$) is

$$f_\nu \approx 7BN_{52}\Gamma_2(1+z)d_{L,28}^{-2}\ \mu\text{Jy}, \tag{5.55}$$

where N is the total number of protons radiating in a dynamical time. The flux scales as $f_\nu \propto \nu^{-\frac{p-1}{2}}$ if $\nu_i \leq \nu \leq \nu_c$ and as $f_\nu \propto \nu^{-\frac{p}{2}}$ if $\nu \geq \nu_c, \nu_i$.

Below ν_p, the flux of a typical GRB is constant, $f_\nu \propto \nu^0$. Above ν_p, the flux scales as $f_\nu \propto \nu^{-1.2}$. Since this break is larger than one half, it cannot be attributed to a cooling break. Therefore, in order to have $f_\nu \propto \nu^0$ below ν_p, we require that both ν_i and ν_c lie above ν_p. Furthermore, the majority of LAT GRBs show a single power law above their peak, extending up to a maximum observed frequency, $\nu_{\max}$, on the order of tens of GeV. We need to ensure that the proton synchrotron radiation does not add any spectral features in this energy range. Since we have already ruled out the fast-cooling regime, there are only two possibilities: the cooled case where, $\nu_i \sim \nu_c \sim \nu_p \sim 1$ MeV with a $p \sim 2.4$ and the uncooled case where $\nu_i \sim \nu_p$, $\nu_c \gtrsim \nu_{\max}$ with $p \sim 3.4$. The cooled case can be ruled out because the energy required in the magnetic field is far too large. The uncooled case is considered in more detail in the following paragraphs.

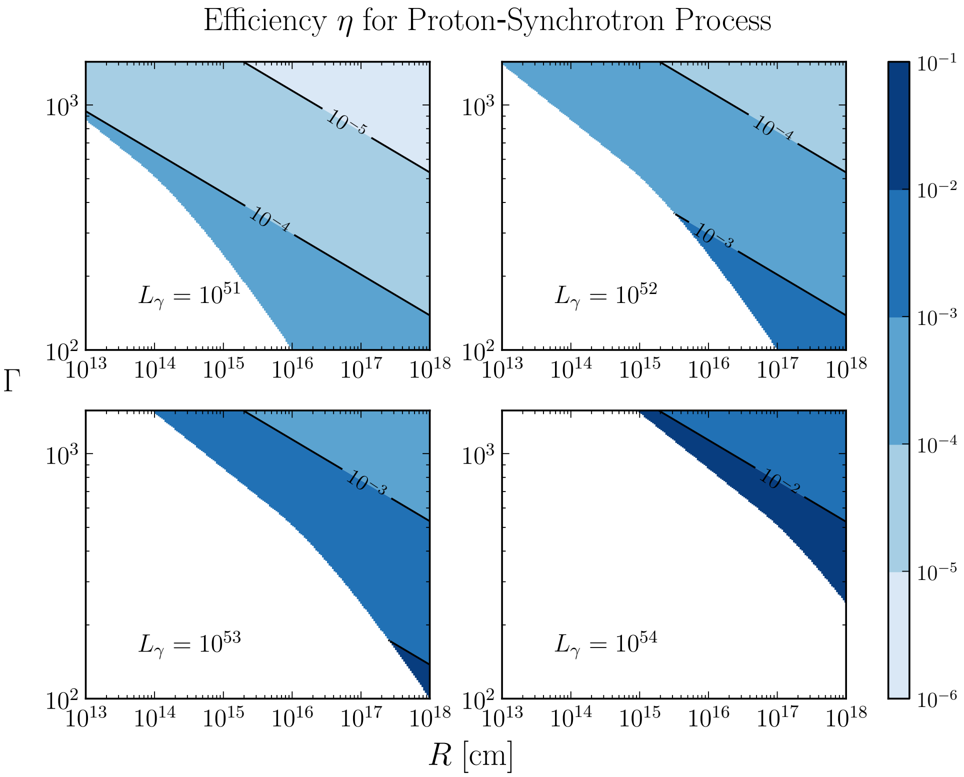

Figure 5.3: The maximum $\eta \equiv L_\gamma/(L_p + L_B)$ plotted in the $R - \Gamma$ plane for various values of L_γ to match a flux of $f_\nu = 1$ μJy at 100 MeV. As in the previous figures, we fix $z = 2$, and $d_L = 4.9 \times 10^{28}$ cm. This η corresponds to the necessary luminosity in magnetic field and protons with energies greater than $\sim 4\Gamma$ PeV to match a flux of $f_\nu = 1$ μJy at 100 MeV. The luminosity in protons with lower energies is likely comparable or much larger. Even when not considering the lower energy protons, the efficiency is very small for a vast majority of GRB parameter space. When η is not shown either the place of emission is below the photosphere or it is opaque to radiation of 10 GeV due to $\gamma + \gamma$ pair production.

If we require that $\nu_i \sim \nu_8$ (*i.e.* 100 MeV) and $\nu_c \gtrsim \nu_{\max} \sim 10$ GeV, we can then place an upper bound on the magnetic field by requiring that $\nu_c > \nu_{\max}$ and a lower bound by requiring that protons will be able to be accelerated to high enough energies to radiate at $\nu_{\max}$. As a practical matter, these bounds do not affect our maximally efficient proton-synchrotron radiation calculation for the parameter range considered. We then minimize the total luminosity required in both the magnetic field and protons radiating at an observed frequency ν_8 to match a typical observed flux of a few μJy.

The minimum Lorentz factor of the proton that radiates at ν_8 is

$$\gamma_i = 4 \times 10^8 B^{-1/2} \Gamma_2^{-1/2} (1+z)^{1/2} \nu_8^{1/2}. \tag{5.56}$$

This Lorentz factor gives a proton luminosity L_p of

$$L_p = 2\Gamma^3 \gamma_i R^{-1} m_p c^3 N \approx 5 \times 10^{58} f_{\nu,\mu\mathrm{Jy}} B^{-3/2} \Gamma_2^{3/2} R_{15}^{-1} \nu_8^{1/2} (1+z)^{-1/2} d_{L,28}^2 \text{ erg/s}. \tag{5.57}$$

Given the magnetic field luminosity, $L_B = 6 \times 10^{44} B^2 R_{15}^2 \Gamma_2^2$ erg/s, the total luminosity $L_B + L_p$ will be minimized with respect to B when $L_p = \frac{4}{3} L_B$, or when

$$B \approx 10^4 \; \Gamma_2^{-1/7} R_{15}^{-6/7} f_{\nu,\mu\mathrm{Jy}}^{2/7} \nu_8^{1/7} (1+z)^{-1/7} d_{L,28}^{4/7} \text{ Gauss}. \tag{5.58}$$

This magnetic field gives a proton luminosity

$$L_p = \frac{4}{3} L_B \approx 5 \times 10^{52} f_{\nu,\mu\mathrm{Jy}}^{4/7} \Gamma_2^{12/7} R_{15}^{2/7} \nu_8^{2/7} (1+z)^{-2/7} d_{L,28}^{8/7} \text{ erg/s}. \tag{5.59}$$

The efficiency η is plotted in figure 5.3. Note that L_B is not negligible as in figure 5.1 and 5.2, so in figure 5.3, $\eta \equiv L_\gamma/(L_p + L_B)$. The proton luminosity is much larger than the γ-ray luminosity for most of the allowed GRB parameter space. Additionally, proton synchrotron requires an unrealistically large γ_i.

Using eq (5.58),

$$\gamma_i \approx 4 \times 10^6 \ R_{15}^{3/7} \Gamma_2^{-3/7} (1+z)^{4/7} \nu_8^{3/7} f_{\nu,\mu\mathrm{Jy}}^{-1/7} d_{L,28}^{-2/7}. \qquad (5.60)$$

It is unclear what physical process could produce a power law with such a high minimum Lorentz factor. If every proton crossing the shock front is accelerated, the minimum Lorentz factor of a particle accelerated in relativistic shocks is approximately equal to the Lorentz factor of the shock front with respect to the unshocked fluid. The Lorentz factor can be proportionally larger if a small fraction of particles are accelerated and the remaining particles are "cold" downstream of the shock front. Considering that the Lorentz factor for GRB internal shocks is of order a few to perhaps a few tens, the typical proton Lorentz factor should be $\sim 10 - 10^3$ (the larger value corresponds to when only 1 in 10^2 protons are accelerated, as suggested by simulations, *e.g.* Sironi & Spitkovsky (2011b)). $\gamma_i \sim 4 \times 10^6$ is an unrealistically high injection Lorentz factor for relativistic shocks. If we set γ_i to 10^3, the proton synchrotron radiation would extend down to ~ 1 keV and would over produce in the GBM band. We can only decrease γ_i by a factor of 10 before over producing below the peak of the GRB spectrum. In summary, if proton synchrotron is to explain the observed LAT emission in GRBs, all of the protons must be accelerated to extremely high Lorentz factors very efficiently by some unknown mechanism.

The expected neutrino flux for the proton synchrotron model is estimated below. The total number of muon neutrinos is $\sim 2\tau_{p\gamma} N_p$, where $\tau_{p\gamma}$ is the optical depth to photo-pion production, given in eq (5.7), and N_p is calculated using eq (5.55) and (5.58):

$$N_\nu = 2 \times 10^{47} L_{\gamma,52} \Gamma_2^{-20/7} R_{15}^{-1/7} f_{\nu,\mu\mathrm{Jy}}^{5/7} \nu_{p,6}^{-1} (1+z)^{-13/7} \nu_8^{-1/7} d_{L,28}^{10/7}. \qquad (5.61)$$

Because the proton synchrotron radiation requires higher energy protons and larger magnetic fields compared to the photo-pion process, the pions produced will suffer larger radiative losses from synchrotron radiation before they decay. If the magnetic field is given by eq (5.58) we find that the pions will be cooled significantly by synchrotron radiation when $\Gamma_2^{12/7} R_{15}^{2/7} < 4 f_{\nu,\mu\mathrm{Jy}}^{3/7} \nu_8^{5/7} (1+z)^{2/7} d_{L,28}^{6/7}$. The neutrino flux will peak at an observed energy of $\sim \frac{1}{4}\Gamma \gamma_i m_\pi c^2/(1+z)$ if the pions are uncooled. If the pions are cooled, the flux will peak at the energy where pion cooling becomes important, or an energy of $\sim \frac{1}{4}\Gamma \gamma_{\pi,\mathrm{cool}} m_\pi c^2/(1+z)$ ($\gamma_{\pi,cool} \equiv 10^{14} B^{-2} \Gamma_2 R_{15}^{-1}$).

$$E_\nu = \begin{cases} 1.4 \times 10^7 \ \Gamma_2^{4/7} R_{15}^{3/7} f_{\nu,\mu\mathrm{Jy}}^{-1/7} \nu_8^{3/7} (1+z)^{-3/7} d_{L,28}^{-2/7} \ \mathrm{GeV}, \\ \text{ if pions are not cooled} \\ \\ 3.5 \times 10^6 \Gamma_2^{16/7} R_{15}^{5/7} f_{\nu,\mu\mathrm{Jy}}^{-4/7} \nu_8^{-2/7} (1+z)^{-5/7} d_{L,28}^{-8/7} \mathrm{GeV}, \\ \text{ if pions are cooled} \end{cases} \tag{5.62}$$

Since the protons are not cooled by the synchrotron loss mechanism, the observed neutrino flux is calculated using eq (5.16) and the dynamical time. The neutrino flux, F_ν, peaks at an energy given by eq (5.62) and is

$$F_\nu = \begin{cases} 1.4 \times 10^{-3} \ L_{\gamma,52} \Gamma_2^{-2/7} R_{15}^{-5/7} \nu_{p,6}^{-1} \nu_8^{2/7} f_{\nu,\mu\mathrm{Jy}}^{4/7} d_{L,28}^{-6/7} (1+z)^{-9/7} \ \mathrm{GeV\ cm^{-2} s^{-1}}, \\ \text{ if pions are not cooled} \\ \\ 3.3 \times 10^{-4} \ L_{\gamma,52} \Gamma_2^{10/7} R_{15}^{-3/7} \nu_{p,6}^{-1} \nu_8^{-3/7} f_{\nu,\mu\mathrm{Jy}}^{1/7} d_{L,28}^{-12/7} (1+z)^{-11/7} \ \mathrm{GeV\ cm^{-2} s^{-1}}, \\ \text{ if pions are cooled.} \end{cases} \tag{5.63}$$

As in Section 5.2.1.1, we estimate the neutrinos detected by IceCube per second of LAT emission from the proton synchrotron process:

$$\frac{dN_\nu}{dt} = \begin{cases} 10^{-3}\ L_{\gamma,52}\Gamma_2^{-4/7} R_{15}^{-13/14} f_{\nu,\mu\mathrm{Jy}}^{9/14} \nu_8^{1/14} \nu_{p,6}^{-1} d_{L,28}^{-5/7} (1+z)^{-15/14} \text{ counts s}^{-1}, \\ \text{ if the pions are not cooled} \\ \\ 5.6 \times 10^{-4}\ L_{\gamma,52}\Gamma_2^{2/7} R_{15}^{-11/14} f_{\nu,\mu\mathrm{Jy}}^{3/7} \nu_8^{-2/7} \nu_{p,6}^{-1} d_{L,28}^{-8/7} (1+z)^{-17/14} \text{ counts s}^{-1}, \\ \text{ if the pions are cooled.} \end{cases} \tag{5.64}$$

Therefore, for a bright GRB detected by the Fermi-LAT with $L_{\gamma,52} \sim 10$, $f_{\nu,\mu\mathrm{Jy}} \sim 2$, $\Gamma_2 \sim 9$, $z \sim 2$ and $\nu_{p,6} \sim 1$ and a duration of 10 seconds we find that the pions will be cooled if $R < 2 \times 10^{14}$ cm. We expect $\sim 4 \times 10^{-3} R_{15}^{-13/14}$ neutrinos of energy $2 \times 10^7 R_{15}^{3/7}$ GeV if $R > 2 \times 10^{14}$cm and $\sim 6 \times 10^{-3} R_{15}^{-11/14}$ neutrinos of energy $2.7 \times 10^7 R_{15}^{5/7}$ GeV if $R < 2 \times 10^{14}$cm.

5.5 Summary and Discussion

With a goal of understanding typical observed 100 MeV fluxes in bright *Fermi*-LAT GRBs during the prompt emission, we estimated the generation of photons by high-energy protons traveling through a shell of photons whose energy distribution is given by the Band function. We calculated the minimum energy in protons required to reproduce *Fermi*-LAT observations for the following hadronic processes: photo-pion, Bethe-Heitler pair production, and proton synchrotron.

Unlike previous works, we specifically focused on the energy required for hadronic models to produce the >100 MeV photons seen in *Fermi* GRBs and how this requirement depends on GRB parameters. To provide additional physical insight into the energy requirements, we have provided both analytical estimates and more detailed numerical calculations.

We find that photo-pion Δ-resonance is much more efficient than Bethe-

Heitler pair production at producing high-energy electrons—so much so that Bethe-Heitler pair production can be ruled out as a mechanism for producing $\gtrsim$100 MeV photons observed by *Fermi*-LAT. The photo-pion process is capable of producing high energy electrons, but to match the *Fermi*-LAT flux at 100 MeV, the photo-pion process requires an energy in protons that is $\gtrsim 10^4$ times greater than isotropic energy in the γ-ray photons. Since the Bethe-Heitler photo-pairs are produced more efficiently at low energies, Bethe-Heitler production will be the dominant process at low energies. These low-energy Bethe-Heitler electrons will have the same spectral index as the high-energy photo-pion electrons (assuming there isn't a cooling break). Therefore it is possible that both processes could add up to produce a single power-law deviation from the Band function that extends from low to high energies. This type of spectral feature has been observed in several *Fermi* GRBs.

According to our calculations, proton synchrotron is capable of producing the *Fermi*-LAT GRB emission more efficiently than the other hadronic processes. The proton synchrotron could possible achieve efficiencies on the order of 1-10% for the brightest GRBs, if we assume that the minimum Lorentz factor for proton accelerated in shocks is extremely large $\sim 2 \times 10^6$. The minimum proton Lorentz factor of order 10^6 is much larger than what is expected based on our current understanding of relativistic collisionless shocks. Regardless of the mechanism accelerating the protons, these high energy protons with LF greater than 10^6 likely carry only a small fraction of the total energy carried by the protons.

We also calculated the expected neutrino flux if the LAT emission is from the photo-pion process or proton synchrotron radiation. In the photo-pion process, for a bright LAT GRB with a Lorentz Factor of 900 and a duration of 10 seconds, we expect $\sim .1$ neutrinos detected by IceCube at an energy of $\sim 10^6$ GeV. This predicted neutrino detection rate is much larger than single burst neutrino count estimates by Guetta et al. (2004); Razzaque et al. (2003). The actual count number reported in each of the papers is 0.010.1, but they consider a hypothetical neutrino detector with a effective area of 1km^2, much larger than the IceCube 59-string effective area at 10^5 GeV.Therefore, it may be possible to rule out photo-pion emission when the emission from multiple bursts is considered. For proton synchrotron radiation, the neutrino flux also depends on the emission radius, R. For a bright LAT GRB with a Lorentz factor of 900, an emission radius of 10^{15} cm and duration of 10 seconds, we expect a $\sim 4 \times 10^{-3}$ neutrinos detected by IceCube at an energy $\sim 2 \times 10^7$ GeV.

In summary, all the hadronic processes considered in this paper require significantly more energy in protons than the observed energy in gamma-rays to reproduce the high-energy flux observed in *Fermi*-LAT GRBs.

Bibliography

Abbasi R. et al., 2012, Nature, 484, 351

Abdo A. A. et al., 2009a, ApJ, 706, L138

Abdo A. A. et al., 2009b, Science, 323, 1688

Achterberg A., Gallant Y. A., Kirk J. G., Guthmann A. W., 2001, MNRAS, 328, 393

Ackermann M. et al., 2011, ApJ, 729, 114

Aharonian F. A., 2000, New Astronomy, 5, 377

Aliu E. et al., 2011, ApJ, 738, L30

Anninos P., Fragile P. C., Wilson J., Murray S. D., 2012, ApJ, 759, 132

Asano K., Mészáros P., 2012, ApJ, 757, 115

Asano K., Guiriec S., Mészáros P., 2009, ApJ, 705, L191

Asano K., Inoue S., Mészáros P., 2010, ApJ, 725, L121

Atwood W. B. et al., 2009, ApJ, 697, 1071

Badnell N. R., Bautista M. A., Butler K., Delahaye F., Mendoza C., Palmeri P., Zeippen C. J., Seaton M. J., 2005, MNRAS, 360, 458

Balbus S. A., Hawley J. F., 1991, ApJ, 376, 214

Ballone A. et al., 2013, ApJ, 776, 13

Band D. et al., 1993, ApJ, 413, 281

Baranov V. B., Krasnobaev K. V., Kulikovskii A. G., 1971, Soviet Physics Doklady, 15, 791

Barniol Duran R., Piran T., 2013, MNRAS, 770, 146

Begelman M. C., 2012, MNRAS, 420, 2912

Begelman M. C., Blandford R. D., Rees M. J., 1984, Reviews of Modern Physics, 56, 255

Bell A. R., 1978, MNRAS, 182, 147

Beloborodov A. M., 2010, MNRAS, 407, 1033

Beniamini P., Piran T., 2014, MNRAS, 445, 3892

Berger E., Zauderer A., Pooley G. G., Soderberg A. M., Sari R., Brunthaler A., Bietenholz M. F., 2012, ApJ, 748, 36

Bessho N., Bhattacharjee A., 2012, ApJ, 750, 129

Bethe H. A., Maximon L. C., 1954, Physical Review, 93, 768

Birn J. et al., 2001, JGR, 106, 3715

Biskamp D., 1986, Physics of Fluids, 29, 1520

Blandford R., Eichler D., 1987, Physics Reports, 154, 1

Blandford R. D., Ostriker J. P., 1978, ApJ, 221, L29

Blandford R. D., Payne D. G., 1982, MNRAS, 199, 883

Blandford R. D., Znajek R. L., 1977, MNRAS, 179, 433

Bloom J. S. et al., 2011, Science, 333, 203

Blumenthal G. R., 1971, Phys. Rev. D., 3, 2308

Blumenthal G. R., Gould R. J., 1970, Reviews of Modern Physics, 42, 237

Bondi H., 1952, MNRAS, 112, 195

Bondi H., Hoyle F., 1944, MNRAS, 104, 273

Böttcher M., Dermer C. D., 1998, ApJ, 499, L131

Bower G. C., Metzger B. D., Cenko S. B., Silverman J. M., Bloom J. S., 2013, ApJ, 763, 84

Bower G. C. et al., 2015, ApJ, 802, 69

Burkert A., Schartmann M., Alig C., Gillessen S., Genzel R., Fritz T. K., Eisenhauer F., 2012, ApJ, 750, 58

Burrows D. N. et al., 2011, Nature, 476, 421

Celotti A., Padovani P., Ghisellini G., 1997, MNRAS, 286, 415

Cenko S. B. et al., 2012, ApJ, 753, 77

Cerutti B., Uzdensky D. A., Begelman M. C., 2012, ApJ, 746, 148

Chhotray A., Lazzati D., 2015, ApJ, 802, 132

Coroniti F. V., 1990, ApJ, 349, 538

Corsi A., Guetta D., Piro L., 2010, ApJ, 720, 1008

Crumley P., Kumar P., 2013a, MNRAS, 429, 3238

Crumley P., Kumar P., 2013b, MNRAS, 436, 1955

Dai Z. G., Lu T., 2002, ApJ, 580, 1013

Davies R. D., Walsh D., Booth R. S., 1976, MNRAS, 177, 319

De Colle F., Raga A. C., Contreras-Torres F. F., Toledo-Roy J. C., 2014, ApJ, 789, L33

de Gouveia dal Pino E. M., Lazarian A., 2005, A&A, 441, 845

de Jager O. C., Harding A. K., Michelson P. F., Nel H. I., Nolan P. L., Sreekumar P., Thompson D. J., 1996, ApJ, 457, 253

de Kool M., Begelman M. C., 1989, Nature, 338, 484

Degenaar N., Wijnands R., Miller J. M., Reynolds M. T., Kennea J., Gehrels N., 2015, ArXiv e-prints

Deng W., Zhang B., 2014, ApJ, 785, 112

Dermer C. D., Chiang J., Böttcher M., 1999, ApJ, 513, 656

Dotan C., Shaviv N. J., 2011, MNRAS, 413, 1623

Drake J. F., Swisdak M., Che H., Shay M. A., 2006, Nat, 443, 553

Drenkhahn G., 2002, A&A, 387, 714

Drenkhahn G., Spruit H. C., 2002, A&A, 391, 1141

Dungey J., 1953, Phil. Mag., 44, 725

Dyson J. E., 1975, Ap&SS, 35, 299

Eatough R. P. et al., 2013, Nat, 501, 391

Falcke H., Goss W. M., Matsuo H., Teuben P., Zhao J. H., Zylka R., 1998, ApJ, 499, 731

Fan Y., Piran T., 2006, MNRAS, 369, 197

Fermi Large Area Telescope Team et al., 2012, ApJ, 754, 121

Gao W. H., Mao J., Xu D., Fan Y. Z., 2009, ApJ, 706, L33

Gezari S. et al., 2012, Nat, 485, 217

Ghisellini G., ed., 2013, Radiative Processes in High Energy Astrophysics, Lecture Notes in Physics, Berlin Springer Verlag, Vol. 873

Ghisellini G., Celotti A., 1999a, ApJ, 511, L93

Ghisellini G., Celotti A., 1999b, A&A, 138, 527

Ghisellini G., Guilbert P. W., Svensson R., 1988, ApJ, 334, L5

Ghisellini G., Celotti A., Lazzati D., 2000, MNRAS, 313, L1

Ghisellini G., Tavecchio F., Maraschi L., Celotti A., Sbarrato T., 2014, Nat, 515, 376

Giannios D., 2008, A&A, 480, 305

Giannios D., Metzger B. D., 2011, MNRAS, 416, 2102

Giannios D., Sironi L., 2013, MNRAS, 433, L25

Giannios D., Spruit H. C., 2006, A&A, 450, 887

Gillessen S., Eisenhauer F., Trippe S., Alexander T., Genzel R., Martins F., Ott T., 2009, ApJ, 692, 1075

Gillessen S. et al., 2012, Nature, 481, 51

Gillessen S. et al., 2013a, ApJ, 763, 78

Gillessen S. et al., 2013b, ApJ, 774, 44

Ginzburg V. L., Syrovatskii S. I., 1965, ARA&A, 3, 297

Greiner J. et al., 2009, A&A, 498, 89

Guetta D., Hooper D., Alvarez-Mun˜Iz J., Halzen F., Reuveni E., 2004, Astroparticle Physics, 20, 429

Guillochon J., Catalogue of Possible Tidal Disruption Events, http://astrocrash.net/resources/tde-catalogue/, accessed April 2015

Guo F., Li H., Daughton W., Liu Y. H., 2014, PRL, 113, 155005

Haggard D. et al., 2014, The Astronomer's Telegram, 6242, 1

Hargrave P. J., Ryle M., 1974, MNRAS, 166, 305

Hascoët R., Daigne F., Mochkovitch R., Vennin V., 2012, MNRAS, 421, 525

Herrnstein R. M., Zhao J. H., Bower G. C., Goss W. M., 2004, AJ, 127, 3399

Hillas A. M., 1984, ARA&A, 22, 425

Hora J. L. et al., 2014, ApJ, 793, 120

Jaroschek C. H., Treumann R. A., Lesch H., Scholer M., 2004, Physics of Plasmas (1994-present), 11, 1151

Jennison R. C., Das Gupta M. K., 1953, Nat, 172, 996

Jiang Y. F., Stone J. M., Davis S. W., 2014, ApJ, 796, 106

Jones F. C., 1965, Phys. Rev., 137, B1306

Jones F. C., 1968, Phys. Rev., 167, 1159

Kasen D., Ramirez-Ruiz E., 2010, ApJ, 714, 155

Kelley L. Z., Tchekhovskoy A., Narayan R., 2014, MNRAS, 445, 3919

Kennel C. F., Coroniti F. V., 1984, ApJ, 283, 710

Komissarov S. S., 2001, MNRAS, 326, L41

Komissarov S. S., Barkov M. V., Vlahakis N., Königl A., 2007, MNRAS, 380, 51

Komissarov S. S., Vlahakis N., Königl A., Barkov M. V., 2009, MNRAS, 394, 1182

Kulsrud R. M., 1998, Physics of Plasmas, 5, 1599

Kulsrud R. M., 2005, Plasma physics for astrophysics

Kumar P., 1999, ApJ, 523, L113

Kumar P., Barniol Duran R., 2009, MNRAS, 400, L75

Kumar P., Barniol Duran R., 2010, MNRAS, 409, 226

Kumar P., Crumley P., 2015, in prep

Kumar P., McMahon E., 2008, MNRAS, 384, 33

Kumar P., Zhang B., 2015, Physics Reports, 561, 1 , The physics of gamma-ray bursts & relativistic jets

Kumar P., Hernández R. A., Bošnjak Ž., Barniol Duran R., 2012, MNRAS, 427, L40

Kumar P., Barniol Duran R., Bošnjak Ž., Piran T., 2013, MNRAS, 434, 3078

Lacy J. H., Townes C. H., Hollenbach D. J., 1982, ApJ, 262, 120

Larrabee D. A., Lovelace R. V. E., Romanova M. M., 2003, ApJ, 586, 72

Lazzati D., Begelman M. C., 2010, ApJ, 725, 1137

Levan A. J. et al., 2011, Science, 333, 199

Lithwick Y., Sari R., 2001a, ApJ, 555, 540

Lithwick Y., Sari R., 2001b, ApJ, 555, 540

Liu D., Pe'er A., Loeb A., 2015, ApJ, 798, 13

Lovelace R. V. E., Li H., Koldoba A. V., Ustyugova G. V., Romanova M. M., 2002, ApJ, 572, 445

Lundman C., Pe'er A., Ryde F., 2013, MNRAS, 428, 2430

Lyubarsky Y., Kirk J. G., 2001, ApJ, 547, 437

Lyutikov M., 2006, New Journal of Physics, 8, 119

Lyutikov M., Blandford R., 2003, ArXiv Astrophysics e-prints

Margon B., 1984, ARA&A, 22, 507

Maselli A. et al., 2014, Science, 343, 48

Maxham A., Zhang B. B., Zhang B., 2011, MNRAS, 415, 77

McCourt M., Madigan A. M., 2015, ArXiv e-prints

McKinney J. C., 2006, MNRAS, 368, 1561

McKinney J. C., Tchekhovskoy A., Blandford R. D., 2012, MNRAS, 423, 3083

McKinney J. C., Tchekhovskoy A., Blandford R. D., 2013, Science, 339, 49

Mészáros P., Rees M. J., 1993, ApJ, 405, 278

Mészáros P., Rees M. J., 1997, ApJ, 482, L29

Mészáros P., Rees M. J., 2000, ApJ, 530, 292

Metzger B. D., Giannios D., Thompson T. A., Bucciantini N., Quataert E., 2011, MNRAS, 413, 2031

Metzger B. D., Giannios D., Mimica P., 2012, MNRAS, 420, 3528

Michel F. C., 1969, ApJ, 158, 727

Michel F. C., 1982, Reviews of Modern Physics, 54, 1

Mimica P., Giannios D., Metzger B. D., Aloy M. A., 2015, ArXiv e-prints

Mücke A., Protheroe R. J., Engel R., Rachen J. P., Stanev T., 2003, Astroparticle Physics, 18, 593

Murase K., Asano K., Terasawa T., Mészáros P., 2012, ApJ, 746, 164

Nakar E., Ando S., Sari R., 2009, ApJ, 703, 675

Narayan R., Igumenshchev I. V., Abramowicz M. A., 2003, PASJ, 55, L69

Narayan R., Özel F., Sironi L., 2012a, ApJ, 757, L20

Narayan R., SÄdowski A., Penna R. F., Kulkarni A. K., 2012b, MNRAS, 426, 3241

Ohsuga K., Mineshige S., 2011, ApJ, 736, 2

Panaitescu A., Kumar P., 2002, ApJ, 571, 779

Park J. H., Trippe S., Krichbaum T. P., Kim J. Y., Kino M., Bertarini A., Bremer M., de Vicente P., 2015, ArXiv e-prints

Parker E. N., 1957, JGR, 62, 509

Pe'er A., 2008, ApJ, 682, 463

Petschek H. E., 1964, in W.N. Hess, ed., The Physics of Solar Flares. Proceedings of the AAS-NASA Symposium, Vol. 50, p. 425

Pfuhl O. et al., 2015, ApJ, 798, 111

Phifer K. et al., 2013, ApJ, 773, L13

Phinney E. S., 1989, in M. Morris, ed., The Center of the Galaxy. IAU Symposium, Vol. 136, p. 543

Piran T., 2004, Reviews of Modern Physics, 76, 1143

Piran T., Sadowski A., Tchekhovskoy A., 2015, ArXiv e-prints

Poutanen J., Lipunova G., Fabrika S., Butkevich A. G., Abolmasov P., 2007, MNRAS, 377, 1187

Pozdnyakov L. A., Sobol I. M., Syunyaev R. A., 1983, Astrophysics and Space Physics Reviews, 2, 189

Rachen J., 1996, Ph.D. thesis, University of Bonn

Rachen J. P., Mészáros P., 1998, Phys. Rev. D., 58, 123005

Rawlings S., Saunders R., 1991, Nat, 349, 138

Razzaque S., Mészáros P., Waxman E., 2003, Phys Rev D, 68, 083001

Razzaque S., Mészáros P., Zhang B., 2004, ApJ, 613, 1072

Razzaque S., Dermer C. D., Finke J. D., 2010, The Open Astronomy Journal, 3, 150

Rees M. J., 1988, Nat, 333, 523

Rees M. J., Meszaros P., 1994, ApJ, 430, L93

Rees M. J., Mészáros P., 2005, ApJ, 628, 847

Reimer A., Protheroe R. J., Donea A. C., 2004, New Astronomy Reviews, 48, 411

Remillard R. A., McClintock J. E., 2006, ARA&A, 44, 49

Romanova M. M., Lovelace R. V. E., 1992, A&A, 262, 26

Rybicki G. B., Lightman A. P., 1986, Radiative Processes in Astrophysics

Samtaney R., Loureiro N. F., Uzdensky D. A., Schekochihin A. A., Cowley S. C., 2009, PRL, 103, 105004

Santana R., Hernández R. A., Crumley P., Kumar P., 2015, MNRAS, submitted.

Sari R., Esin A. A., 2001, ApJ, 548, 787

Sari R., Piran T., Narayan R., 1998, ApJ, 497, L17

Saxton C. J., Soria R., Wu K., Kuin N. P. M., 2012, MNRAS, 422, 1625

Sądowski A., Narayan R., Sironi L., Özel F., 2013a, MNRAS, 433, 2165

Sądowski A., Sironi L., Abarca D., Guo X., Özel F., Narayan R., 2013b, MNRAS, 432, 478

Schartmann M., Burkert A., Alig C., Gillessen S., Genzel R., Eisenhauer F., Fritz T. K., 2012, ApJ, 755, 155

Schlafly E. F., Finkbeiner D. P., 2011, ApJ, 737, 103

Scoville N., Burkert A., 2013, ApJ, 768, 108

Sell P. H. et al., 2010, ApJ, 719, L194

Semenov V., Dyadechkin S., Punsly B., 2004, Science, 305, 978

Shakura N. I., Sunyaev R. A., 1973, A& A, 24, 337

Shen R. F., Barniol Duran R., Nakar E., Piran T., 2015, MNRAS, 447, L60

Sironi L., Spitkovsky A., 2011a, ApJ, 741, 39

Sironi L., Spitkovsky A., 2011b, ApJ, 726, 75

Sironi L., Spitkovsky A., 2014, ApJ, 783, L21

Spitkovsky A., 2008, ApJ, 682, L5

Stern B. E., Poutanen J., 2004, MNRAS, 352, L35

Strubbe L. E., Quataert E., 2009, MNRAS, 400, 2070

Sweet P. A., 1958, in B. Lehnert, ed., Electromagnetic Phenomena in Cosmical Physics. IAU Symposium, Vol. 6, p. 123

Syrovatskii S. I., 1981, ARA&A, 19, 163

Tchekhovskoy A., McKinney J. C., Narayan R., 2008, MNRAS, 388, 551

Tchekhovskoy A., Narayan R., McKinney J. C., 2010, ApJ, 711, 50

Tchekhovskoy A., Narayan R., McKinney J. C., 2011, MNRAS, 418, L79

Tchekhovskoy A., Metzger B. D., Giannios D., Kelley L. Z., 2014, MNRAS, 437, 2744

Thompson C., 1994, MNRAS, 270, 480

Thompson C., Gill R., 2014, ApJ, 791, 46

Thompson C., Mészáros P., Rees M. J., 2007, ApJ, 666, 1012

Totani T., 1998, ApJ, 509, L81

Tout C. A., Pringle J. E., 1996, MNRAS, 281, 219

Tsuboi M. et al., 2015, ApJ, 798, L6

Usov V. V., 1992, Nature, 357, 472

Uzdensky D. A., Kulsrud R. M., 2000, Physics of Plasmas, 7, 4018

van Velzen S., Frail D. A., Körding E., Falcke H., 2013, A&A, 552, A5

Vlahakis N., Königl A., 2004, ApJ, 605, 656

Vurm I., Lyubarsky Y., Piran T., 2013, ApJ, 764, 143

Wang F. Y., Cheng K. S., 2012, MNRAS, 421, 908

Wang Q. D. et al., 2013, Science, 341, 981

Wang X. Y., He H. N., Li Z., Wu X. F., Dai Z. G., 2010, ApJ, 712, 1232

Werner G. R., Uzdensky D. A., Cerutti B., Nalewajko K., Begelman M. C., 2014, ArXiv e-prints

Wilkin F. P., 1996, ApJ, 459, L31

Witzel G. et al., 2014, ApJ, 796, L8

Yamada M., Ji H., Hsu S., Carter T., Kulsrud R., Ono Y., Perkins F., 1997, PRL, 78, 3117

Yuan F., Quataert E., Narayan R., 2003, ApJ, 598, 301

Zamaninasab M., Clausen-Brown E., Savolainen T., Tchekhovskoy A., 2014, Nat, 510, 126

Zauderer B. A. et al., 2011, Nature, 476, 425

Zauderer B. A., Berger E., Margutti R., Pooley G. G., Sari R., Soderberg A. M., Brunthaler A., Bietenholz M. F., 2013, ApJ, 767, 152

Zenitani S., Hoshino M., 2001, ApJ, 562, L63

Zhang B., Mészáros P., 2001, ApJ, 559, 110

Zhang B. et al., 2007, ApJ, 655, 989

Zhang B. B. et al., 2011, ApJ, 730, 141

Zhao J. H., Young K. H., Herrnstein R. M., Ho P. T. P., Tsutsumi T., Lo K. Y., Goss W. M., Bower G. C., 2003, ApJ, 586, L29

Zou Y. C., Fan Y. Z., Piran T., 2011, ApJ, 726, L2

Zweibel E. G., Yamada M., 2009, ARA&A, 47, 291

Vita

Patrick Crumley grew up in Iowa, son of Dr. David Crumley and Rene Crumley. Patrick graduated with honors from Grinnell College in 2008 with a B.A. in Physics and a concentration in East Asian Studies. During this time, Patrick spent one semester abroad at Waseda University in Toyko. Patrick began his studies as a graduate student in the Physics department at University of Texas at Austin in Fall 2008. Patrick married Diana Crumley in May 2009. They welcomed into the world their first child, Arlo James, in February 2015.

Permanent address: 4113 Avenue C, Austin, TX 78751

This dissertation was typeset with LaTeX[†] by the author.

[†] LaTeX is a document preparation system developed by Leslie Lamport as a special version of Donald Knuth's TeX Program.